Laser Cooling and Trapping of Neutral Calcium Atoms

Ian Norris

A thesis presented in partial fulfillment
of the requirements for the degree of
Doctor of Philosophy

Department of Physics
University of Strathclyde

August 2009

This thesis is the result of the author's original research. It has been composed by the author and has not been previously submitted for examination which has lead to the award of a degree.

Signed: Date:

Laser Cooling and Trapping of Neutral Calcium Atoms

Ian Norris

Abstract

This thesis presents details on the design and construction of a compact magneto-optical trap (MOT) for neutral calcium atoms. All of the apparatus required to successfully cool and trap $\sim 10^6$ ^{40}Ca atoms to a temperature of $\sim$3 mK are described in detail.

A new technique has been developed for obtaining dispersive saturated absorption signal using a hollow-cathode lamp. The technique is sensitive enough to detect signals produced by isotopes of calcium with abundances of less than 0.2 %.

A compact Zeeman slower has been used to reduce the velocity of a thermal beam of calcium atoms to around 60 m/s, which are then deflected into a MOT using resonant light. A discussion on the characterisation and optimisation of the Zeeman slower and deflection stage is also given.

The number of atoms trapped in the MOT has been shown to increase by a factor of $\sim$4 when a repumping laser at 672 nm is used to excite atoms from the $^1D_1$ state back into the main cooling cycle. As this transition is excited the lifetime of the MOT increases, with lifetimes up to 50 ms having been measured. These measurements are compared with a rate equation model and were found to be in agreement. A 1530 nm diode laser has also been used in conjunction with the 672 nm laser, to repump atoms from the metastable $^3P_2$ state back into the cooling cycle, increasing the trapped atom number by a further 70 %.

Acknowledgements

The process of doing an experimental physics PhD has been one of the most rewarding experiences of my life. Learning the physics has been great, but working with fantastic people has made it even better.

I consider myself extremely lucky to have had Professor Erling Riis as my PhD supervisor, he is a true master of experimental physics. His crystal clear explanations of physical principles has allowed me to grasp difficult concepts with relative ease. Not only was his guidance critical to the success of this study, but his company has made it a very enjoyable experience. Erling, thank you for teaching me all that you have done, feeding back on this thesis and for putting up with me!

A huge thank you goes to Dr Aidan Arnold for his encouragement and advice over the past three years. Aidan's input throughout the whole PhD has been invaluable to my development and I consider myself lucky to have had him also supervise my studies. Cheers Aidan!

Thanks to the other academics of the Photonics group; Thorsten Ackemann, Nigel Langford and the group founder Professor Allister Ferguson for help and encouragement over the years.

Dr. Umakanth Dammalapati joined the calcium experiment in April 2007 and brought with him a wealth of experience from his previous experiment, which involved laser cooling of barium. I have thoroughly enjoyed working with Umakanth and learned large amount from his practical expertise.

Thanks to Luke Maguire and Mateusz Borkowski who also made major contributions to the calcium experiment and were excellent company during their time in Glasgow.

Much of the apparatus used in the experiment was made from original components created by the Photonics workshop. Many thanks to Bob, Ewan, Paul and Lisa for all of their help and hard work, and for some really good laughs.

The other students and post-docs who co-inhabited the Photonics group office made a great environment for working in. The three years would not have been the same without Wei, Fiona, Matt, Kenneth, Stef, Neal, Yann, Nick, Kanu, Simon and Alessio.

With their practical jokes and good-fun nature Mateusz Zawadzki and Kyle Gardner made the office a fun and very exciting place to work and I'm lucky to have started my PhD at the same time as these two good friends. I am very grateful to Paul 'Griff' Griffin for his constant encouragement and for being a good friend. I'm disappointed that our time in the group did not overlap more.

Craig 'The Craigy-Boy' Hamilton, we've had some awesome nights out, especially in the early days at TFI! Cheers for being a good buddy throughout this process.

Someone else on the PhD road, doing work in a biology orientated version of the Photonics group, is my wee brother Greg. Not only is his friendship one of the most valued things in my life, but his advice is always the best. Thanks to Greg for all of his support and encouragement over the duration of the PhD, as well as the past 23 years. You're some man for reading this as well!

My Granny & Granda and Nana & Papa have always been major influences on shaping me as a person. All of the love and support that they have given me over the past four years, as well as all the previous years, has kept me focused and on track. Thank you so much for everything.

Now for my Mum and Dad. I'm probably a bit old to still be at home, but I've not just been living with my parents, I've been staying with my greatest friends. Their guidance is *always* the best and their support is *always* rock-solid, for this

I am truly grateful. You guys mean everything to me and I want to say thanks for being there every single time. This book is for you guys.

On the 31^{st} of March 2001 I became the luckiest guy in the world. That was the night I met ma Wee Yin. Everyday I still can't believe just how lucky I am to have such a beautiful, caring and thoughtful person to share my life with. I'm sorry that this has taken so long and that things have been delayed for longer than they should have been, but I'll never forget your patience and encouragement over this last year. The best thing in the world is knowing that when I see you and hear your voice everything else melts away and all I feel is warm, cosy and happy. You are everything to me and from now on nothing is going to stop our wee team. Mandy, I love you and I'll never stop. Love Bugs.

Contents

List of Figures

Abbreviations

AOM	Acousto-optic Modulator
AR	Anti-Refection
BEC	Bose-Einstein Condensate
BS	Beamsplitter
Ca	Calcium
CCD	Charged Coupled Device
ECDL	External Cavity Diode Laser
FWHM	Full-Width at Half-Maximum
HR	High Refelction
IR	Infrared
MOT	Magneto-Optical Trap
PBS	Polarising Beam Splitter
PD	Photodiode
PM	Polarisation Maintaining
PTFE	Polytetrafluoroethylene
PZT	Piezoelectric Transducer
Rb	Rubidium
RF	Radio Frequency
ROC	Radius Of Curvature
TEC	Peltier Thermoelectric Cooler

Physical Constants [1]

Atomic mass unit	1 amu=1.661×10^{-27} kg
Bohr Magneton	$\mu_B = 9.74 \times 10^{-24}$ J/T
Boltzmann's Constant	$k_B = 1.381 \times 10^{-23}$ J/K
Electron Charge	$e = 1.602 \times 10^{-19}$ C
Electron Mass	$m_e = 9.109 \times 10^{-31}$ kg
Permeability of free space	$\mu_0 = 4\pi \times 10^{-7}$ H/m
Permittivity of free space	$\epsilon_0 = 8.854 \times 10^{-12}$ F/m
Plank's Constant	$h = 6.626 \times 10^{-34}$ Js
Reduced Plank's Constant	$\hbar = 1.055 \times 10^{-34}$ Js
Speed of light in vacuum	$c = 2.998 \times 10^{8}\mathrm{ms}^{-1}$

Chapter 1

Introduction

1.1 Laser cooling

1.1.1 History and development

In 1975, Hänsch and Schawlow published an article that described how an ensemble of neutral atoms could be brought to a temperature close to absolute zero, using laser light [2]. In that seminal article they stated that coherent light, slightly red detuned from the relevant atomic transition, could be used to remove an atom's kinetic energy, to the point where the Doppler width was as small as the natural linewidth. In fact, it was later discovered that the lower energy limit of their laser cooling technique results in a Doppler width well below the natural linewidth [3]. At around the same time, Wineland and Dehmelt independently suggested that laser light could be used to remove energy from trapped ions [4], and indeed, the process of Doppler cooling (or laser cooling) was first demonstrated on ions trapped in electric fields [5]. Despite laser cooling reducing the kinetic energy of each ion, Coulomb interactions limit the number of particles that can be cooled simultaneously within a given volume [6].

If an atom is moving towards a laser beam that is red detuned from its resonance frequency, the Doppler effect causes the atom to experience the light shifted closer to resonance and is more likely to absorb a photon from the beam. On the other hand, if the atom and laser light are propagating in the same direction, the light is shifted further from resonance and no photon will be absorbed. Since photons that are absorbed are re-emitted randomly into space, this results in a net force in the direction opposite to the atom's motion.

It took a number of years to develop the light sources and build an experimental setup that was capable of cooling atoms in the way that Hänsch and Schawlow envisaged. Phillips and Metcalf demonstrated in 1986 how the technique could be used to slow a thermal beam of neutral sodium atoms [7]. However, it was Steven Chu, and co-workers at Bell Labs, that were the first to experimentally realise resonance radiation pressure cooling in three dimensions [8]. They used three orthogonal, counter-propagating, laser beam pairs to cool a cloud of sodium atoms to 240 μK in a configuration known as optical molasses.

At around the same time, Phillips and Metcalf had demonstrated that it was possible to trap neutral atoms using a quadrapole magnetic field [9]. As the force that atoms experience in optical molasses is independent of position, a technique was sought that would trap the cold atoms and also allow long interaction times; the ideal situation for spectroscopic measurements. The magneto-optical trap (MOT) was the fruit of this work, developed in 1987, it was designed to incorporate optical molasses and magnetic trapping into a single setup, see Fig. 1.1 [10]. The method proved to be successful and produced 10 million atoms, cooled to a temperature of ~ 600 μK, for over two minutes.

The theory of laser cooling had been well developed by the time the first MOT had been created [11], therefore, the community was surprised when the group at NIST produced results which showed that atoms cooled in optical molasses could exhibit a temperature below the Doppler limit [12]. It was not long before it was realised that Doppler theory was too simple to apply to multi-level atoms and so the theory for laser cooling was extended to include the additional mechanisms which could enable further cooling [13, 14, 15]. For their contributions to the experimental realisation and theoretical description of laser cooling, Steven Chu,

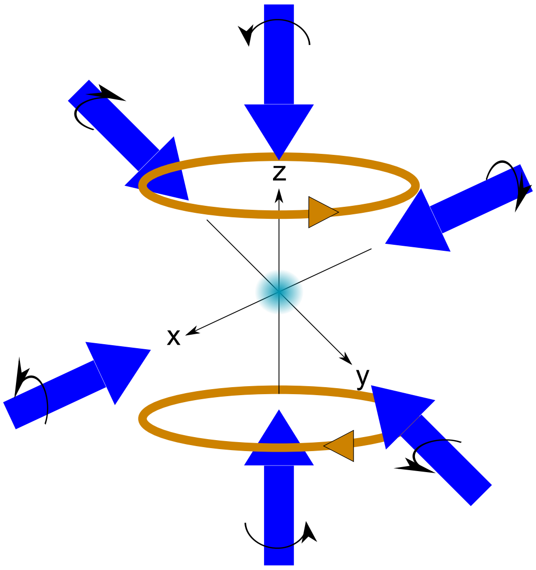

Figure 1.1: The configuration of the anti-Helmholtz coils and laser beams used in a MOT. The arrows indicate the direction current flows through the coils and the handedness of the circularly polarised light beams.

William Phillips and Claude Cohen-Tannoudji were each awarded one third of the 1997 Nobel prize in physics [16, 17, 18].

Laser cooling is a method for creating a sample of atoms that have a high phase space density (PSD)= $n\lambda_{\mathrm{dB}}^3$, where n is the number density and λ_{dB} is the thermal de Broglie wavelength. A high PSD describes a group of atoms that have narrow spatial and velocity distributions; a property that is useful in many areas of physics. If the atoms involved have integer spin, i.e. they are bosons, and have a PSD above 2.62, they enter the quantum degenerate regime [19]. Therefore, there exists a critical temperature, T_c, at which the thermal de Broglie wavelength of each atom becomes larger than the inter-particle spacing and the atoms collapse into the lowest energy, quantum mechanical state of the system. This phenomenon is known as Bose-Einstein condensation (BEC) and was first predicted in 1924 [20, 21].

Well-known phenomena such as superconductivity [22] and superfluidity [23] have been long known to exhibit some of the behaviour expected from a quantum degenerate system, however, these systems can only be described by strong inter-particle interactions, since the atoms are closely packed. The strong interactions make the resulting macroscopic state difficult to understand and is not the original vision of a BEC, which was based on weakly interacting particles. The advent of laser cooling provided a fast and efficient route to achieving high phase space densities for weakly interacting particles. However, the re-absorption and emission of photons limits a MOT from reaching the temperatures and densities required to enter the quantum degenerate regime [24].

Higher phase space densities were achieved when laser cooled atoms were transfered into magnetic traps. In this case re-absorption of light was no longer a limiting issue [25], and a technique known as evaporative cooling was used to further cool the atoms [26]. This technique involves removing the hottest atoms from a trap and allowing the remaining atoms to re-thermalise at a colder temperature; this is analogous to blowing on a spoonful of hot soup before putting it in your mouth. In 1995, within the space of three months, the groups at JILA and MIT both reported that they had used an evaporative cooling technique to Bose condense gases of rubidium and sodium respectively [27, 28]. For their work in experimentally realising the first Bose-Einstein condensates Carl Wieman, Eric Cornell and Wolfgang Ketterle won the Nobel prize in Physics in 2001 [29, 30].

Much like the laser at the time it was invented, Bose Einstein condensates have found few practical applications in everyday life. However, they have been frequently employed in experimental setups to test fundamental physics problems. BECs have been used by over 70 groups [31] to study fundamental topics in physics such as wave-particle duality [32] and the superfluid to Mott insulator phase transition [33]. Closely related experiments have cooled fermions (particles with half-integer spin) to a temperature at which a degenerate Fermi gas forms [34]. In this case, the atoms are forbidden to all collapse into the trap's ground state by the Pauli exclusion principle and so each atom then has to occupy the lowest available energy level. Although direct laser cooling methods of molecules have been proposed [35], Bose condensation of molecules was actually achieved using cold fermions and forcing them to form bosonic molecules [36]. This area of research has allowed direct study of the BCS-BEC crossover regime [37].

1.1.2 Atomic species

With the exception of metastable helium [38], ytterbium [39] and most recently chromium [40], the elements which have been Bose condensed have been limited to atoms with a single outer electron; hydrogen [41], lithium [42], sodium [28], potassium [43], rubidium [27] and caesium [44]. It is only relatively recently that laser sources have become readily available that are capable of driving the electronic transitions of more exotic species.

The atoms of the alkali-earth group of elements have drawn the interest of the laser cooling community in recent years for a number of reasons. The even isotopes of this group have no nuclear spin and as a result have a non-degenerate singlet ground state. This produces an almost ideal two-level energy level structure, simplifying the theory associated with the interaction of light. However, the addition of the spins of the outer electrons also results in a triplet energy level scheme, connected to the singlet scheme through narrow resonances known as intercombination lines.

Much of the previous work, which has made use of laser cooled alkali-earth atoms, has focused on utilising the narrow resonances between the singlet and triplet schemes for frequency metrology [45, 46]. The second is currently defined via the RF frequency of the radiation corresponding to the transition between the two hyperfine levels of the ground state of of ^{133}Cs [47]. Narrow linewidth optical radiation could be used as a faster frequency reference and allow improved accuracy over the current standard. However, techniques that are capable of measuring optical frequencies have only recently become available [48]. The $^1S_0-^3P_1$ transition in calcium has been demonstrated to be a possible reference for a future frequency standard by the PTB group in Germany and the JILA group in the US [49, 50].

In addition to being used as a frequency reference, laser cooled alkali-earths have been used to model how atoms collide at very low temperatures [51, 52]. The non-degenerate ground state of the alkali-earths reduces complexity of the theory for cold collisions greatly when compared to the alkalis. Experiments have since been performed which have resulted in the photoassociation of calcium, allowing the theory to be directly compared with experiment [53]. Laser cooled alkali-earths may also provide a method of measuring the electronic dipole moment [54].

The ${}^1S_0 - {}^3P_1$ transition in ^{40}Ca is narrow enough to facilitate laser cooling to extremely low temperatures. However, direct laser cooling of this transition is not possible as the resulting spontaneous force is not large enough to support against gravity. In strontium, where the intercombination line is wider and gravity is not an issue, samples have been created which have a phase space density 1000 times greater than have been achieved by laser cooling the alkalis [55].

Stimulating the main intercombination line in ^{40}Ca, where $\Gamma < 400$ Hz, presents the huge engineering challenge of generating light with a linewidth narrower than that of the transition [56]. The JILA group have demonstrated that such a source is not critical to drive this transition using a technique known as 'quenched narrow line cooling' [57]. Here they have artificially decreased the lifetime of the metastable state by exciting the atoms into higher lying states that can decay quickly to the ground state. The linewidth of the long-lived state can then effectively be controlled by the number of atoms excited to the higher lying state, but at the expense of heating; due to higher energy photons. Another way to continually stimulate this transition would be to trap the atoms in a dipole trap and continually irradiate the transition [58].

The group at PTB has shown very recently that forced evaporative cooling can be used to reach these temperatures and allow a calcium BEC to form. They have used a laser close to the 'magic wavelength' to generate a dipole trap the atoms. In this situation, the laser induces ac-Stark shifts that are equal for the ground state and the $^3P_1$ state, allowing direct cooling using a 657 nm laser. Using the trapping laser in a crossed dipole trap configuration they have trapped around 20,000 atoms and cooled them to a temperature of around 200 nK and observed the bimodal distribution synonymous with the formation of a BEC [59]. At almost the same time, the Innsbruck group used an evaporative cooling technique to Bose condense Strontium [60].

The aim of the work presented in this thesis was to develop a source of laser cooled calcium atoms, which could be used as a platform for exploring paths to reach the low temperatures required for a calcium BEC. The majority of the the work herein details the design and construction of the components used to create this source of cold calcium [61, 62]. The system has been characterised in detail and has been used to demonstrate new repumping schemes for collecting cold samples of atoms.

1.2 Thesis layout

- Chapter 2 summaries the fundamental theory required for the laser cooling of neutral atoms. The latter part of the of the chapter gives relevant information the properties of calcium and reviews the energy level structure of ^{40}Ca.

- For light to interact with ensembles of free neutral atoms it is essential that there are as few collisions with background atoms as possible. Chapter 3 describes the design and construction of the vacuum system used for the experiments in this thesis.

- Chapter 4 details the frequency doubled laser system used to create the blue light for driving the strong laser cooling transition. A simple frequency stabilisation technique, for atoms that do not have commercially available vapour cells, is also described.

- A number of diode lasers were employed in the experiment, used for frequency references and for probing atomic transitions. These lasers, and the methods used to stabilise them, are described in Chapter 5.
- Measurements obtained from characterising and optimising the laser cooling system are given in Chapter 6.
- Chapter 7 describes how a homemade ECDL and commercial telecoms laser were used to control the lifetime of the MOT and the states that the trapped atoms were permitted to occupy.
- Chapter 8 concludes with a thesis summary and a discussion of possible future experiments.

Chapter 2

Laser cooling and the alkali earths

2.1 Laser cooling

2.1.1 The scattering force

For an ensemble of two-level atoms interacting with a laser beam of intensity I, red-detuned from the atomic resonance, ω_0, the fraction of the atoms in the excited state is given by [63]

$$n_{\mathrm{e}} = \frac{1}{2}\frac{(I/I_{\mathrm{sat}})}{1 + (I/I_{\mathrm{sat}}) + (2\delta/\Gamma)^2}, \tag{2.1}$$

where ω is the angular frequency of the laser, ω_0 is the atomic resonance frequency, $\delta = \omega - \omega_0$ and Γ is the decay rate of the transition. The saturation intensity, I_{sat}, is defined, such that, if a laser beam is resonant with an atomic transition and has an intensity of I_{sat}, the atom will spend one quarter of its time in the excited state. Knowing the atomic transition wavelength, λ, and its spontaneous emission coefficient, A_{ik}, the saturation intensity is calculated via [24]

$$I_{\mathrm{sat}} = \frac{\pi h c A_{\mathrm{ik}}}{3\lambda^3}, \tag{2.2}$$

where h is Planck's constant and c is the speed of light.

Consider a two level atom, with a resonant frequency ω_0, that is interacting with a laser beam propagating along the z direction, with a wavelength $\lambda = 2\pi c/\omega$. The atom initially has a velocity v_z and so experiences the laser light Doppler shifted to $\omega' = \omega - kv_z$. If the atom is moving towards the laser source it finds the light blue-shifted closer to the atomic resonance and so will scatter more photons. If it is moving away from the laser, the frequency of the light is red shifted further from resonance and the atom will interact less strongly with the light.

The photons that make up the laser beam each carry an absolute momentum of $p = \hbar k$, where $\hbar$ is the reduced Planck constant and $k = 2\pi/\lambda$. When the atom absorbs a photon from the beam it gains a momentum p, in the direction the photon was traveling. When the atom spontaneously re-emits the photon it receives a momentum kick, of the same magnitude, resulting in an associated recoil velocity $v_\mathrm{r} = \hbar k/m$ in a random direction. Since each of the laser's photons produce a momentum change in the same direction, and the emission process is symmetric, many absorption/emission events result in an average force on the atom in the direction of the laser beam, slowing the atom down. This force is known as the scattering force. It is the basis of laser cooling and its magnitude is calculated by multiplying the photon momentum by the rate at which the atom can scatter photons [64]. Dividing this force by the atomic mass gives the acceleration the atom experiences as it moves towards a red detuned laser beam,

$$a = \frac{\Gamma\hbar k}{2m}\frac{I/I_\mathrm{sat}}{1 + (I/I_\mathrm{sat}) + (2(\delta - kv_z)/\Gamma)^2}. \tag{2.3}$$

The acceleration saturates as $I \to \infty$, due to the populations of the upper and lower states both approaching 1/2. This results in a maximum acceleration,

$$a_\mathrm{max} = \frac{\hbar k}{m}\frac{\Gamma}{2} = v_\mathrm{r}(\Gamma/2). \tag{2.4}$$

In the case of the ${}^1\mathrm{S}_0$–${}^1\mathrm{P}_1$ transition for a ^{40}Ca atom, a resonant beam can cause a maximum possible acceleration of 2.6×10^6 m/s^2, which is almost three hundred thousand times the acceleration due to gravity! The acceleration the atom experiences clearly depends on the rate of the absorption/emission cycle, which scales with the amount of time that the atom spends in the excited state, i.e. the shorter the excited state lifetime, the stronger the cooling transition. For calcium this excited state lifetime is of the $^1S_0-^1P_1$ transition is 4.6 ns, resulting in a very strong line for laser cooling.

Table 2.1 compares the transitions of some elements that have been successfully used for laser cooling and highlights the differences between important atomic parameters for the alkali and the alkali-earth metals in the same row of the periodic table.

	^{39}K	^{87}Rb	^{40}Ca	^{88}Sr
Mass [amu]	39	87	40	88
Abundance [%]	93.3	28	97	83
Main cooling line	$4^2S_{1/2}$-$4^2P_{3/2}$	$5^2S_{1/2}$-$5^2P_{3/2}$	4^1S_0-4^1P_1	4^1S_0-4^1P_1
A_{ik} [s^{-1}]	3.87×10^7	3.81×10^7	2.18×10^8	2.02×10^8
λ [nm]	766.701	780.241	422.792	460.862
$a_{\max}$ [m/s^2]	2.58×10^5	1.1×10^5	2.56×10^6	9.9×10^5
$\Gamma/2\pi$ [MHz]	6.2	5.9	34.2	31.8
I_{sat} [mW/cm^2]	1.81	1.67	60	42.7
T_{D} [μk]	148	145	832	767
v_{rec} [mm/s]	13.3	6.02	23.5	9.84
T_{rec} [μk]	0.83	0.37	2.67	1.02

Table 2.1: A comparison of relevant atomic parameters for the main cooling transitions for the isotopes of elements used in laser cooling experiments [65].

The theory described above can be extended to the more useful situation where a laser is used to reduce the velocity of the atoms in a thermal atomic beam, which can be achieved by illuminating the collimated beam with laser light propagating opposite to the atomic motion. As the beam is made up of atoms with a distribution of velocities, the laser detuning is chosen to be on resonance with a particular velocity class. However, a major problem arises quickly in this scenario: as atoms are slowed down by the laser, the Doppler shift corresponding to their new velocity effectively tunes the laser out of resonance and the atoms absorb photons at a much lower rate. Taking the example of cooling on the main calcium transition, which has a natural linewidth of 34 MHz, an atomic change in velocity of 1 m/s results in a Doppler shift of 2.4 MHz, giving a maximum velocity change of 15 m/s before the atoms no longer interact with the laser light.

Originally, this problem was first solved by altering the laser frequency as the atoms slowed, such that the laser was constantly resonant with the atoms. This 'frequency chirping' technique can be achieved using either an EOM [66] or by directly modulating the laser itself [67]. However, experiments that make use of this method of slowing have the serious disadvantage of producing a pulsed atomic beam.

In 1982, an atomic beam was passed down the axis of a tapered solenoid. Current flowing in the solenoid created a spatially varying magnetic field and provided a Zeeman shift to compensate for the changing Doppler shift [7]. This varying magnetic field and laser beam combination are commonly referred to as a Zeeman slower.

2.1.2 The position dependent scattering force

Zeeman effect

Applying an external magnetic field, $B(z)$, to an atom where the nuclear spin is absent shifts the atomic energy levels by an amount $\Delta E = \mu_{\mathrm{B}} g_J m_J B(z)$, where μ_{B} is the Bohr magneton, m_J is the magnetic quantum number, g_J is the Landé g-factor for the fine structure level J and is given by [68]

$$g_J = \frac{3}{2} + \frac{S(S+1) - L(L+1)}{2J(J+1)}. \tag{2.5}$$

For a two level atom with ground and excited levels $J = 0$ and $J = 1$ respectively, the Zeeman effect splits the energy of the excited level into three magnetic sublevels, $m_J = -1, 0, +1$. These sub-levels must each be driven by a laser beam with σ^-, π, σ^+ polarisations respectively, which are defined relative to the z-direction for the 1-D case.

The Zeeman slower

By still considering the case of a laser propagating opposite to an atomic beam, when an inhomogeneous magnetic field is introduced along the interaction region this results in an additional detuning of the laser beam from the atomic resonance,

$$\Delta_{\pm}(z) = \delta \pm kv + \frac{\mu_{\mathrm{B}}}{\hbar} g_J m_J B(z), \tag{2.6}$$

Substituting $\Delta_{\pm}(z)$ for $\delta \pm kv$ into Eqn. 2.3 results in an acceleration that is both velocity and position dependent,

$$a = \frac{\Gamma \hbar k}{2m} \frac{I/I_{\mathrm{sat}}}{1 + (I/I_{\mathrm{sat}}) + (2\Delta_{\pm}(z)/\Gamma)^2}. \tag{2.7}$$

For a constant deceleration, the velocity of an atom moving along the length of a Zeeman slower is $v(t) = v_0 - at$, and the distance traveled can be found from $z(t) = v_0 t - at^2/2$, where v_0 is the atom's initial velocity. The time and distance to slow an atom to $v(t)$, is given by,

$$t = \frac{v_0}{a} \quad \text{and} \quad s = \frac{v_0^2}{2a}. \tag{2.8}$$

At every position along the atomic path, the magnetic field must have a value such that it cancels the Doppler shift so the laser beam is continuously on resonance with the transition, i.e. $\Delta_{\pm}(z) = 0$. By rearranging the equations of motion above, the required magnetic field can be found as a function of the position, z, along the path of the slower. To slow the atom, which has $g_J = 1$, when using the $m_J = +1$ level, the field required to keep the atom on resonance is given by,

$$B(z) = B_{\mathrm{bias}} \pm B_0 \sqrt{1 + \frac{2az}{v_0^2}}, \tag{2.9}$$

where $B_{\mathrm{bias}} = \hbar\delta/\mu_{\mathrm{B}}$, $B_0 = hv_0/\mu_{\mathrm{B}}\lambda$, and $a \approx a_{max}/3$ [7]. The B_{bias} depends on the laser detuning, if it is neglected when B_0 is calculated δ can then be used as a free parameter to select an initial velocity class to slow.

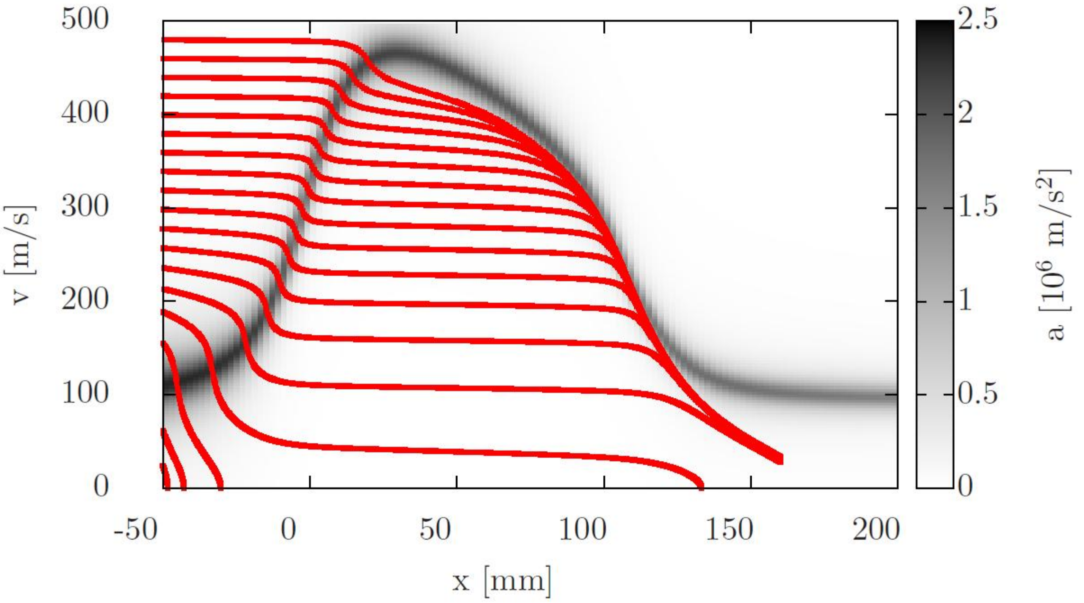

Figure 2.1: The magnitude of the spatially and velocity dependent acceleration is given by the grey-scale on the right-hand side. Each red line corresponds to the motion of atoms along the length of the slower for a number of initial velocity classes as they enter the Zeeman slower.

A plot of the acceleration experienced by an atom moving through the calcium experiment Zeeman slower is plotted in Fig. 2.1. Values for the equation parameters were taken from the actual experimental values, which are described in detail in Chapter 3. The red lines along the length of the plot show the trajectories for atoms in a number of different velocity classes. It can be seen that atoms with initial velocities between 200 and 500 m/s are decelerated to around 60 m/s, at which point they exit the slower.

Traditionally Zeeman slowers generate the required magnetic field by passing a current through a solenoid, set up such that the $m_J = +1$ level can be driven using σ^+ polarised light for slowing. More recent techniques have been developed which slightly improve on the original design. For example using a σ^- polarised beam is used for slowing this has the advantage that atoms can be quickly taken out of resonance with the beam. In other cases the solenoid has been replaced with a permanent magnet, which can help in cases where power and cooling issues are critical [69, 70].

Any atoms with different initial velocities below the v_0 are shifted into resonance with the laser beam at different points along the slower. This bunches atoms that were initially in different velocity classes together in a slower velocity distribution. This is not strictly cooling of the atoms, rather, just a reduction of the mean velocity in one direction.

2.1.3 Doppler cooling

Consider a single atom in a 1-D standing wave created by two identical, counter-propagating, laser beams, which are slightly red-detuned from the atomic resonance. If the atom is moving it experiences the light it is moving towards Doppler shifted closer to resonance and the light it is moving away from Doppler shifted further from resonance. The atom will therefore scatter more photons from the beam it moves towards and experiences a force opposite to its velocity, slowing the atom down. The total force on the atom in this 1-D case is given by [24]

$$\begin{aligned} F = \hbar k(\Gamma/2)&\frac{I/I_{\text{sat}}}{1+(2I/I_{\text{sat}})+4(\delta+kv)^2/\Gamma^2} \\ -\hbar k(\Gamma/2)&\frac{I/I_{\text{sat}}}{1+(2I/I_{\text{sat}})+4(\delta-kv)^2/\Gamma^2}. \end{aligned} \tag{2.10}$$

For (red) detunings, $\delta = \omega - \omega_0 < 0$, and atomic velocities close to zero, this force varies linearly with velocity, $F = -\alpha v$, as shown in Fig. 2.2. Producing a damping force on the atom similar to a particle moving in a viscous fluid. Consequently, this mechanism is commonly known as ‘optical molasses’ [8]. The damping coefficient, α, is given as [71]

$$\alpha = 4\hbar k^2 \frac{I}{I_{\text{sat}}} \frac{2\delta/\Gamma}{(1+2\delta/\Gamma)^2}. \tag{2.11}$$

The critical velocity, $v_c \approx \delta/k$, depicted by vertical lines in Fig. 2.2, marks the velocities over which Eqn. 2.11 is valid; outside this region the force is no longer directly proportional to the velocity and the atoms are less efficiently cooled.

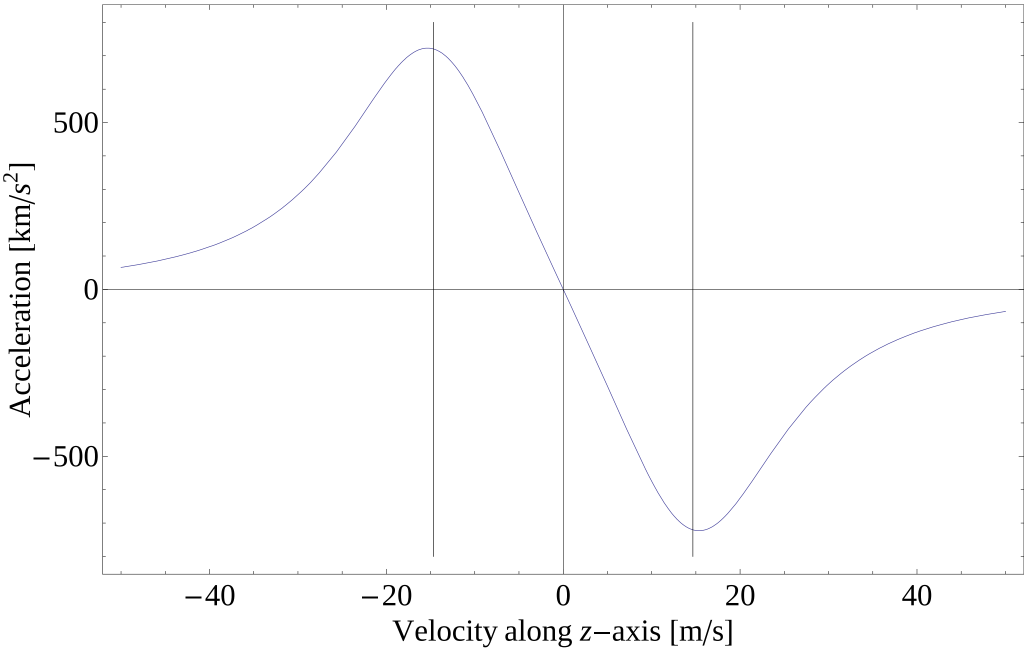

Figure 2.2: The linear force around $v_{\mathrm{z}} = 0$, for one-dimensional Doppler cooling on the strong ${}^1\mathrm{S}_0$–${}^1\mathrm{P}_1$ transition of ^{40}Ca, where $\delta = -\Gamma$ and the incident intensity is equal to the saturation intensity. The vertical lines mark the linear region over which the force can be described by a damping constant.

The damping force described above can be used to remove kinetic energy from a system of atoms and hence reduce their velocity. However, there is a limit to the cooling process. The recoil velocity associated with the emission or absorption of a photon gives rise to heating which competes with the damping force, resulting in each atom having a steady state, nonzero velocity. The movement of the atoms in momentum space is due to the random direction in which the photon is spontaneously re-emitted and also the uncertainty in the number of photons absorbed from the light field. An equilibrium temperature is reached when the heating rate equals the cooling rate of the damping force, which is described by [68]

$$T = \frac{\hbar\Gamma}{4k_B}\frac{1 + I/I_{sat} + (2\Delta/\Gamma)^2}{2|\Delta|/\Gamma}, \tag{2.12}$$

where k_{B} is Boltzmann's constant. The Doppler temperature, T_{D}, is the minimum of this function and occurs at low laser intensities and a detuning of $\delta = -\Gamma/2$,

$$T_{\mathrm{D}} = \frac{\hbar\Gamma}{2k_{\mathrm{B}}}. \tag{2.13}$$

Atoms cooled in this manner are constantly absorbing and emitting photons, making the atoms undergo a random walk in momentum space in a way similar to Brownian motion. As there is no restoring force to keep atoms fixed in space they can eventually diffuse out of the molasses region and are therefore eventually lost from the cooling process.

Sub-Doppler cooling techniques have been developed that allow temperatures to be reached that are well below the Doppler Temperature [13, 71, 14, 15]. However, as there is no hyperfine splitting of the strong ${}^1\mathrm{S}_0$–${}^1\mathrm{P}_1$ transition in ^{40}Ca, standard sub-Doppler cooling techniques cannot be used.

2.1.4 Position dependent Doppler cooling

Ideally, long interaction times are required to make precise spectroscopic measurements of the electronic transitions in atoms. The MOT uses an optical molasses setup combined with a spherical quadrupole magnetic field $B(z)$, to trap atoms for long time periods [10]. The field is typically created using two co-axial coils in an anti-Helmholtz configuration, positioned so the zero of the field coincides with the intersection point of the molasses beams.

For relatively small detunings, replacing Eqn. 2.6 for $\delta - kv$ in Eqn. 2.10 gives a force proportional to the atomic velocity as well as position [72]. The principle of operation for a MOT in one-dimension, for a $J = 0$ to $J = 1$ transition is given in Fig. 2.3. As in the case for molasses, the laser beams are red-detuned from resonance and as the magnetic field is linear with z, the $\sigma^{\pm}$ beams propagating in the $\pm z$ directions drive the $\Delta m_J = \pm 1$ transitions respectively. As can be seen from the figure, atoms on the positive (negative) side of the origin have the $m_J = -1$ $(+1)$ sub-level lowered in energy and scatter more σ^- (σ^+) than σ^+ (σ^-) photons. As the atoms are cooled they are also pushed toward the zero of the magnetic field, confining them in space.

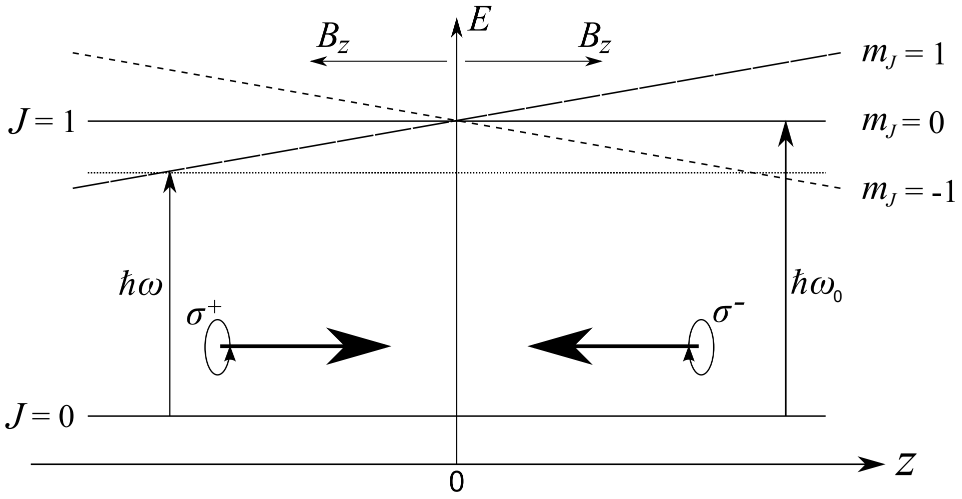

Figure 2.3: The principle of operation of the MOT. The Zeeman splitting of the m_J sub-levels depends on the position of the atom along the z-axis. The two counter-propagating $\sigma^{\pm}$ beams drive the $m_J = \pm 1$ respectively, creating an imbalance in the scattering force that pushes the atom towards the zero of the magnetic field ($B(0) = 0$).

This one dimensional treatment is readily extended to three dimensions [73]. However, it should be noted that the three dimensional field created by the anti-Helmholtz coils disturbs the light shift created by the standing wave of the orthogonal beams, breaking down the mechanism for sub-Doppler cooling. As a result, it should be noted that sub-Doppler cooling can only be observed in optical molasses.

Capture velocity

For the one dimensional case, the capture velocity of the calcium MOT was found by numerically calculating an atom's position and velocity as it moves through the z-axis MOT beam. All of the MOT beams are derived from a single source and therefore all have a Gaussian profile of width σ. By assuming that the fastest atom that can be trapped by the MOT comes to rest 1.5 σ beyond the trap centre, and that the atoms's acceleration can be described by Eqn. 2.3, the atom's motion is calculated as shown in Fig. 2.4. Calculating the capture velocity for atoms incoming from the z direction returns the maximum possible velocity as the magnetic field gradient is largest in this direction.

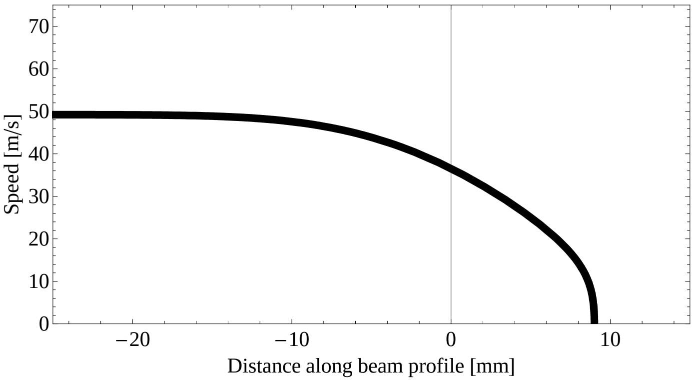

Figure 2.4: A numerical simulation of an atom's velocity along the z-axis as it enters and moves through the MOT. The simulation calculates the initial velocity of an atom that has been slowed to 0 m/s at the point it passes 1.5 σ beyond the trap centre. This is calculated for a detuning Δ = -24 MHz, a MOT with 10 mW of power in each beam and a field gradient of 18 G/cm.

To find how the capture velocity varied with MOT trapping parameters, the numerical simulation was adapted and run for different initial conditions. Fig. 2.5 shows how the capture velocity varies with the diameter of the MOT beams. As is expected, the capture velocity increases with increasing MOT beam diameter, d, due to the longer time that the atom will spend in the beam. However, as the power that was available for the MOT beams was limited, $d = 12$ mm was chosen so as to drive the atoms close to saturation when trapped in the MOT.

Fig. 2.6 shows the variation in the capture velocity as the detuning of the MOT beams is changed. As the laser frequency is detuned further from resonance the MOT can capture atoms with faster velocities. As the laser cooling process produces the coldest temperatures for a beam detuning of $\Gamma/2$, using a detuning far from this value would introduce heating of the atoms. Experimentally a value of $\Delta = -24$ MHz was found to give the highest trapped atom number, this is

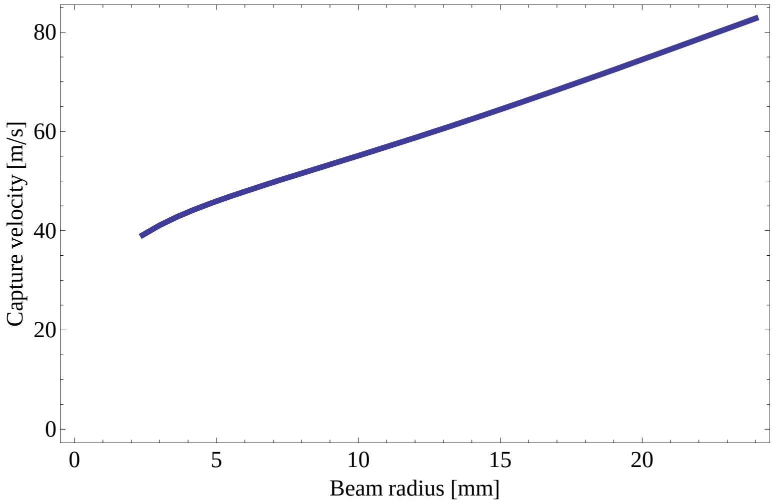

Figure 2.5: The variation of the capture velocity with beam radius, for a constant detuning of $\Delta = -24$ MHz and a constant field gradient of 18 G/cm.

close to the optimum detuning, and also gives a capture velocity close to the velocity of the incoming atoms.

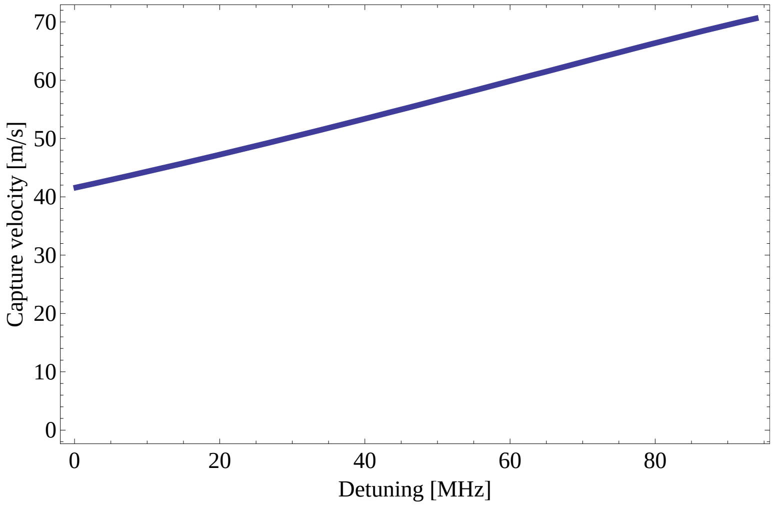

Figure 2.6: The variation of the capture velocity with laser detuning for a constant field gradient of 18 G/cm and a constant beam diameter of 1.2 cm with 10 mW in each beam.

Fig. 2.7 shows the variation of the capture velocity as the MOT field gradient is changed. These plots also show that field gradient does not have a large influence on the capture velocity. Therefore, optical molasses removes the energy from the atoms, the field only acts to trap the atoms once they have been slowed.

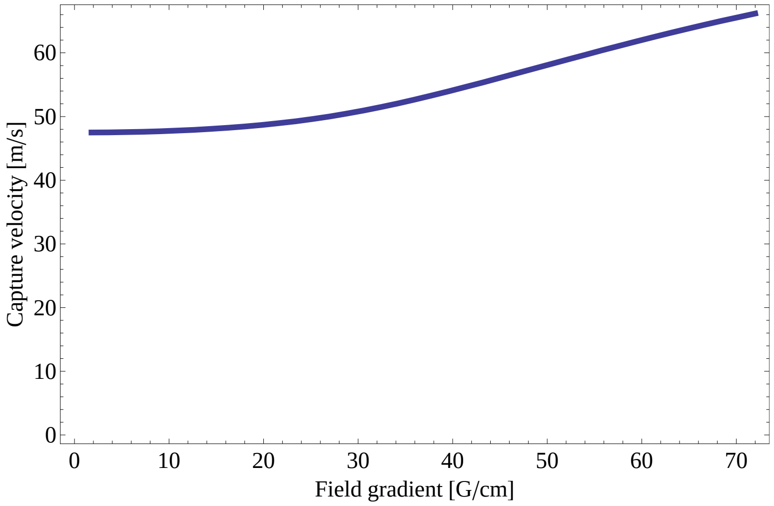

Figure 2.7: The variation of the capture velocity with the magnetic field gradient for a MOT beam diameter of 1.2 cm, a beam detuning of $\Delta = -24$ MHz and 10 mW in each beam.

2.2 Calcium

For a hydrogen atom, the allowed electronic transitions are governed by the presence of only one proton in the nucleus and the one orbiting electron. At the time laser cooling was demonstrated, there was a lack of efficient ultraviolet laser sources, which meant that many of the techniques developed for laser cooling were for more complex atomic species.

The alkali metals are similar in structure to hydrogen as they have only one valence electron. However, they have additional sub-shells of orbiting electrons, as well as a number of extra protons and neutrons within the nucleus that change their energy level structure away from being purely hydrogen-like [74].

The laser sources required to stimulate the cooling transitions of the alkali metals have been readily available for many years. Narrow linewidth, near IR, diode lasers were developed in the early 90's and have been the source of coherent light for many atomic physics experiments [75, 76]. The presence of a nuclear spin in the alkali metals results in hyperfine splitting of the ground state, producing in a loss channel for atoms laser cooled on the D2 line. An additional laser is required to 'repump' atoms decaying to the lower hyperfine state back into the cooling cycle. When the repump laser is used in conjunction with the trap laser, atoms can be trapped in a MOT for time limited by collisions with background atoms in the vacuum chamber.

As more efficient, narrow-linewidth, laser sources are created [77], there is an option of laser cooling more exotic species, such as the alkali earth metals. Changing the atomic source in a laser cooling experiment from rubidium to an alkali earth atom, like calcium, removes the problem of a hyperfine ground state but introduces other leaks into the system. An aim of the work for this thesis was to find a suitable repumping scheme for ^{40}Ca and remove the decay channels to allow a large number of atoms to be trapped at low temperatures.

2.2.1 Physical properties of calcium

Calcium is a reactive, soft metal with atomic properties that place it in the s-block of the periodic table. It has a melting point of 840 °C and boils at 1480 °C [74]. Solid calcium has a metallic silver colour, but rapidly forms an oxide coating when exposed to air, which clouds its metallic surface [78].

Vapour pressure

At 840 °C the melting point of calcium is very high when compared to the potassium, which is in the same row of the periodic table, but only has a melting point of 63 °C. The *vapour pressure* is the pressure of a vapour in equilibrium with its solid and liquid phases and is a measure of how many atoms are released from a solid as it is heated. The vapour pressure can be modeled with the equation

$$\log_{10}P = 5.006 + a + \frac{b}{T} + (c * \log_{10}T), \tag{2.14}$$

where P is the vapour pressure in mPa, $a = 10.127$, $b = -9517$ and $c = -1.4030$ are constants found in the literature [74], and T is the temperature of the metal in kelvin. It can be seen from Fig. 2.8 that calcium must be heated to a temperature four times higher than that of potassium to reach a sufficient vapour pressure of 10 mPa.

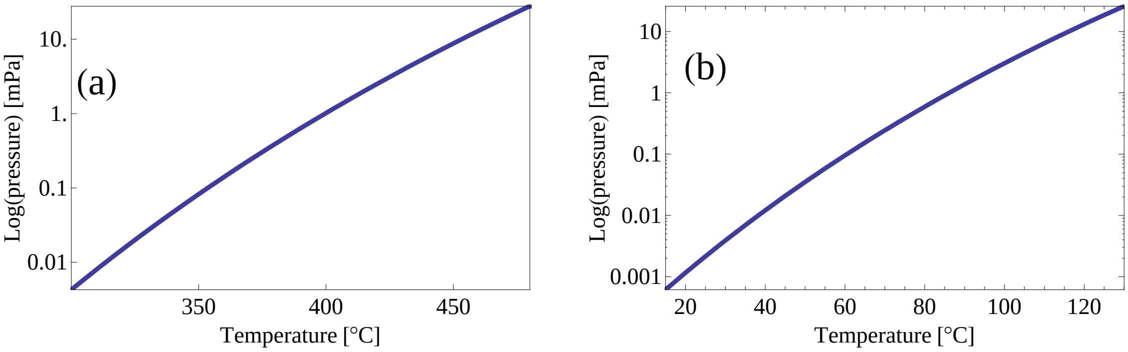

Figure 2.8: The vapour pressure calculated using Eqn. 2.14, where $a = 10.127$, $b = -9517$ and $c = -1.4030$ for (a) calcium and (b) potassium.

2.2.2 Atomic and spectroscopic properties

Neutral calcium atoms have 20 protons and electrons, however, there are a number of calcium isotopes that have properties summarised in Table 2.2 [79]. The most abundant isotope is ^{40}Ca, accounting for 97% of all the calcium on Earth, and unless otherwise stated the rest of this thesis only considers this isotope.

As an alkali earth metal, calcium has the attractive feature of two valence electrons. Using the standard Russell-Saunders notation of $^{2S+1}L_J$ to describe the total angular momentum of the atom, calcium has an electronic ground state of

$$1s^2 2s^2 2p^6 3s^2 3p^6 4s^2 \quad {}^1\mathrm{S}_0. \tag{2.15}$$

This ground state has no fine or hyperfine structure due to the absence of a nuclear spin. The two outer electrons can have spins aligned anti-parallel or parallel, resulting in singlet and triplet energy level schemes respectively. An energy level

Isotope	Natural Abundance [%]	Isotope shift [MHz]	Half Life
40	96.94	0	Stable
41	10^{-12}	166	10^5 Years
42	0.65	393	Stable
43	0.14	554	Stable
44	2.09	774	Stable
46	10^{-3}	1160	10^{15} Years
48	0.19	1513	$> 10^{19}$ Years

Table 2.2: The abundances and half life of each of the calcium isotopes [79]. The isotope shifts are for the $^1S_0 -^1 P_1$ transition relative to ^{40}Ca.

diagram is shown in Fig. 2.9, and gives the relevant transition wavelengths and corresponding transition rates that are relevant to the work described in this thesis.

The $^1S_0 -^1 P_1$ transition is the line most often used for first-stage laser cooling alkali earth-like atoms [80]. The short upper-state lifetime of the $^1P_1$ level results in a large natural linewidth. This makes the line ideal for Doppler cooling, recalling from Section 2.1 that the force an atom experiences increases with a decreasing absorption-emission cycle time. It was this transition that Kurosu and Shimizu used to first laser cool calcium in 1990, just three years after the first MOT of sodium atoms [81].

At an energy between that of the ground and first excited states, calcium has a $^1D_2$ state that provides an additional path for an electron to decay back to the ground state. The branching ratio for an electron to decay from $^1P_1$ into the $^1D_2$, rather than to the ground state, has been measured to be 1 (± 0.15) $\times 10^5$ [82]. Once in this state, the electron has a lifetime of 3.1 (± 0.3) ms [83]. Experimentally this lifetime has been measured to be around 2.5 ms [84, 85]. A more recent measurement of the lifetime used a time-of-flight technique and found the lifetime to be (1.5 ± 0.4) ms [86]. For a system of calcium atoms in a

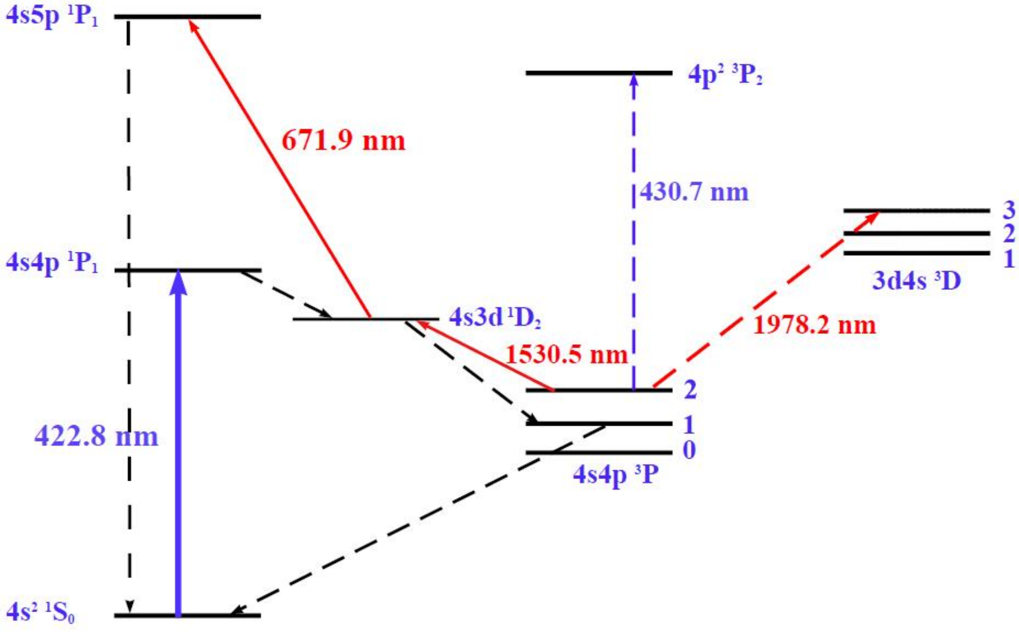

Figure 2.9: The energy level diagram for a neutral ^{40}Ca atom. The energy level spacing is not to scale and only transitions relevant to this work are shown.

MOT, there is a lifetime of approximately 20 ms before all of the atoms leak into this D state and have eventually populated metastable states and are hence lost from the cooling cycle.

The ^{88}Sr energy level structure is very similar to that of ^{40}Ca and also has a low lying $^1D_2$ state. Kurosu and Shimizu demonstrated using a 717 nm laser that the lifetime of a strontium MOT could be increased by pumping atoms straight from the $^1D_2$ state to a higher lying $^1P_1$ state. This repumping is achieved in calcium with laser at 672 nm. After a few cycles on this transition the atoms return to the ground state, increasing the number of atoms that can be trapped and cooled. The $^1D_2$ state has 5 degenerate Zeeman sublevels that have their energies shifted due to the presence of the magnetic field component of the MOT. The magnitude of the Zeeman shifts within the region of the atomic cloud is smaller than the natural linewidth of the transition and so atoms in any of the Zeeman states are pumped by a single frequency laser.

Atoms in the 3d4s $^1D_2$ state spontaneously decay to 4s4p$^3P_2$ and 4s4p$^3P_1$

Transition	Excited state lifetime [s]	Centre wavelength [nm]	I_{sat} $[\frac{\mathrm{mW}}{\mathrm{cm}^2}]$
^{1}S$_0$-4^{1}P$_1$	4.6×10^{-9}	422.792	60.0
^{1}D$_2$-4^{1}P$_1$	83×10^{-9}	671.954	0.8
^{1}D$_2$-5^{1}P$_1$	1.3×10^{-3}	1530	4.46×10^{-6}
^{1}S$_0$-^{3}P$_1$	3.85×10^{-3}	657.460	190×10^{-6}

Table 2.3: The excited state lifetimes, centre wavelengths [65, 82] and saturation intensities of relevant transitions in calcium.

with a branching ratio of 1:5 respectively [81]. It is important to note that the branching from the main transition is weak and that atoms in a MOT can be cooled to near the Doppler temperature before they decay to the ^3P states. The $^3P_2$ level is metastable with a lifetime of 118 minutes, representing the leak out of the cooling cycle [87].

The lack of a nuclear magnetic moment in the ground state means traditional evaporative cooling cannot be used to create a ground state quantum degenerate gas in a magnetic trap [27]. Theoretical studies have therefore suggested making use of the long lived ^3P state, which for calcium, is filled with atoms at a rate of 2×10^{10} atoms per second [87, 88]. Experimentally this has been realised and could be used to explore the rich collision physics that has been predicted for anisotropic interactions between ^3P atoms [89].

In LS coupling transitions between the singlet and triplet states are forbidden. However, the spin-orbit interaction allows electric dipole transitions to take place. Transitions between the two energy level schemes have very narrow linewidths and are known as intercombination lines. Due these narrow linewidths the transitions have been adopted by the optical atomic clock community as a reference oscillator [46].

The first intercombination line to consider is the 1530 nm transition, which links the $^1P_1$ and $^1D_2$ energy levels and represents the leak from the strong cooling 423nm cooling transition. Stimulating this transition should drive atoms in $^3P_2$

back to the ^1D state and allow atoms to decay to the ground state through $^3P_1$, essentially emptying the $^3P_2$ state.

The 657 nm $^1S_0$-$^3P_1$ intercombination line is a prime candidate for an optical atomic clock [50]. The appeal comes from the narrow natural linewidth of 400 Hz, which also happens to give a Doppler temperature in the nano kelvin range, opening up the possibility of laser cooling to Bose-Einstein condensation. However, this narrow linewidth does not provide a large enough acceleration to allow the creation of a MOT directly. Schemes have been created that artificially broaden the lifetime of the state to allow direct laser cooling, this in turn increases the linewidth of the transition [57]. Cooling atoms using the main cooling transition and transferring them into a dipole trap would support the atoms against gravity and allow them to be laser cooled on the intercombination line [58].

Although not used in this work, a 430 nm laser has been used to pump atoms from the the metastable 4^3P_2 state back into cooling cycle by using the higher lying 5^3P_2 state [90]. However, as the photons required to stimulate this transition are of higher energy, pumping this transition results in heating of the atoms.

Chapter 3

Hardware

3.1 Vacuum system overview

For all experiments that involve laser cooling of dilute gases, it is critical that collisions between the atoms of interest and background molecules are kept to a minimum. This is achieved by using an ultrahigh vacuum (UHV) system, inside which, the background pressure is typically lower than 10^{-5} Pa (10^{-7} mbar).

During the vacuum system's design process, the element that was to be laser cooled had to be taken into account. Unfortunately, as can be seen from Fig. 2.8, calcium must be heated to a relatively high temperature to provide sufficient vapour pressure, when compared to the alkali metals. Heating calcium to these high temperatures results in the evaporated atoms possessing a large mean velocity, which is unsuitable for direct trapping when using the vapour-cell MOT technique. This means that the calcium vacuum system needs to incorporate a few additional platforms to facilitate laser cooling; a Zeeman slower and deflection chamber. A schematic showing the main components of the vacuum system is shown in Fig. 3.1. A pneumatic valve is also shown in the figure, its purpose was to provide a means of isolating the two ends of the chamber, allowing maintenance to be carried out at one end of the system, while the other end could remain under vacuum. This also significantly reduced the time to bring the entire system to low pressures after a number of power cuts experienced during 2008.

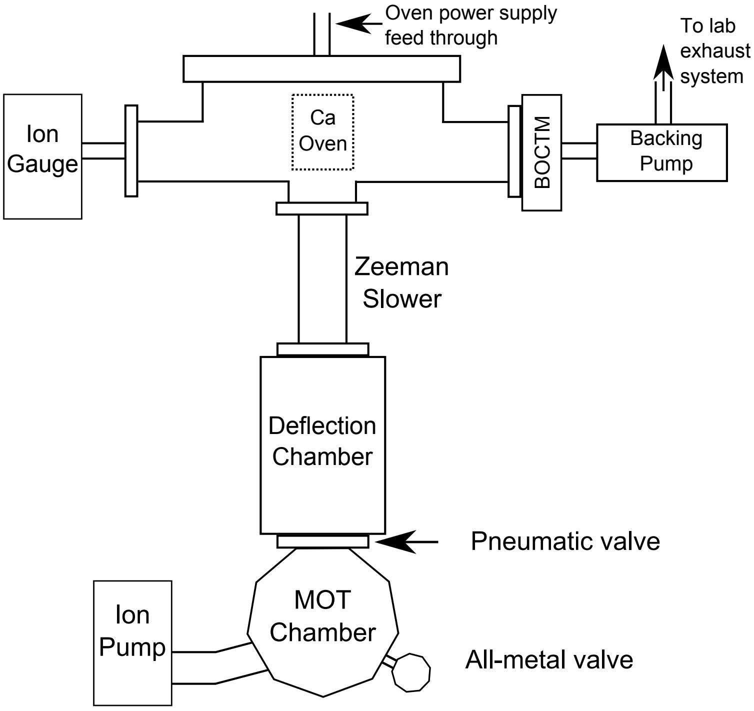

Figure 3.1: A schematic of the vacuum apparatus as viewed from above. Solid calcium is heated in the oven to produce an atomic beam that propagates through the Zeeman slower. The slower increases the number atoms with slow velocities within the beam. These atoms are then directed into the MOT chamber by a 2D molasses in the deflection chamber. The pressure inside the system was typically 10^{-5} Pa during experiments.

3.1.1 Vacuum pumps

The system was pumped below atmospheric pressure using a combination of commercial vacuum pumps. When all the sub-components of the vacuum chamber were sealed together, the system was then pumped to a pressure of 10^{-3} Pa by a BOC Edwards turbomolecular 250 l/s pump (BOCTM in Fig. 3.1). This pump was operated continually throughout all of the experiments in this thesis. Since the turbo pump requires an initial pressure of 10^{-1} to operate, an Edwards PB25 rotary pump, attached to the turbo's exhaust, was used to initially reduce the pressure inside the chamber and allow the turbo pump to reach optimum pumping speed. Although the pressure in the chamber was already significantly reduced by these two pumps the pressure had to be be reduced further to ensure that the MOT lifetime was not dominated by background collisions.

A Varian Starcell Valcon Plus, 40 l/s, ion pump was fixed to a port on the MOT chamber and was used to reduce the chamber pressure to 10^{-5} Pa. The ion pump, like the turbo pump, continually worked on the system during experiments, but unlike the turbo pump does not have any moving parts and therefore does not couple mechanical vibrations to the MOT chamber.

A Kurt Lesker ion gauge (KJL4500) was used to provide a rough measure of the pressure in the chamber. However, at low pressures the current drawn by the ion pump was used as more sensitive measurement of the pressure inside the MOT chamber. This is done by using a current-pressure chart provided by the manufacturer of the ion pump [91].

3.2 The calcium oven

An oven was developed that would generate temperatures high enough to provide a sufficient vapour pressure when it was used to heat granules of calcium; the finished oven is shown in Fig. 3.2. The oven was designed to have two stainless steel caps, each with a flange diameter of 35 mm and an inner diameter of 17 mm, into which the calcium granules were loaded. To allow the vaporised calcium to escape from the crucible a 7 mm diameter hole was drilled in the upper cap. Two, hollow, copper caps, with a 34 mm outer diameter were fixed and then placed over each end of the crucible, the lower of which was shaped to allow a tight fit over the bottom half of the crucible. The upper cap allowed space for 19, 10 mm long, 1 mm diameter nozzles to be stacked together in a hexagonal structure, held together by two copper clamping pieces, to be fitted between its inner edge and the crucible. These nozzles provided collimation of the atoms emerging from the crucible.

Two Thermocoax, twin core, swaged heaters were wound around the outer surface of the copper shell. The front and rear parts of the oven were heated independently, and the temperatures at both ends were measured with K-type thermocouples. When the system was reduced to low pressures and experiments were being performed, the oven was raised to a temperature of 770 K by delivering 20 W of electrical power to each of the heaters. The top of the oven was kept approximately 20 K warmer than the rear of the oven to ensure that calcium could would not condense inside the small capillaries.

The oven was mounted on a DN75 conflat flange which provided the electrical feedthroughs for the heaters and thermocouples. The entire assembly was then mounted into the vacuum system where it was surrounded by a 50 mm diameter, water cooled, copper pipe, in order to minimise direct heating of the vacuum chamber.

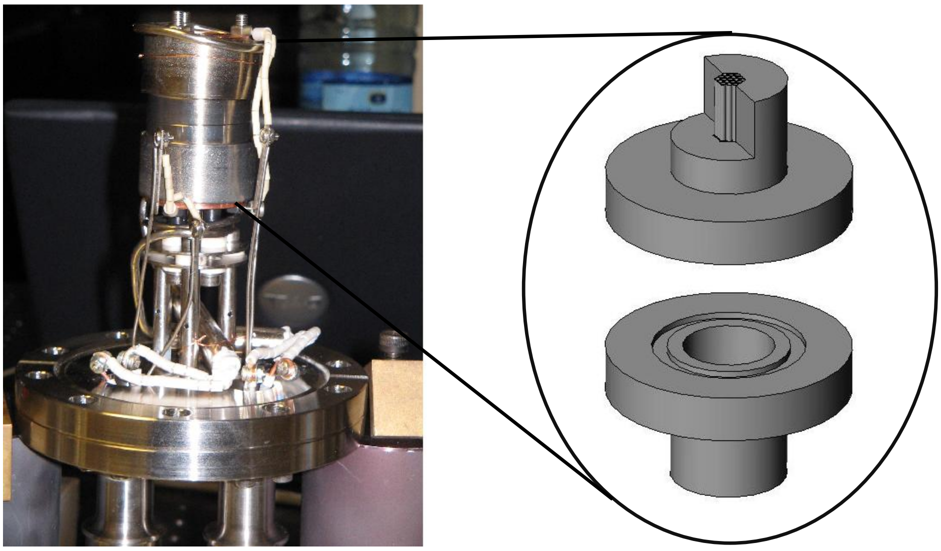

Figure 3.2: The photograph on the left shows the oven before it was fitted into the vacuum system. The heating wires can be seen wrapped round the top and bottom of the oven. The diagram to the right shows the inside of the oven. The lower section in this diagram is the crucible where calcium is loaded.

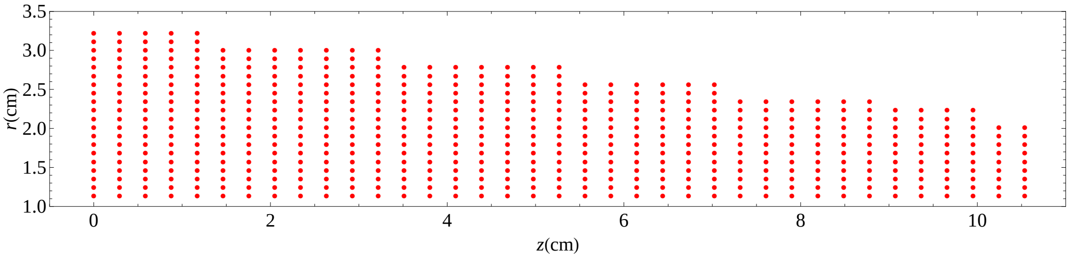

Figure 3.3: The coil windings of the Zeeman slower solenoid. Each red point represents the centre of a layer of wire wrapped round the water cooled pipe. Each winding is symmetric around the $z-$axis.

3.3 Zeeman slower

In 2006, Dr. Luke Maguire designed and built the Zeeman slower for the calcium experiment. Traditional Zeeman slowers can often be over 1 m long, taking up a large amount of space on the optical bench. However, since calcium is a relatively light atom and the energy of the photons used for cooling is large, atoms can be slowed over small distances. By using a laser beam that produces a modest deceleration of $0.3a_{\rm max}$, atoms in the atomic beam can have their velocity reduced from 490 m/s to 55 m/s by a slower which is only 11 cm long.

The solenoid that was used to create the Zeeman magnetic field was wound around a custom pipe which was 13 cm long. The pipe was designed to have a thin channel underneath its outside diameter and have connectors at either end to permit a water supply to be attached and allow water to flow through the channel. The purpose of the water flow was to remove the 40 W of heat generated by the solenoid when the maximum 10 A of current was passed through it. The magnetic field that the solenoid was required to generate was calculated using the theory in section 2.1.2.

Once the Zeeman slower was constructed, the on-axis field, generated by 10 A flowing through the solenoid, was measured using a Hall probe. The data points shown in Fig. 3.4 are the measured values of the field along the axis and are compared to the solid line, which is the ideal field required to slow atoms from

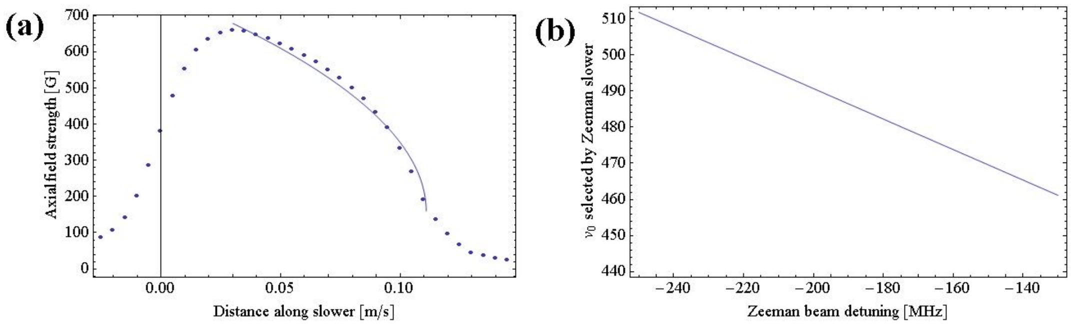

Figure 3.4: (a) Data points are the measured values of the magnetic field by a Hall probe along the centre axis of the slower. The solid line indicates the ideal magnetic field to slow ^{40}Ca atoms from 490 m/s to 55 m/s using counter propagating laser beam that produces a constant deceleration of $0.3a_{\text{max}}$ and has a detuning $\delta = -220$ MHz from resonance. Part (b) shows the initial velocity selected as a function of the Zeeman beam detuning from resonance, over the range permitted by the AOM.

longitudinal velocity of 490 m/s to 55 m/s and was calculated using Eqn. 2.9.

As described in section 2.1.2, if the peak value of the magnetic field is fixed, detuning of the Zeeman laser gives control over the initial velocity class which is slowed. Experimentally, this was achieved using an acousto-optic modulator. The capture velocity as a function of laser detuning is given in Fig. 3.4 (b).

When the Zeeman slower was tested, it was realised the water cooling was not sufficient to remove the heat produced by the solenoid. To stop the wire reaching temperatures in excess of 50 °C, a length of Tygon tubing was wrapped around the outside of the solenoid and connected to the laboratory water supply. This additional water cooling removed enough heat to keep the solenoid at room temperature while it operated with the maximum current flowing.

The distribution of velocities for atoms within the atomic beam is given by [92]

$$f(v) = \frac{2v^3}{v_0^4}\exp(-v^2/v_0^2), \tag{3.1}$$

where $v_0 = \sqrt{2k_{\text{B}}T/m}$ is the most probable velocity and m is the atomic mass. As described in section 2.1.4, the Zeeman slower can slow atoms with a velocity up to the capture velocity, v_c, and slows all atoms traveling slower than this to the desired final speed. Therefore, it is desirable to know what fraction of the total distribution is actually slowed by the slower, this is given by

$$\int_0^{v_c} f(v)\, dv \; = 1 - \left(\frac{v_0^2 + v_c^2}{v_0^2} \exp(-(v_c^2/v_0^2)) \right) . \tag{3.2}$$

Therefore, a Zeeman slower with a capture velocity of 490 m/s, acting on a beam of ^{40}Ca atoms at 490 °C will capture around 12 % of the distribution.

3.4 Deflection chamber

The oven was used to collimate the atomic beam such that the divergence from the propagation axis is less than 6°. However, even with this small angle, the transverse velocity is still relatively large at 60 m/s (for an oven temperature of 770 K). These speeds produce a beam width of almost 2.5 cm at the Zeeman slower exit. Without a reduction of the transverse velocity the beam would continue to expand and become unmanageable by the time the beam reaches the MOT chamber. The deflection chamber is used to reduce the atomic transverse velocity components and remove Zeeman slowed atoms from the rest of the beam.

A single laser beam with a 12 mm diameter and a power of ∼10 mW was retroreflected in a figure-of-four geometry using two mirrors placed at an angle of incidence of 22.5°, see Fig 3.5. For a laser beam of this diameter, the atoms slowed by the Zeeman slower spend several damping times in the molasses and leave in a direction orthogonal to the molasses beams. This results in a deflection of the beams by an angle of 12.9° in the vertical plane and into the direction of the MOT chamber.

The chamber itself consists of a rectangular stainless steel block with the dimensions 70 × 70 × 140 mm and 10 conflat ports. The ports at each end serve as the entrance and exit for the atoms of interest, while the laser beams enter through anti-reflection coated windows. To prevent the atomic beam from

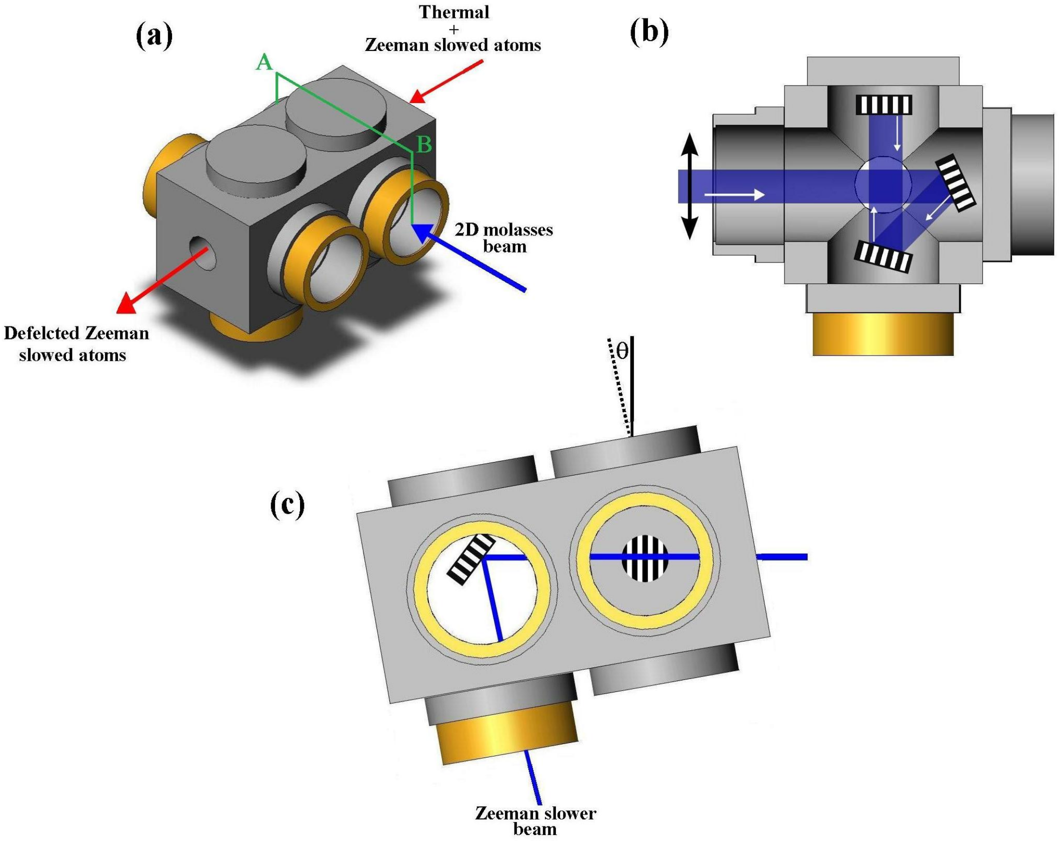

Figure 3.5: The deflection chamber. (a) Atoms enter and are transversely cooled by a 2D molasses then exit the chamber, leaving the thermal atoms to collide with the chamber. (b) The cross-section A-B. The view of the 2D molasses, as seen by atoms entering the chamber. (c) The Zeeman slower laser beam entering the chamber.

directly striking a window, the Zeeman laser beam enters from the underside of the chamber and is directed towards the oven using a silver coated mirror, fixed at ∼40° to the horizontal.

3.5 MOT chamber

The MOT chamber was designed to give substantial optical access to a cold cloud of calcium atoms trapped at its centre. The chamber was originally designed to accommodate the beams required to create the tetrahedral lattice crated by a

CO_2 laser, as described in [58]. A large amount of optical access is required for such a system and this is not typically found in standard commercial parts. As a result a custom MOT chamber was commissioned.

The custom chamber had to have at least 6 ports for the MOT beams and 8 ports for the CO_2 laser to allow both traps to operate simultaneously. In total, the MOT chamber was designed to have 22 ports, 20 of which could potentially be used for optical access, taking the vacuum pumps and atomic beam access into account. A minimum MOT beam size of 1 cm was required to ensure that any trapped atoms that decayed into the $^3P_1$ could be recaptured. This constraint lead to a minimum port size for the MOT beams to be 40 mm.

The chamber was machined in the Photonics group workshop by Mr. Robert Wylie, from a block of 316 LN stainless steel. To be compatible with additional standard vacuum components, each of the ports were machined to have a ConFlat edge, this also done in the workshop. A similar chamber was built previously for a project in Durham, which investigated a CO_2 tetrahedral lattice for rubidium atoms [93].

The main body of the vacuum system in its typical operating state is shown in Fig. 3.6, with the oven on the far left and the MOT chamber on the far right.

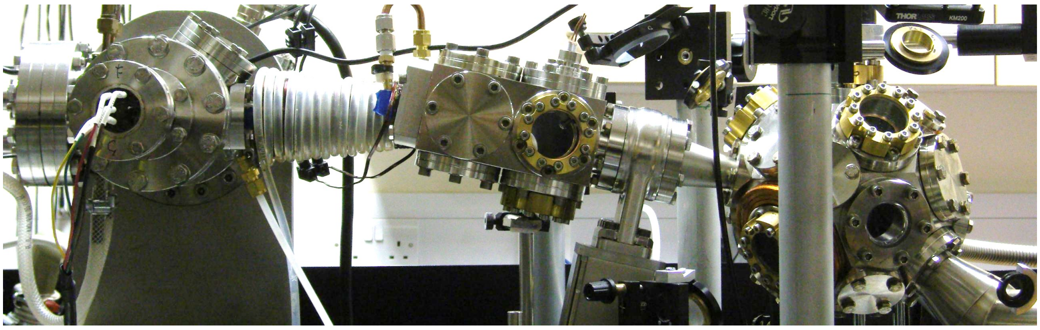

Figure 3.6: An image of the vacuum system. The oven chamber is on the far left, while the MOT chamber is on the far right.

3.5.1 Viewports

In their raw form, traditional glasses are unsuitable for viewports in laser cooling experiments due to their transmission waveband and the reflections from their flat surfaces. The glass for viewports needs to be specially selected for the wavelength of light intended to be used. Even when the correct glass is chosen anti-reflection (AR) coatings are required to minimise the reflected power. The Doppler cooling effect is very sensitive to an imbalance in the intensity in each of the beams. Since the experiment makes use of retroreflected beams, it is essential that losses from the windows are minimised. The windows used were made from a fused silica substrate coated with an AR coating that provides a transmission of 99.2% at 423 nm and a transmission of 99.6% at 657 nm.

Due to the AR coatings and specific glasses required for windows in laser cooling experiments, commercially available viewports are often expensive or just not available. As a result there are a number of methods that describe how to build viewport assemblies [94]. The FokTek windows were incorporated into a modified version of the design presented in [95].

Each viewport was created from four main parts: a 2 3/4” flange (Kurt Lesker; HN-0275SS), a sealing washer made from an alloy wire (97.5% Lead, 1.5% silver, 1% tin), a FokTek (J4S1) circular window (6 mm thick, 44.5 mm diameter) and a brass clamping flange to hold the assembly together.

The solder rings were made from a lead alloy commercially available from the Indium Corporation of America and has a circular diameter of 0.78 mm. It has a high melting point of 327 °C and outgassing from the wire is negligible, making the wire suitable for baking to moderate temperatures. The washer was made by cutting a length of the solder and placing both ends close together and then applying a large force to compress the wire to a thin annulus. Two seals were required for each viewport assembly.

Each component of the window was stacked then held together by twelve M4 screws on the clamping flange, which screwed into pre-drilled holes in the flange.

Figure 3.7: Two views of the homemade viewports that were used on both the MOT chamber and deflection chamber to minimise reflections of the laser light coupled into the vacuum system.

The screws had to be tightened to 1.5 Nm to squeeze the washers on either side of the glass and create a glass to metal seal. Each viewport was mounted onto the vacuum system with large bore copper gaskets using the knife edges of the system.

The viewport assemblies were tested after being mounted to the vacuum system and were found to operate well for a system pressure of 10^{-5} Pa. Testing was done using an SRS RGA200 residual gas analyser to monitor the amount of helium within the system as the exterior was surrounded by a helium rich atmosphere.

Chapter 4

Frequency doubling and laser stabilisation

4.1 423 nm source

Due to its short upper-state lifetime, the $^1S_0 -^1 P_1$ transition in ^{40}Ca is ideal for laser cooling neutral calcium atoms to mK temperatures. The blue light at 423 nm required to drive this transition can be generated from two main sources: diode lasers and frequency doubled infrared (IR) lasers.

Diode lasers are a common source of light for the alkali atom laser cooling experiments and have been reliably generating coherent radiation in the near-infrared for a number of years [75]. If the diode is used in combination with an external grating a tunable, narrow linewidth output can be achieved. These external cavity diode lasers are a common tool in the field of spectroscopy and would be an ideal candidate for a 423 nm source if a suitable diode were available. Some groups have used low power ($\sim$ 30 mW) laser diodes, that have a central wavelength close to 423 nm, for spectroscopy of calcium [96]. However, these blue diodes are now a rarity and few exist due to the drive towards creating diodes centered on the 405 nm; the wavelength required for Blu-Ray DVD technology.

Nonlinear crystals offer an alternative approach to generating blue light [97, 98]. As a reliable, narrow linewidth, IR source was available in our lab, 423 nm light for the calcium experiment was generated by frequency doubling its output using a periodically poled potassium titanyl phosphate (ppKTP) crystal. Details on how this light was generated, as well as how it was stabilised to the ^{40}Ca transition, are given in this chapter.

4.2 Second harmonic generation: theory

Classical optics is an approximation and as the intensity of a light beam propagating through a medium increases, linear optics fails and a material's optical properties must be described by nonlinear optics [99]. Due to the high intensities of light required to enter this domain, optical nonlinear processes in materials could only be witnessed after the invention of the laser [100].

There are a number of solid state gain media that provide a stable high-power output, but these sources are mainly limited to the IR region of the spectrum. By utilising of the nonlinear response at high intensities of certain crystals, light from readily available IR sources can be converted into its harmonics, providing useful coherent light in the violet region of the spectrum [101].

For an optical wave propagating through a medium, its associated electric field induces a time varying electric polarisation, $P(t)$. At low incident intensities, this polarisation wave interacts with the optical wave and reduces its phase velocity. Classical optics measures the reduction in phase velocity via the refractive index, n. At high intensities, the polarisation can be described as a power series in the incident electric field, $E(t)$,

$$\begin{aligned} P(t) &= \epsilon_0 \left(\chi^{(1)}E(t) + \chi^{(2)}E^2(t) \cdots + \chi^{(n)}E^n(t)\right) \\ &= P^{(1)}(t) + P^{(2)}(t) \cdots + P^n(t) \qquad (4.1) \end{aligned}$$

where $\chi^{(n)}$ are the nonlinear optical susceptibilities corresponding to the nth order of the electric field. For the purpose of this thesis, only second order nonlinear interactions will be considered and it is assumed that the polarisation wave responds instantaneously to the electric field.

A laser beam, with an electric field strength described by

$$E(t) = Ee^{-i\omega t} + c.c., \tag{4.2}$$

where *c.c.* is the wave's complex conjugate, that is incident on a crystal with $\chi^{(2)} \neq 0$, will create a nonlinear polarisation

$$P^{(2)}(t) = \epsilon_0 \left(\chi^{(2)} E^2(t) = 2\chi^{(2)} EE^* + (\chi^{(2)} E^2 e^{-2\omega t} + c.c.) \right). \tag{4.3}$$

Therefore, the resulting second-order polarisation consists of a DC contribution and a contribution at a frequency of 2ω. The latter contribution leads to the generation of radiation at the second-harmonic of the incident electric field and is known as second harmonic generation (SHG) [102]. This nonlinear process is used experimentally to create a source of 423 nm light for the calcium experiment. Note that only crystals lacking a centre of inversion can have $\chi^{(2)} \neq 0$.

4.2.1 Nonlinear susceptibility

The second order nonlinear susceptibility, $\chi^{(2)}_{ijk}$, where the indices ijk refer to the directions along each cartesian axes, is a third order tensor with 27 elements. For most crystals, Kleinman symmetry can be assumed, therefore, it is convenient to introduce the contracted notation

$$d_{il} = \frac{\chi^{(2)}_{ijk}}{2}, \tag{4.4}$$

where $jk \rightarrow l$ as

jk	11	22	33	23, 32	31, 13	12, 21
l	1	2	3	4	5	6

Every crystal can be categorised by one of 32 classes, each of which has its own symmetries. The combination of Kleinman symmetry and the crystal's own spatial symmetry generally simplifies the d_{il} matrix to have few non-zero elements.

KTP is classed as a type $mm2$ crystal and so has the second order nonlinear susceptibility described by the matrix [103]

$$d_{il} = \begin{pmatrix} 0 & 0 & 0 & 0 & d_{13} & 0 \\ 0 & 0 & 0 & d_{23} & 0 & 0 \\ d_{13} & d_{23} & d_{33} & 0 & 0 & 0 \end{pmatrix}, \tag{4.5}$$

where $d_{13} = 1.95$ pm/V, $d_{23} = 3.9$ pm/V and $d_{33} = 15.3$ pm/V [104].

The polarisation component that gives rise to second harmonic generation is described by the scalar relationship [102]

$$P(2\omega) = 2d_{eff}\epsilon_0 E(\omega)^2, \tag{4.6}$$

where d_{eff} is an effective nonlinear coefficient, which depends on the direction of propagation and polarisation of the incident fields and is calculated from the elements of the d_{il} matrix [105].

4.2.2 Phase matching

As the fundamental and second harmonic beams propagate through the crystal, they each experience a different refractive index and therefore propagate at different phase velocities. As the direction of the power flux between the interacting waves is determined by the relative phase between the beams [106], the resulting dispersion produces a change in direction power flow. Hence, the intensity of the second harmonic wave is determined by the phase difference between the wavevectors, $\Delta k = k_2 - 2k_1$, where $k_i = n_i\omega_i/c$. For an incident fundamental intensity, I_ω, the intensity of the second harmonic is given by [102],

$$I_{2\omega} = \frac{2\omega^2|d_{eff}|^2L^2}{n^3c^3\epsilon_0}\text{sinc}^2(\Delta kL/2)I_\omega^2, \tag{4.7}$$

where L is the crystal length. The coherence length, $l_c = \lambda/4(n_2 - n_1)$, is the distance over which the relative phase between the fundamental and second harmonic waves changes by π, it is also the half period of the growth and decay cycle of the second harmonic. Typically, l_c is of the order of only a few μm, which is not long enough to provide sufficient buildup of the second harmonic.

In order to achieve the maximum conversion efficiency along the length of the crystal, it is crucial to make $\Delta k = 0$, i.e. the fundamental and second harmonic should propagate at the same phase velocity, this process is known as phase matching. When phase matched, the second harmonic intensity grows quadratically along the crystal length, as shown by the red curve in Fig. 4.1 [106]. However, from Eqn. 4.7 it is clear that if the phase velocities are not matched, the second harmonic intensity oscillates between zero and a maximum value, which determined by the fundamental intensity, Fig. 4.1 (green curve).

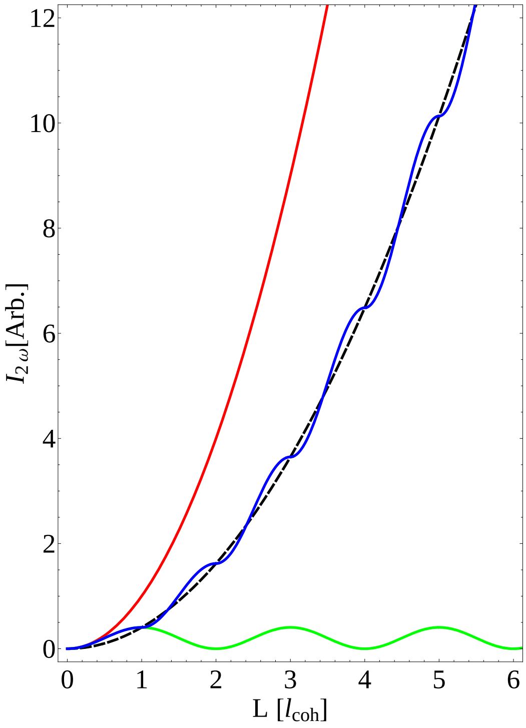

Figure 4.1: The growth of the second harmonic intensity as a function of the propagation length through a nonlinear crystal. The red curve is the case when the waves are critically phase matched, i.e. $\Delta k = 0$. The green curve is the growth of the second harmonic when there is no phase matching between the waves (Eqn. 4.7). The blue curve shows the second harmonic growth when the waves are quasi-phase matched in a periodically polled crystal [106].

Practically, phase matching can be achieved in birefringent crystals by carefully choosing the angle at which the fundamental enters the crystal, as the refractive index is a function of the incident angle. This process is known as *critical* phase matching. There are a number of problems associated with this method, with walk-off being one of the most troublesome. This is an effect produced by the difference in the direction of power flow, given by their Poynting vectors, between the two waves and results in the waves propagating in slightly different directions and therefore a reduced interaction length.

Quasi-phase matching

As can be seen from Fig. 4.1, when the waves are not phase matched the second harmonic intensity begins to drop after a distance l_c in the crystal, at which point the phase difference is π. However, by repeatedly inverting the nonlinear coefficient after a distance l_c, along the full length of the crystal, it is possible to enable continuous second harmonic growth along the length of the crystal. This method of SHG is known as quasi-phase matching (QPM) and removes the difficulty of critical phase matching, since the restraint of $\Delta k = 0$ is removed.

A technique called periodic poling generates domains of altering polarity in ferroelectric nonlinear crystals, which changes the sign of the effective nonlinear coefficient. The process involves applying an electric field to the ferroelectric crystal using a cathode of length l_c, with a period $\Lambda = 2l_c$ [107]. Using a quasi-phase matched technique, generating 423 nm light requires a commercially available crystal with a poling period of 4.2 μm.

QPM allows for the direction of propagation and polarisation to be chosen to maximise d_{eff}, unlike birefringent phase matching where the propagation directions are severely constrained. Another major advantage for using a QPM system is that all of the waves propagate along the same crystal axis so there is no spatial walk-off. The wavelengths for QPM are also only limited by the transmission band of the crystal, compared to traditional phase matching where only a wavelength that can be critically phase matched can be used, this allows the propagation axis through the crystal to be chosen arbitrarily. The selection of the axis for QPM is usually chosen to be the axis with the largest nonlinear coefficient. As can be seen from Eqn. 4.4, the largest nonlinear component of the nonlinear susceptibility for KTP is d_{33}, permitting more than double the SHG efficiency of any other propagation direction.

The build up of the second harmonic in quasi-phase matching depends critically on the polling period, as the crystal has a non-zero thermal expansion coefficient, $\Lambda = \Lambda(T)$ and the phase matching condition for a periodically polled crystal

$$\Delta k_{QPM}(T) = 4\pi\frac{n_{2\omega}}{\lambda} - 4\pi\frac{n_{\omega}}{\lambda} - \frac{2\pi}{\Lambda(T)}, \tag{4.8}$$

for a fundamental wavelength λ [108]. As a result, controlling the crystal temperature provides allows fine control over the crystal poling period, and hence the efficiency of the SHG process.

4.3 Second harmonic generation: experiment

4.3.1 Infrared laser source

The workhorse laser for the calcium experiment was a Coherent Verdi-V8 laser. The commercially available laser generally required no attention and operated reliably for over two and a half years. Due to this reliability, the laser can be regarded as a black box that generates 532 nm laser light. The interface unit for the laser allows the output power to be set between 0 W and 8 W with a 10 mW resolution. An electric chiller was used to keep the laser head at a constant temperature of 17 °C and ensured stable operation.

The light produced by the Verdi was used as the pump source for a Coherent MBR-110 Ti:sapphire laser. The MBR-110 is a source of single frequency light that is tunable over the range 770 nm - 880 nm [109]. Various elements inside the laser are used, in conjunction with an external interface electronics unit, to produce a narrow linewidth, TEM_{00} laser beam that is polarised horizontally with respect to the table. Due to the high power incident on the Ti:sapphire crystal, a water supply was connected to the water inputs of the laser head, allowing water to flow past the crystal at a rate of 0.5 l/min, removing any dissipated heat and again ensuring stable operation. Under optimum conditions, the maximum output power from the laser was 950 mW at 846 nm for 8 W of pump power. However, in normal operation, 7 W of pump light would produce $\sim$ 600 mW of infrared light, sufficient for the calcium experiment.

The MBR-110 electronics unit has a number of useful modes of operation, two of which were used frequently in different experimental situations. The *scan* mode allows the user to select a range of frequencies to be scanned over a range of up to 30 GHz, whilst remaining single frequency, this was useful for spectroscopy of the calcium resonances. An *offset* mode allows fine control of the output laser frequency to a resolution of 10 MHz. This control was used as a method of setting the output to approximately the frequency required to generate resonant blue light, the external stabilisation system, described later in section 4.5, was then used to lock the laser frequency.

The *scan* mode was used frequently, however, the scan range input was not calibrated to the scan range output by the laser. Using a Toptica FPI-100 Fabry-Pérot interferometer [110], it was found that the frequency input (in MHz) on the control unit should be multiplied by 0.64 to represent the actual frequency range scanned by the laser. The linewidth of the laser was also measured to be 1.5 ± 0.5 MHz using the same FPI. The linewidth of the ti:sapphire laser was not completely optimised since, even when the beam was frequency doubled, it was still narrow enough to probe the natural linewidth of the strong cooling transition.

After a daily ‘warm-up’ period of 20 minutes, the laser would operate reliably over a 12 hour period and only need serviced around once per month to optimise the cavity mirrors. Note that a strong laminar flow unit was required to operate above the laser to ensure that no dust particles entered into the cavity.

4.3.2 Nonlinear crystals

Two nonlinear crystals were used to frequency double the infrared light from the Ti:sapphire laser; one was used in a single pass configuration and the other was placed into a resonant enhancement cavity to generate the higher powers required for the calcium MOT.

The crystals were designed to an identical specification, both were 10 mm long, 1 mm thick and 5 mm tall and formed from c-cut ppKTP. The periodic poling period of each crystal was 4.2 μm ($\Lambda = 2l_c$) and was achieved using the electric field poling along the c-axis of the crystal. The end facets of both crystals were AR coated for 846 nm and 423 nm light.

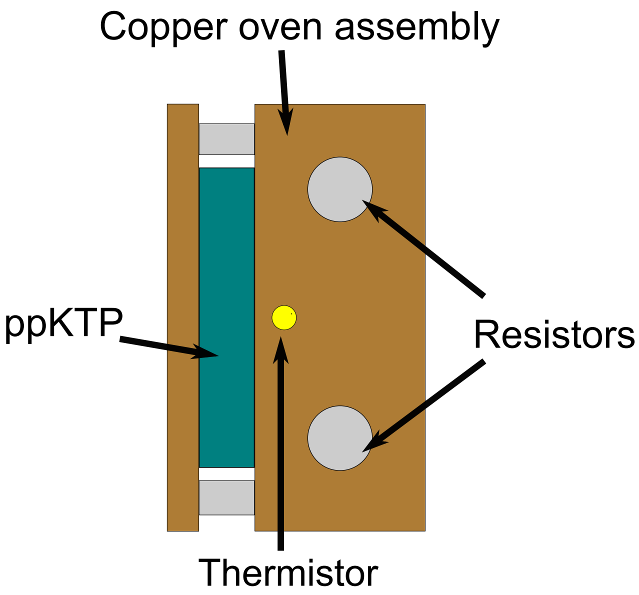

Figure 4.2: The ppKTP crystal was spring loaded into a copper oven. The oven temperature was controlled by the current flowing through the resistors, regulated by a temperature controller that received temperature feedback from the thermistor.

Each of the crystals were fixed to an individual copper oven and clamped as shown in the Fig. 4.2. The copper oven was embedded with two resistors, which acted as the heat source, and a 10kΩ thermistor, all of which was housed in a PTFE casing. The oven (and casing) were constructed to give maximum optical access to the crystal, whilst using enough insulation to maintain temperature stability. The resistors for each oven had a series resistance of 10.54 Ω and were driven with $\sim$ 1 A of current supplied by a Wavelength Electronics MPT-5000 temperature controller, operated in resistive heater mode. This kept each of the crystals at a constant temperature of around 75 °C.

A number of parameters determine the efficiency of the SHG process within the crystal. The first of these is the incident polarisation, this was easily controlled by a $\lambda/2$-plate positioned prior to the crystal. By rotating the waveplate about its axis, the maximum second harmonic output was obtained empirically. The efficiency also depends on the poling period of the crystal, which changes with crystal temperature.

Crystal temperature

A measurement of the SHG conversion efficiency as a function of crystal temperature was carried out for each of the two crystals used in the laser cooling experiment. The Ti:sapphire output frequency was set to twice the ${}^1S_0 -{}^1 P_1$ calcium resonance using a wavemeter and the beam was focused to a spot size of 17 μm inside the centre of the crystal, using a two lens system.

Fig. 4.3 shows the second harmonic power produced as the crystal temperature was varied from 69 °C to 77 °C for a single pass configuration. The maximum second harmonic power generated was 4.2 ± .2 mW at a temperature of 73.5 °C, for a fundamental power of 600 mW this corresponds to a conversion efficiency of 1.17 ± 0.02 %/W, in line with previous measurements [111]. As expected from Eqns. 4.7 and 4.8, the data follow a sinc-function, which has a FWHM of 1.9 °C.

The same experiment was repeated for both crystals, the second crystal produced a similar maximum power of 3.6 ± .2 mW but at the slightly lower tem-

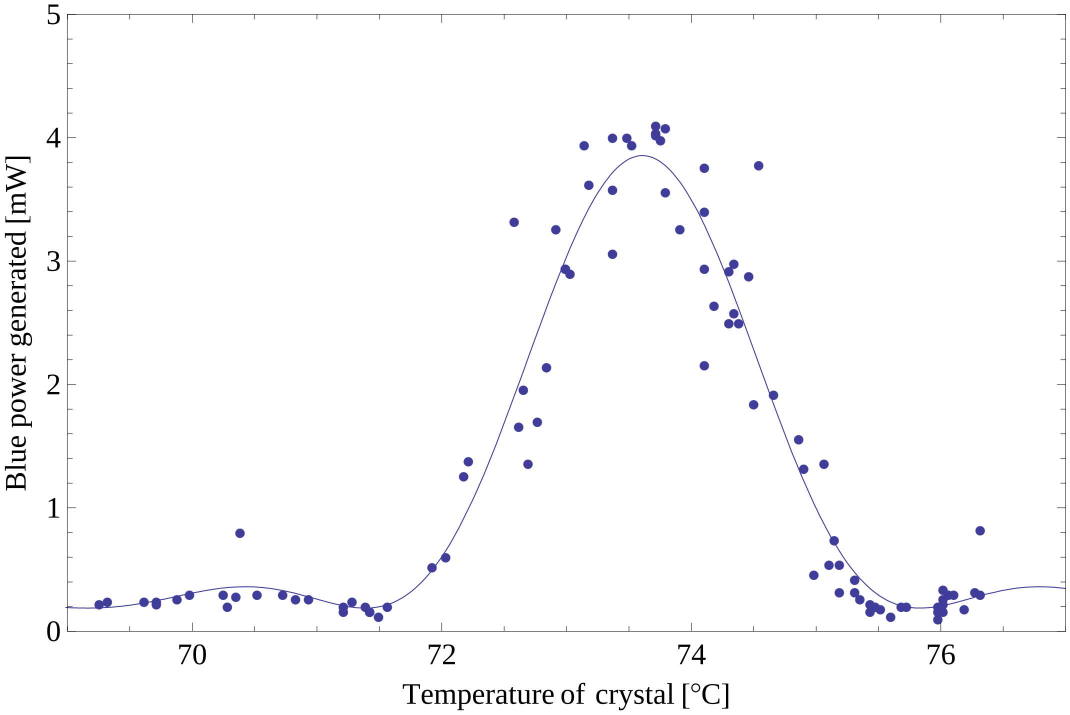

Figure 4.3: The SHG power generated as a function of crystal temperature for: a 10 mm long ppKTP crystal, 600 mW of 846 nm fundamental light focused to 17 μm at the centre of the crystal. The data fit well to a sinc function (see 4.7) with a measured FWHM of 1.9 °C.

perature of 70.2 °C. There may be a number of reason for the inconsistencies in optimum temperature, although it is expected that a slightly different poling period is the likely cause [107].

Techniques have been recently developed that allow direct observation of the domains in periodically polled materials [112]. The technique shows that many irregularities occur during the poling process and can be a cause for lower than expected conversion efficiencies from a specific crystal. These probing techniques will hopefully lead to improved poling processes and result in crystals that produce higher conversion efficiencies.

4.4 SHG setup

Light from the Ti:sapphire laser was used in a single pass configuration with a ppKTP crystal to generate 423 nm light that was used to stabilise the laser to the atomic transition. By placing the ppKTP crystal at the focus of a telescope, which was used to collimate the Ti:sapphire output, 4-5 mW of blue light was generated with negligible loss of IR power. This blue light was then used in the laser stabilisation setup apparatus, see Fig. 4.4.

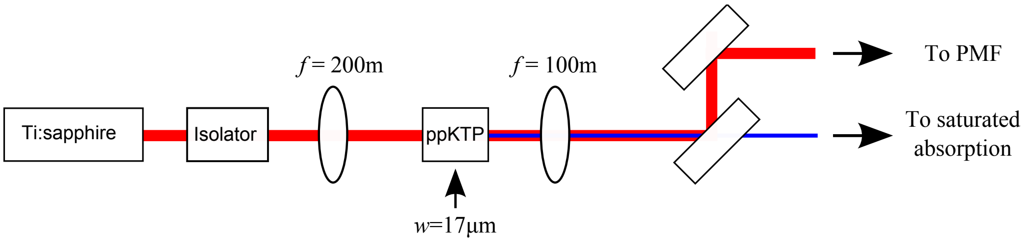

Figure 4.4: A ppKTP crystal, placed at the focus the Ti:sapphire collimation telescope. For 600 mW of IR and a at crystal temperature of 74.2 °C, 4.2 mW of blue light was generated. It was separated from the IR beam using a mirror with a transparent substrate and reflective coatings for IR wavelengths.

The 4 mW generated by a single pass of the IR light through the ppKTP crystal was not sufficient to drive the laser cooling experiment, at least 80 mW of 423 nm light was required for the Zeeman slower, deflection stage and MOT beams. High second harmonic power output can be achieved by placing a nonlinear crystal inside a resonant enhancement cavity [113, 114]. The following section details the design and construction of a resonant enhancement cavity used for generating sufficient blue light for the calcium experiment.

4.4.1 Resonant Enhancement Cavity

A resonant enhancement cavity consists of two or more mirrors that are set up in such a way that allows light to propagate round a closed path. If the incident light is resonant to the cavity and properly mode matched to it, the resulting circulating power is far above the the incident power. By placing a ppKTP crystal inside the cavity, the higher fundamental power can be utilised to produce a higher power of SHG.

The resonant enhancement cavity was chosen to have a ring configuration, as shown in Fig. 4.5. The cavity was created from two plane mirrors, M1 & M2, and two curved mirrors M3 & M4 (radius of curvature (ROC) = 50 mm), in a bow-tie arrangement. All of the mirrors were high-reflection (HR) coated for 846 nm (except M1 which has a reflection coefficient $R = 0.95$) and anti-reflection (AR) coated for 423 nm. The crystal, housed in the oven, was mounted on a vertical translation stage at the tight focus between the two curved mirrors. There were two main advantages of using a ring cavity over a linear cavity. First, there was minimal feedback from the enhancement cavity back to the pump laser, ensuring stable operation. Second, as the fundamental beam only propagates round the cavity in one direction, almost all of the second harmonic was emitted in one direction.

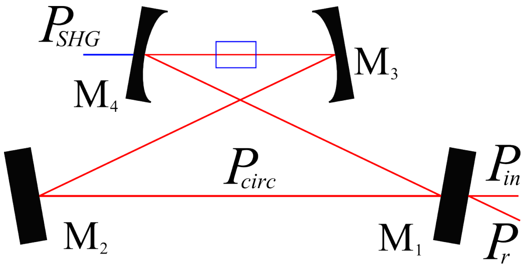

Figure 4.5: The ring cavity design for resonant enhancement of the incident fundamental wave.

The cavity was designed under the assumption that the incident IR light had a Gaussian transverse profile [115], this allowed the complex beam parameter, $q(z)$, to be used to describe the propagation of the laser beam throughout the system [116],

$$q(z) = \left(\frac{1}{R(z)} - i\frac{\lambda}{\pi w^2(z)} \right)^{-1}, \tag{4.9}$$

where λ is the incident wavelength, $R(z)$ is the radius of curvature of the wave-front and $w^2(z)$ is the beam waste. Winlase is commercially available software that calculates $q(z)$ at all points throughout an optical system for a given set of initial parameters. Winlase outputs the beam diameter and ROC graphically as a function of z throughout the system, reducing the time required to design a cavity.

It is essential for a cavity to be stable in order for the laser to circulate many times around the cavity and produce a build up of power. A cavity is defined to be stable when the complex beam parameter is reproduced after one round trip i.e. the beam waist and radius of curvature are the same after the beam passes through the entire cavity. Mode matching is the process of matching the incident light $q(z)$ to the cavity $q(z)$ at M1, practically this was achieved by manipulating the incident beam with a lens pair before it entered the cavity. Winlase also determines the cavity stability for a particular design and will only output data for a stable cavity.

For a mode matched cavity, only one longitudinal and transverse cavity mode is excited. However, the amount of light that is coupled into the resonant mode is determined by how well the cavity and incident beam are impedance matched [117]. This can be achieved by matching the reflectivity of the input coupler to the losses experienced by a beam that has propagated once round the cavity [98].

After careful alignment of the coupling lenses at the input to the cavity, $\sim$ 85% of the incident light could be coupled into the cavity. Fig. 4.6 shows the signal detected by a photodetector monitoring the light reflected from M1 as the cavity length is scanned using a PZT fixed to M2.

Before the curved mirrors were fixed into the cavity configuration, they were placed in the path of a 600 mW, 846 nm laser beam. Using a photodiode, the power transmitted through the mirror was measured and recorded. Once the cavity was completely assembled and resonating with the ppKTP crystal inside, the same photodiode was used to measure the transmitted power from the curved

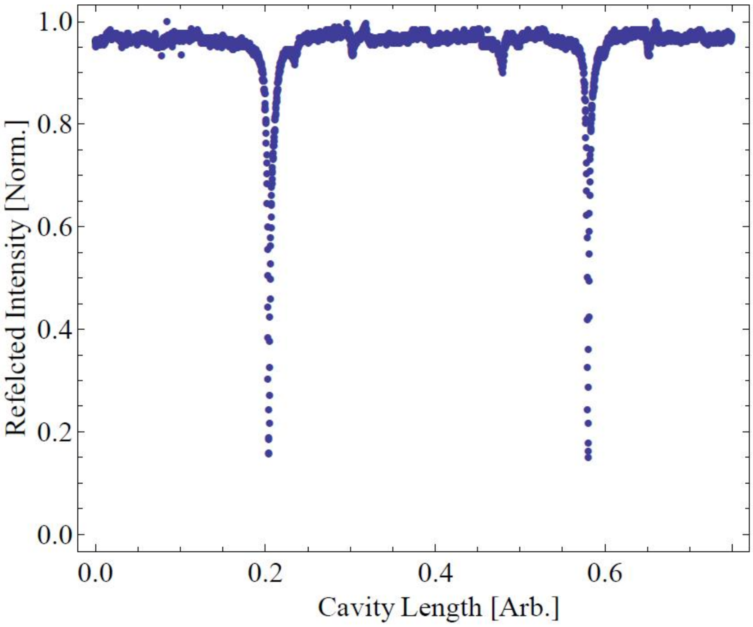

Figure 4.6: The light reflected from the input coupler was measured with a photodiode as the cavity length was scanned over one free spectral range. Input coupler had 5 % transmission.

mirrors once again. From the known ratio of incident power to transmitted power, the circulating pump power was found to be 6.4 W on resonance, for ~350 mW of 846 nm incident light.

Cavity stabilisation

To provide constant second harmonic power from the enhancement cavity, the cavity length had to be stabilised to ensure that it was always resonant with the fundamental beam. A number of schemes that actively counteract the effect of mechanical vibrations and temperature changes, which cause the cavity to drift from resonance, have been developed [118, 119]. The Hänsch-Couillaud technique does not require modulation of the incident light to provide active feedback to the cavity, reducing the complexity and expense associated with the the locking system. Fig. 4.7 shows the setup used to lock the enhancement cavity and brief review of the technique follows [120].

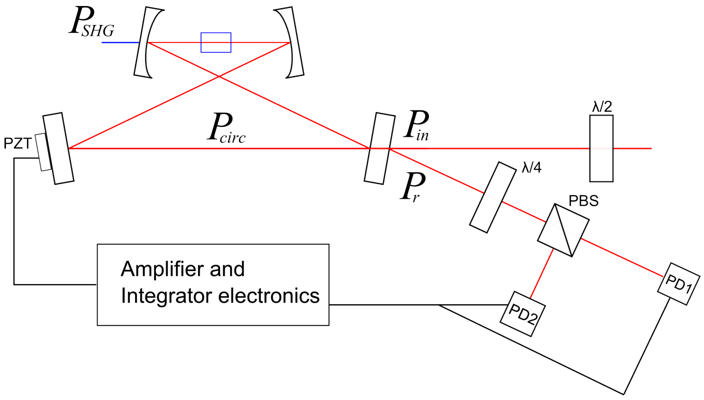

Figure 4.7: The experimental setup for the enhancement cavity containing the ppKTP, locked on resonance using the Hänsch-Couillaud locking technique.

Light incident on the enhancement cavity, with a power P_{in}, strikes the input coupler and enters the cavity. The $\lambda/2$ plate is used to align the polarisation of the incident light to an angle θ relative to the optic axis of the birefringent crystal within the cavity, as this determines the polarisation axis of the system. The incident beam's electric field can therefore be decomposed into two orthogonal, linearly polarised components, polarised parallel and perpendicular to the transmission axis of the crystal,

$$E^i_{||} = E^i \cos\theta, \quad E^i_{\perp} = E^i \sin\theta, \tag{4.10}$$

where E^i is the amplitude of the incident beam. The perpendicular component of the beam is reflected by the input coupler and is used as a reference. The parallel component is coupled into the cavity and experiences a frequency dependent phase shift as it is reflected. If any phase difference is introduced between the two beams, the polarisation of the light reflected from the input coupler will be elliptical. The amplitude of the reflected wave, E^r, for each polarisation is given by [121]

$$E^r_{||} = E^i_{||}\,\sqrt{R_1} - \frac{T_1 R}{\sqrt{R_1}} \frac{\cos\,\delta - R + i\,\sin\,\delta}{(1-R)^2 + 4R\,\sin^2\,(\delta/2)}\ , \tag{4.11}$$

where δ is the phase accumulated by the wave as it propagates around the cavity, R_1 and T_1 are the reflectivity and transmissivity of the input coupler, and R is the amplitude ratio of the field as it propagates through a number of round trips through the cavity. The reflected component is given by

$$E_{\perp}^{r} = E_{\perp}^{i}\sqrt{R_1}. \tag{4.12}$$

When the cavity is resonant, each of the polarised components are real and both waves are in phase. However, when the cavity is off resonance, the parallel component of the field gains a phase shift relative to the perpendicular component, resulting in the reflected beam being elliptically polarised. The magnitude of the ellipticity of the reflected polarisation therefore a measure of the frequency detuning from the cavity resonance.

Experimentally, the elliptically polarised light is decomposed into its components using a $\lambda/4$ plate and a polarising beamsplitter cube, see Fig. 4.7. The fast axis of the waveplate is aligned at 45° to the polarisation axis of the beamsplitter, to resolve the elliptical light back into linear components. The intensity of light emerging at the output of the beamsplitter, I_a and I_b, was then monitored using two photodiodes. By detecting the difference in the intensities [120],

$$I_a - I_b = I^i 2\cos\theta \, \sin\theta \frac{T_1 R \, \sin\delta}{(1-R)^2 4R \, \sin^2\delta/2}, \tag{4.13}$$

an error signal could be obtained, which was then input to an integration unit that was used to drive the PZT mirror within the cavity, keeping the cavity on resonance. Fig. 4.8 shows the typical error signal that was produced by the subtraction of the photodiode currents.

When the cavity was originally constructed the error signal was highly asymmetric about the x-axis and not suitable for input into the locking electronics. The asymmetry was produced by a thermal induced bistability [98]; when the round-trip path length is decreased by the PZT mirror in the cavity, the circulating pump power increases, as does the second harmonic power. The crystal absorbs photons from both of the beams, which results in a local temperature increase, and hence an increase in the optical path length. The cavity resonance then shifts to a shorter cavity length, resulting in a slow increase of the circulating

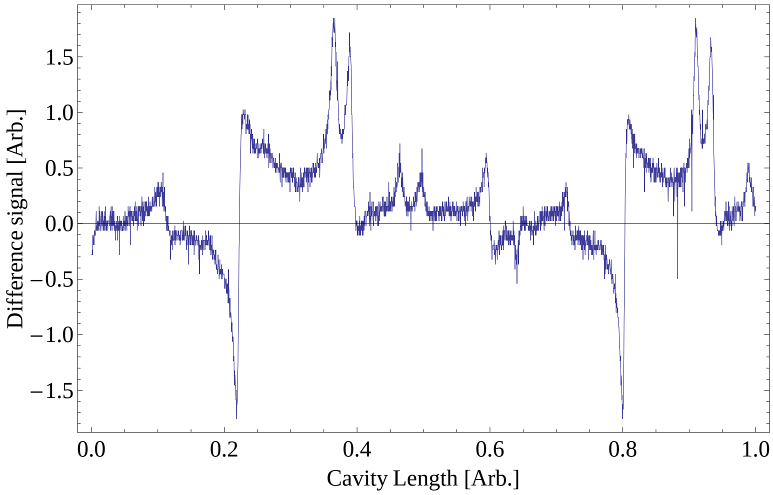

Figure 4.8: The difference signal between PD1 and PD2 as the cavity length was scanned using the PZT.

pump power. As the cavity is tuned just beyond the resonance, the circulating pump power decreases at an accelerated rate due to the sudden decrease in temperature in the crystal.

To reduce the effect of the bistability, the spot size at the crystal's centre was increased beyond the ideal value of 17 μm, in 1 μm steps until a quality error signal was produced and could be used for locking. A spot size that is not equal to the optimum value results in a poorer conversion efficiency for the SHG process, however, the lower powers did allow the cavity to be locked. Unfortunately, no single cavity parameter could be changed to alter the size of the focused spot in the crystal, so a number of cavities had to be designed and tested.

The design parameters for the cavity which produced the most power, but also produced a reliable error signal, are given in Tab. 4.1. The measured circulating pump power of 6.4 W and second harmonic output power of 100 mW produces a single pass conversion efficiency of $\sim$ 0.5 %/W, less than the 1.2 %/W measured in section 4.3.2. However, even with this lower conversion efficiency, a stable output power of 100 mW could be achieved continuously for over four hours, using the above locking scheme.

Parameter	Value
M1 reflectivity	95 %
M3 & M4 ROC	50 mm
Mode matching spot size	178 μm
Spot size in crystal	25.75 μm
Crystal temperature	73.5 °C
Typical incident power	450 mW
Typical SHG output power	100 mW
M1/M2 separation	120 mm
M3/M4 separation	65 mm

Table 4.1: The optimum parameters used for the resonant enhancement cavity.

4.5 Laser stabilization to an atomic reference

The Ti:sapphire laser that was used as the light source for the fundamental wave in the SHG process, described in the previous sections, required an absolute reference to the $^1S_0 -^1 P_1$ ^{40}Ca transition. There are a number of well developed, Doppler-free techniques that can be used to produce a reference source for laser stabilisation and they are often employed in laser cooling experiments [122, 123]. Similar to the locking technique used for the resonant enhancement cavity, an absolute frequency reference requires an anti-symmetric line with a steep zero-crossing, to allow electronic feedback to compensate for any laser drifts. Spectroscopic techniques that have been developed to generate these reference signals can be classified into two groups; modulation free techniques [124] or those that require to internally or externally frequency modulate the laser light [125, 119].

Saturated absorption is an attractive technique for frequency stabilisation and is commonly used in laser cooling experiments [126]. The narrow spectral features that can be resolved provide good long-term stability, however, the basic signal is a symmetric Lorentzian that does not have a zero-crossing. Frequency modulating the laser light produces a dispersive signal that passes through zero, allowing feedback electronics to stabilise the laser to the centre of the absorption feature [127]. However, frequency modulation of the laser light introduces complication to the setup and may cause disruption further down the optical path, especially if the laser is internally modulated.

A dispersive signal can be produced without frequency modulating the laser beam, this can be obtained from the difference between two saturated absorption features generated by pump beams with a small frequency difference. The small frequency difference between the beams has been shown previously to be obtained by using either two acousto-optic modulators (AOM) [128] or using the zeroth and the first order beam of an AOM as the pump beams [129]. Neither of the setups modulate the AOMs to allow for phase sensitive detection and as a result both are prone to low frequency noise.

At room temperature, the vapour pressure of calcium is low when compared with atoms typically used in laser cooling experiments, see section 2.2.1. As a result, the commercial vapour cells that are often used for saturation spectroscopy are not available for calcium. Home made vapour cells often have relatively complex designs [130] and require to heat the calcium source to high temperatures [131]. However, there are reliable alternative methods, for example those that make use of an atomic beam [123] or hollow cathode lamps (HCL) [132] to produce a reference signal.

The following section describes a simple saturated absorption setup that employs a commercial HCL to generate an error signal, which is then used to stabilise the Ti:sapphire laser. The technique has been demonstrated to lock the laser relative to the calcium resonance over a number of hours and is sensitive enough to also provide a frequency reference for the less abundant calcium isotopes.

4.5.1 Lamp characterisation

The central feature of the Hamamatsu L2783-20NE-Ca, the HCL used in the setup, is a cylindrical hollow cathode with a 3 mm bore that is lined with solid calcium. The lamp is contained in a glass T-shaped bulb, which is filled to a pressure of 6 torr with a neon buffer gas. The lamp was connected to a power supply, which provided a potential of around 680 V. Although the applied voltage was varied during the experiments, care was taken not to exceed the 20 mA maximum current specified by the manufacturer. The neon atoms in the gas become charged at the anode when the potential is applied and accelerate toward the cathode, resulting in calcium atoms being ejected. The released calcium atoms can then be used for spectroscopy.

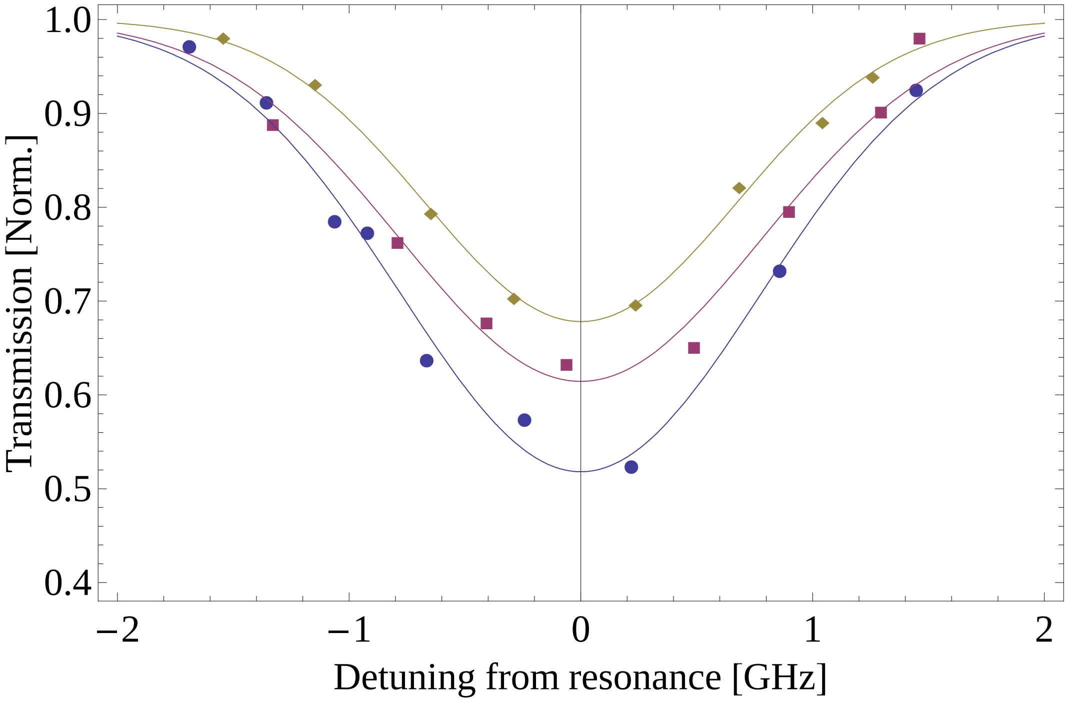

Figure 4.9: The Doppler broadened absorption profiles produced by a 423 nm, 25 μW, 0.5 mm diameter beam passing through the HCL with an applied voltage of 900 V (circles), 800 V (squares) and 700 V (diamonds). A Gaussian fit was found for the normalised data to find the maximum absorption and FWHM of the absorption profile.

With the aid of a Coherent WaveMaster wavemeter, the Ti:sapphire laser was adjusted to output a wavelength of 845.584 nm. The four milliwatts of blue light, produced by the single pass of the IR light through the ppKTP crystal, was separated from the fundamental beam using a mirror with a transparent substrate and an HR coating for IR light. The blue beam was focused to a diameter of 150 μm in the centre of the lamp and reduced to a power of 25 μW, using neutral density filters. A photodiode was used to monitor the power of the light that emerged from the exit of the HCL. The Ti:sapphire laser was used to scan the blue light 4 GHz around the expected ${}^1S_0{-}{}^1P_1$ ^{40}Ca transition frequency, resulting in a fraction of the light being absorbed by the calcium atoms. The absorption profiles for three different applied voltages to the lamp are shown in Fig. 4.9, the fits are used to determine the maximum absorption. The temperature of the calcium atoms, which absorb the photons from the laser beam is related to the full-width half-maximum (FWHM) of the absorption profile via [126]

$$T = \frac{c^2 m(\Delta\omega_{FWHM})^2}{8k_{\mathrm{B}}\omega_0^2 \ln 2}, \tag{4.14}$$

where c is the speed of light, ω_0 is the transition frequency, m is the atomic mass and $\Delta\omega_{FWHM}$ is the Doppler width.

As the life of an HCL is limited [133], 680 V was typically applied during experiments as this resulted in a sufficient beam absorption for spectroscopy and also helped increase the lifetime of the lamp. A summary of the maximum absorption of the laser through the HCL and the temperature of the ejected calcium atoms for a number of voltages applied to the lamp is given in table. 4.2, which is in good agreement with previous measurements [96]. The maximum absorption was measured as a function of the power in a 150 μm diameter beam, for a constant lamp voltage of 680 V. This allowed an evaluation of the power to be used in the beam that would result in sufficient absorption but still produce a measurable signal. The data are shown in Fig. 4.10. As the maximum absorption occurs for $\Delta = 0$, the data should follow $1/(1 + I/I_{sat})$ and allow a direct measurement of I_{sat}.

Voltage [V]	FWHM [GHz]	Max. absorption [Norm.]	Temperature [°C]
900	1.9	0.48	250
800	1.8	0.38	244
700	1.6	0.32	116

Table 4.2: Data for the variation of absorption profile and calcium temperature as a function of the voltage applied to the lamp. The beam spot size was 150 μm and the beam power was 25 μW.

The curve shown in Fig. 4.10 is a fit to the data corresponding to $I_{sat} = 57.7 \pm 6$ mW/cm^2, in agreement with the accepted value of 61.9 mW/cm^2 [81].

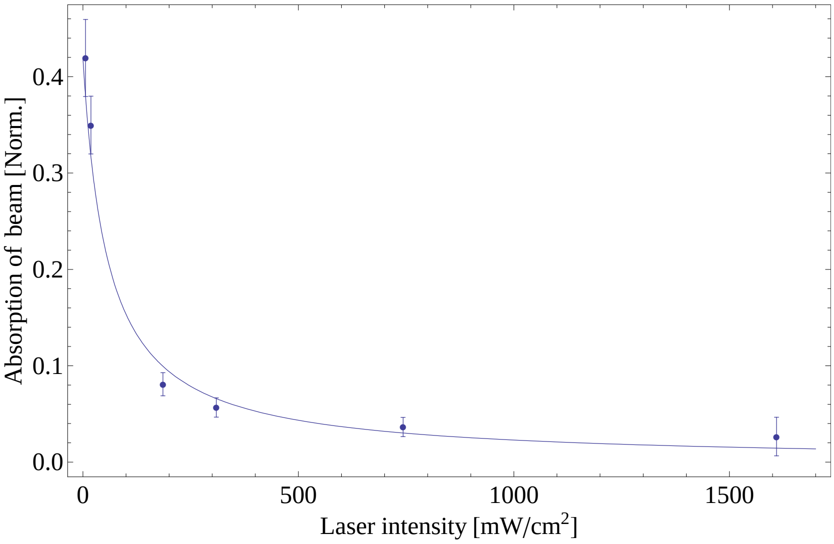

Figure 4.10: The variation of laser beam absorption with incident intensity. The laser spot size was 125 μm, while the lamp voltage was set to 680 V.

4.5.2 Saturated absorption

A typical saturated absorption setup comprises of a pump beam and a counter-propagating probe beam that simultaneously interact with an atomic vapour. By modulating the amplitude of the pump beam, phase-sensitive detection of the probe beam produces a signal that is proportional to the homogeneously broadened atomic linewidth.

Modulation can be achieved by passing the pump beam through an AOM, which displaces most of the incident light into the first order, and modulating the applied power to the device. By aligning the zeroth and first orders to overlap with the probe beam at the same position in the atomic vapour, the detected signal depends on which pump beam the probe interacts with. If power is applied to the AOM the probe interacts with the first order beam, resulting in a detected signal that is shifted by half of the AOM frequency from the zero velocity class value. If there is no power supplied to the AOM the detected linewidth is centred on the zero velocity class but is phase shifted from the previous signal by 180°. For a rapid modulation, the probe signal, as detected with a phase sensitive detector, displays an anti-symmetric lineshape with a zero-crossing at one quarter of the AOM frequency.

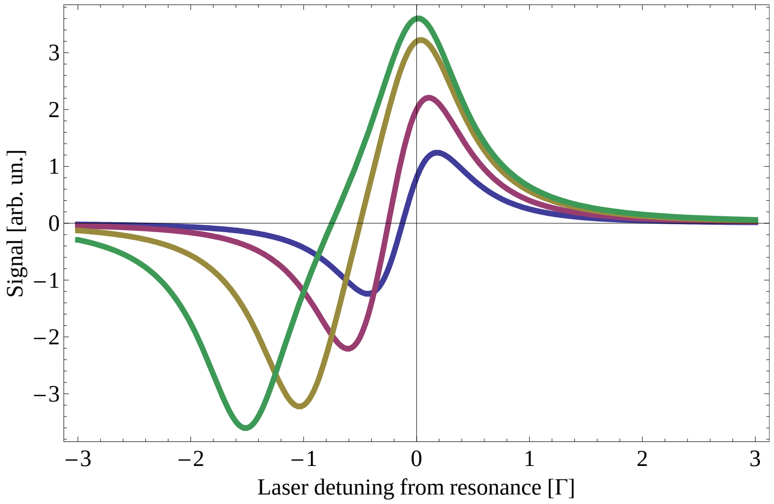

Figure 4.11: The dispersion signals for a range of AOM frequencies, calculated using Eqn. 4.15. The amplitudes were kept equal and the AOM frequencies used were ν_{AOM}= .5Γ (blue), Γ (magenta), 2Γ (gold) and 3Γ (green).

As the centre frequency is increased to the point at which the signal crosses zero, i.e. the point used for locking, also increases. For the case where the

AOM is used to create two pump beams, the observed signal is the difference of two Lorentzian profiles that are frequency shifted from each other by half the frequency of the AOM:

$$S = \frac{A_1}{(\Gamma/2)^2 + (\nu_l - \nu_0 + \nu_{\mathrm{AOM}}/2)^2} - \frac{A_2}{(\Gamma/2)^2 + (\nu_l - \nu_0)^2}, \tag{4.15}$$

where A_1 & A_2 are the amplitudes of each signal, Γ is the homogeneously broadened linewidth for the transition, ν_0 is the atomic transition frequency and ν_l is the laser frequency. Any difference in the amplitudes of the individual signals leads to a shift of the zero crossing frequency. Experimentally, there was generally a difference of ∼20 % between the amplitudes, which corresponds to an induced frequency shift of 3.5 MHz, this is relatively small when compared with the 34 MHz of the natural linewidth.

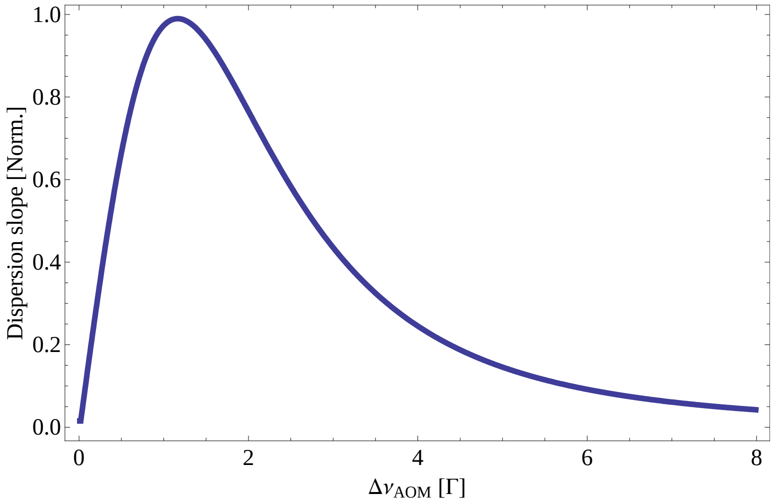

Figure 4.12: The slope of the dispersion signal, formed by two equal amplitude signals, through the zero crossing as a function of AOM frequency.

The calculated difference frequency for a number of AOM frequencies are shown in Fig. 4.11. As the AOM frequency is increased, the difference signal grows and the slope passing through zero steepens until the two individual absorption profiles separate. Therefore, the slope through the zero crossing is a measure of the suitability of the signal as a reference source for the stabilisation scheme.

Fig. 4.12 shows the variation of the slope of the dispersion signal through the zero crossing as a function of AOM frequency. It can be seen that the maximum of the curve occurs at an AOM frequency of $\sim 1.15\Gamma$, the experiment is conducted at an AOM frequency within 5% of this value.

4.5.3 Method and results

The setup used for frequency stabilisation of the Ti:sapphire laser is shown in Fig.4.13. The 4 mW of blue light was passed through an AOM driven with an RF frequency of 80 MHz. Approximately 80% of the incident light could be coupled into the +1 diffracted order beam from the AOM and independently aligned through the collimation lens from the zeroth order beam.

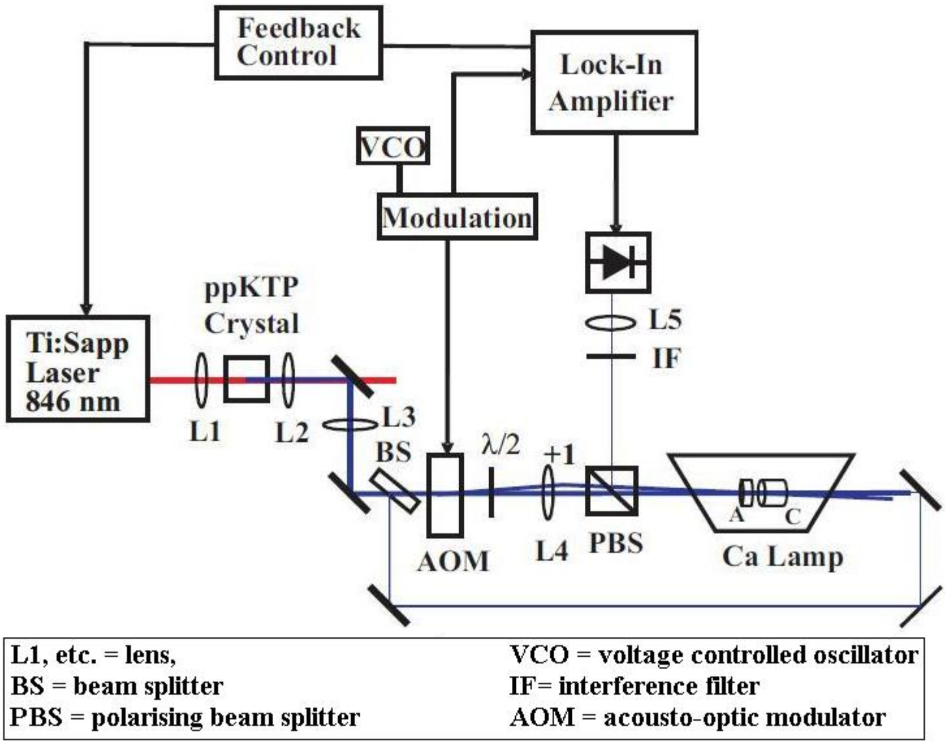

Figure 4.13: The experimental setup for the frequency stabilisation of the Ti:sapphire laser to the calcium resonance. The $\lambda/2$ plate is used to rotate the polarisation of the pump beams wrt to the probe beam. The beam marked with +1 is the first diffracted order from the AOM.

The two vertically polarised pump beams were overlapped inside the HCL along with a weak, horizontally polarised, probe beam propagating in the opposite direction. The probe beam was picked off from the main beam before entering the AOM and had a power of 300 μW. The applied RF frequency was modulated on and off at a frequency of 55 kHz, due to the efficient coupling into the first order, this essentially results in alternate switching of the pump beam at this high frequency. A 423 nm interference filter is placed in front of the AC coupled, amplified photodetector to remove the stray light produced by the HCL. The individual saturated absorption signals are obtained by only allowing one pump beam through the lamp at a time and detected using a Stanford Research Systems lock-in amplifier. Fig. 4.14 shows the individual saturated absorption signals, the red plot is the signal when the first order beam is blocked from entering the HCL, the green trace shows the signal when the zeroth order beam is blocked. The yellow trace is the signal detected by the lock-in amplifier, set with a time constant of 1 ms, when both modulated pump beams interact with the probe beam. The measured linewidth of the signal is 70 MHz, or twice the natural linewidth of the $^1S_0 -^1 P_1$ transition.

Doppler broadening effects caused by the alignment of the pump beams is kept below the natural linewidth, Γ_{nat}, by using knife-edge mirrors. However, calcium collisions with the neon inside the HCl could potentially result in homogeneous broadening or a frequency shift. The 423 nm transition in calcium is well studied in the presence of noble gases and by extrapolating from data measured at higher temperatures, at the 6 torr of neon within the lamp, there should be a broadening of Γ_p =16 MHz [134].

The pump intensities of 130 mW/cm^2 also induces a broadening of the observed linewidth, given by [3]

$$\Gamma_{total} = \Gamma_{nat}\sqrt{\frac{I}{I_{sat}} + \left(1 + \frac{\Gamma_p}{\Gamma_{nat}}\right)^2}. \tag{4.16}$$

Using the extrapolated value of Γ_p =16 MHz along with Γ_{nat} = 34.6 MHz, I_{sat} = 61.9mW/cm^2 and I = 130 mW/cm^2, the expected linewidth is 71 MHz, which is

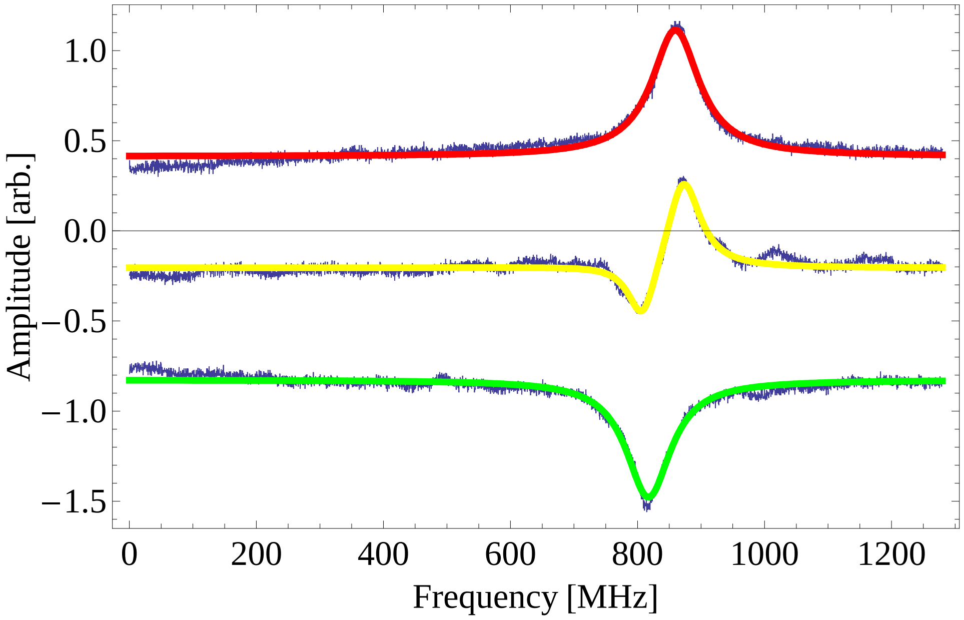

Figure 4.14: The slope of the dispersion signal, formed by two equal amplitude signals, through the zero crossing as a function of AOM frequency.

close to the measured value.

As the calcium inside the HCL cannot be used as an absolute frequency reference, the zero crossing frequency of the dispersion signal was compared to the laser induced fluorescence from a thermal beam of atomic calcium, which was excited with light incident perpendicular to the atomic beam direction of propagation. The atomic beam used for the reference is also the source of atoms for the MOT and was accessed through the spare viewports on the deflection chamber. The incident laser beam was retroreflected and aligned to ensure that the Doppler contribution to the detected signal was minimised.

Fig. 4.15 shows the dispersion signal from the saturated absorption setup and compares it with the beam fluorescence signal. As both setups used light from the same source, the signals could be obtained simultaneously, allowing a direct measurement of the zero crossing of the dispersion signal and the atomic transition frequency. The beam fluorescence is fitted with a Gaussian, which has a FWHM of 80 MHz. The lower signal is fitted with Eqn. 4.15 and has a calculated zero

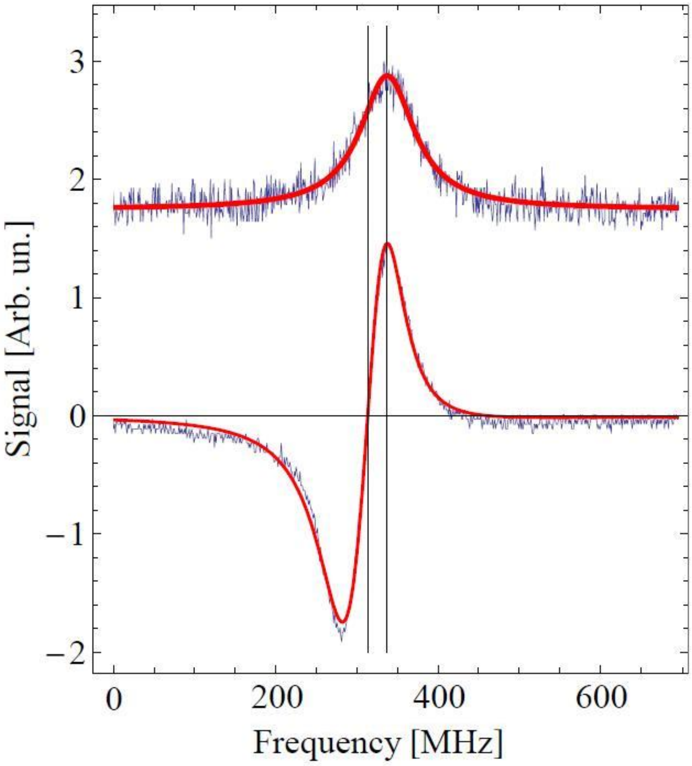

Figure 4.15: The top signal is the detected laser induced fluorescence from the atomic beam. The lower signal is the dispersion signal produced by the saturated absorption setup. The amplitude and offsets of the signals have been adjusted to allow both signals to appear in one plot. The left and right vertical lines correspond to the atomic transition frequency and zero crossing frequency, respectively.

crossing at 24 MHz to the red of the peak of the fluorescence curve.

The resonance frequency of the calcium within the HCL is shifted from the true value due to the presence of the neon buffer gas. For the pressure of neon in the HCL, the resulting in a shift of 8.6 MHz to the red [134]. For an AOM frequency of 80 MHz the resulting zero crossing should be 20 MHz to the red of the transition, adding this to the pressure shift the crossing should be -28.6 MHz from the true transition frequency, meaning the expected and measured values differ by more than 4 MHz. The reason for this could be partly attributed to amplitude differences between the two pump beams entering the HCL, however, as the amplitudes were within 20% of one another, this suggests that there are additional shifts taking place in the HCL that are unaccounted for.

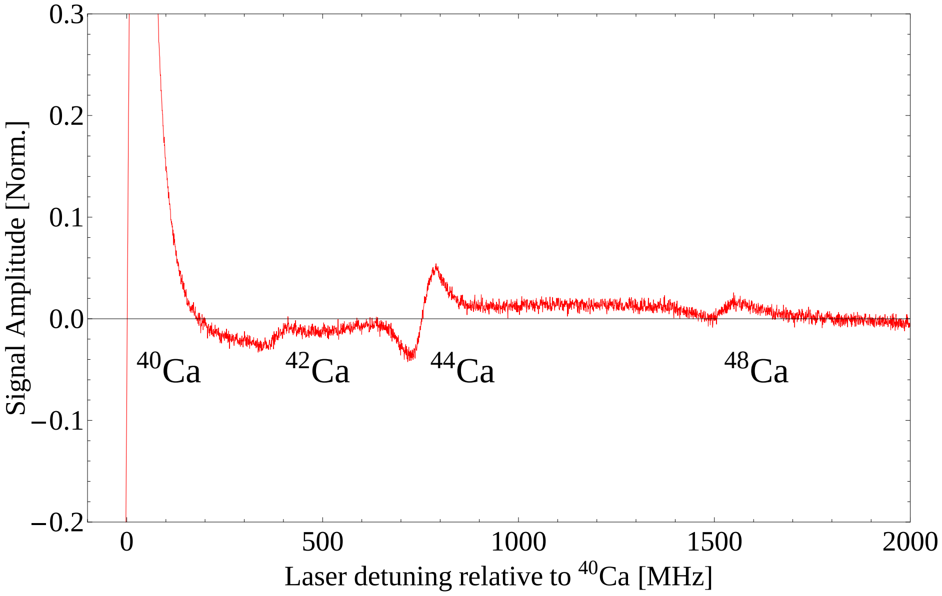

Figure 4.16: The dispersion signals for calcium isotopes, detected in the hollow cathode lamp.

The plot shown in Fig. 4.16 demonstrates the sensitivity of the technique. As the Ti:sapphire was scanned far from the ^{40}Ca $^1S_0 -^1 P_1$ resonance, dispersion curves resulting from the $^1S_0 -^1 P_1$ transitions in ^{42}Ca, ^{44}Ca and ^{48}Ca could also be observed, where the abundances range from 0.2-2%. The measured isotope shifts for each of the signals are compared to recently pulished values in Table. 4.3 [79].

Isotope	Measured [MHz]	Literature value [MHz]
^{42}Ca	390 (20)	393
^{44}Ca	765 (28)	774
^{48}Ca	1525 (39)	1513

Table 4.3: The isotope shifts, measured relative to the $^1S_0 -^1 P_1$ transition in ^{40}Ca, of three isotopes of low abundance and compared to values in the literature [79].

As the typical absorption of a beam through the HCL is around 50% (Fig. 4.9) and the cross section for the transition is 5×10^{-15} m^2, the density of atoms is 6.9×10^{15} m^{-3} [135]. Therefore, the beams interact with $\sim 10^8$ atoms of which ~ 180000 (0.2%) are ^{48}Ca.

Chapter 5

Laser diode light sources

Since its creation in 1962 [136], the diode laser has become the most common form of laser in the world today [137]. Over this time it has evolved into a compact and efficient source of coherent radiation, which has found many everyday applications. Laser diodes are inherent in barcode scanners and optical data storage devices, and we also rely on them for high speed intercontinental communication [138]. However, industry has not been the only beneficiary of mass produced laser diodes, as the range of available wavelengths has grown, researchers have employed diode lasers in their experiments as an invaluable substitute for dye lasers due to their low cost and easy maintenance [75]. The following chapter describes the setup and configuration of the various diode lasers used in the Strathclyde calcium lab. For a detailed discussion on the theory of diode lasers see [139].

5.1 Properties of diode lasers

5.1.1 Structure

Traditional lasers, such as gas lasers, typically have cavity lengths of centimeters or greater. However, diode lasers have a cavity length of only a few hundred microns. The structure of a standard diode is shown in Fig. 5.1. Optical feedback is made possible in such a small device by cleaving flat, parallel, edges when the

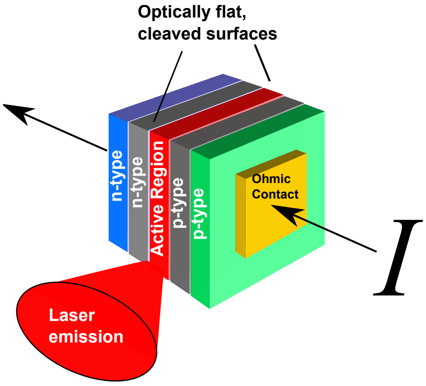

Figure 5.1: The typical structure of a standard diode laser. Feedback is achieved in the diode laser by cleaving the diode form the source with optically flat edges. Adapted from [139].

diode is first cut from the source wafer. These flat edges from a very small optical cavity, which define the longitudinal modes of the coherent light emitted. For a typical diode laser length of 400 μm the frequency spacing between each of the modes permitted to oscillate is around 100 GHz. The longitudinal mode that will actually oscillate within the cavity will be the mode with maximum gain, i.e. the longitudinal mode closest to the maximum point on the diode gain curve, see Fig. 5.2. The laser diode gain profile varies with the current injected across the bandgap and with the temperature of the diode itself.

5.1.2 Temperature and current dependence

The wavelength of the light output by a laser diode depends critically on the bandgap of the semiconductor used, which is not a parameter that can be easily changed. For calcium, there are a number of commercially available laser diodes with an output close to the wavelengths required for driving a number of atomic transitions. As the output of a diode does generally not correspond exactly to the atomic transition frequency, the diode must be tuned a number of GHz from its free running value. This is achievable by controlling the diode temperature, the injection current and controlling the light fed back to the bare diode.

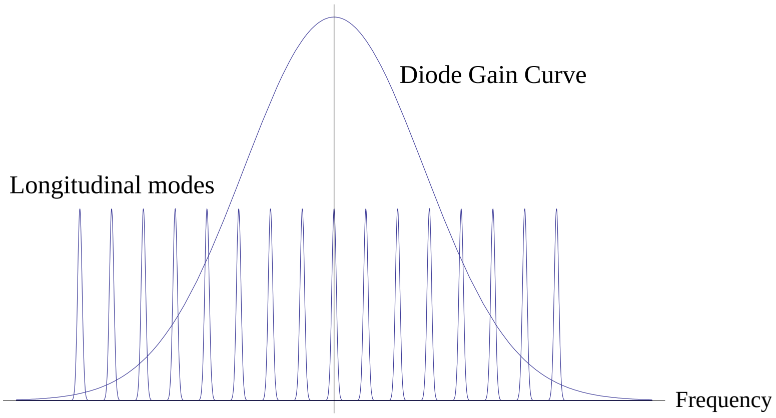

Figure 5.2: The diode gain curve is defined by the bandgap in the semiconductor. The longitudinal mode which experiences the most gain will be the mode which oscillates, in this case shown by the vertical line.

The temperature of the diode affects two properties of the diode: the length of the laser cavity (since the material has a thermal expansion coefficient) and the laser diode gain curve. For a typical laser diode an increase of one kelvin results in an increase of 0.06 nm in output wavelength [75]. This can be used as a coarse method of bringing the output to within a few hundredths of a nanometer of the desired wavelength. As temperature control systems are generally slow to react to small changes in temperatures, the injection current to the diode is used as the next stage of refinement.

Changing the injection current to the diode laser changes the charge carrier density in the diode, which in turn changes the refractive index of the active region of the diode and hence the output wavelength. However, on timescales of a microsecond this effect can be ignored [140]. The injection current also affects the temperature of the laser diode, which again has a direct effect on the output wavelength of the diode. A change of one milliamp in the injection current typically corresponds to a frequency shift of 4 GHz [54].

5.1.3 Mode-hopping

The laser diode temperature and injection current affect the frequency position of both the longitudinal modes and the diode gain curve. However, the shifts in gain curve and mode spacing due to temperature and current are different and result in a phenomenon known as mode-hopping. If the laser diode gain curve maximum occurs at a frequency between two longitudinal modes, small variations in temperature or current result in a large discontinuous shift in output frequency, see Fig. 5.3.

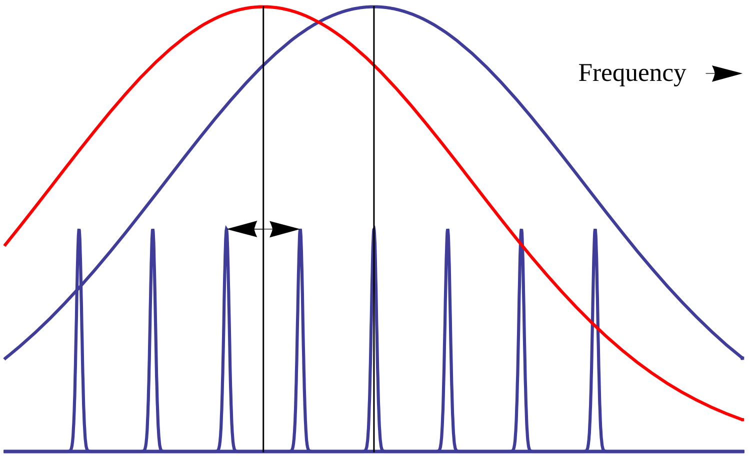

Figure 5.3: The centre of the diode gain curve at temperatures T (blue) and $T + \Delta T$ (red) correspond to a different oscillating longitudinal mode. The maximum gain at $T + \Delta T$ occurs at a frequency between two longitudinal modes, giving rise to large discontinuous frequency shifts for small changes in temperature or current.

Generally, mode-hopping cannot be well predicted and presents the technical challenge of producing a laser with a large continuous tuning range. In practice, wavelength tuning via current and temperature becomes an iterative process where both are changed until the laser operates in a region around the wavelength of interest.

5.2 External cavity diode lasers

While the output wavelength of the laser diode can be somewhat controlled by the temperature and injection current, the linewidth of the light produced by a free running laser diode can be up to tens of megahertz. There are a number of systems that have made use of the fact that diode lasers are extremely sensitive to optical feedback, and have been used to narrow the linewidth of the light output by the diode successfully [141]. As mentioned previously, mode-hops do not allow a continuous tuning of the output wavelength. External cavity diode lasers (ECDLs) are a common tool in laser cooling laboratories and solve many of the issues associated with bare diodes.

Placing a diode laser into an external cavity, which makes use of a frequency dependent reflector, such as a diffraction grating, provides a method of reducing the linewidth of the output and increases the continuous tuning range. Increasing the cavity length and feeding back a small fraction of the emitted light can reduce the linewidth by a factor of two orders of magnitude [142].

The ECDLs used in the calcium laboratory used the Littrow configuration [143], which is commonly used for diode lasers in spectroscopy. This method uses the grating to diffract the low power first order beam back to the diode's active region, while the zeroth order beam is coupled out from the cavity. The angle of the grating to the direction of propagation of the output beam defines the frequency of light reflected back by,

$$\lambda = 2\ d\ sin\ \theta, \tag{5.1}$$

where λ is the wavelength of the light, d is the distance between the grooves of the grating and θ is the angle between the grating's normal and the angle of the incident light. As small changes in grating angle correspond to relatively large changes in wavelength, a piezoelectric transducer is used to control the angle of the grating position. By changing the voltage applied to the PZT, θ can be increased, which then in turn increases the wavelength.

5.3 672 nm source

An ECDL system was used as the light source for driving the $3^1D_2 - 5^1P_1$ transition of the atoms trapped in the MOT (see sec. 2.2.2). The ECDL design is based on that of Arnold *et al* [141], a design which has previously been successfully implemented in our group [76].

A high power, single mode, diode laser (HL6545MG) was used as the light source in the ECDL. A Thorlabs LT230P-B collimation tube was used to fix the diode position with respect to a lens ($f = 5$ mm), which was used for collimating the highly divergent output. As the lens is threaded, precise control of the beam collimation can be achieved, which is essential for creating good feedback to the diode.

A commercial optical mirror mount (Newport U100-P) was used to hold both the diode/lens assembly and the grating. Fig. 5.4 indicates how the individual components are fitted together to create the ECDL. The collimation tube was fitted into a pre-drilled hole in a standard post adapter (Newport UPA-PA1), then clamped in place with a screw. The post adapter was then fixed to the mirror mount, from which a square section had been removed from the faceplate. This was to allow an aluminum block, cut with one face at an angle of 37° to the collimation tube axis, to be fixed to the mirror mount and be used as a location for the grating.

A standard, off-the-shelf, 1800 lines/mm, diffraction grating (05HG1800-500-1) was then fixed to the aluminum mount and aligned with its lines parallel to the output polarisation of the incident light. In this configuration up to 75 % of the light could be coupled out via the zeroth order beam.

To gain control of the output frequency of the laser it was essential to have well aligned feedback into the active region of the diode. The first order diffracted beam was directed back into the laser diode by using both the horizontal and vertical adjustment screws of the mirror mount. Once good feedback was achieved, small adjustments of the horizontal screw provided control over the laser fre-

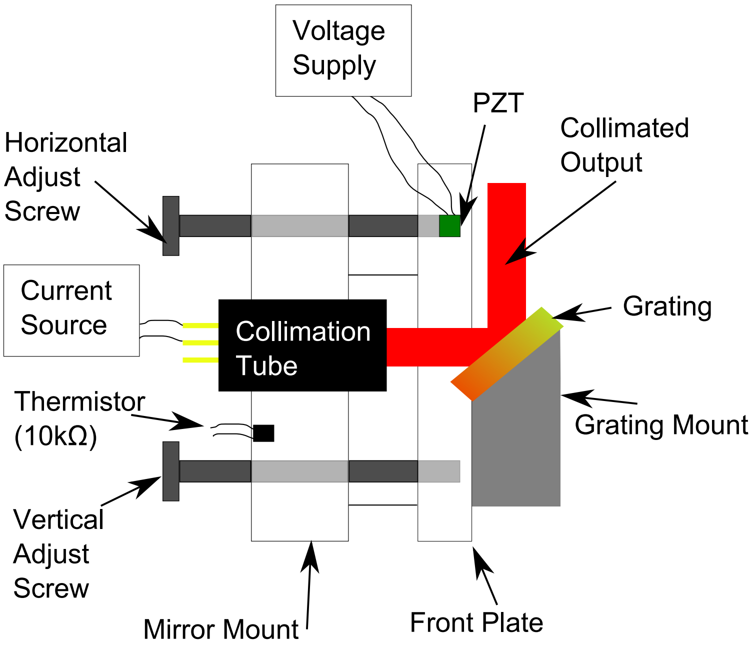

Figure 5.4: The external cavity diode laser used for the 672 nm laser source. Coarse frequency tuning is achieved using the horizontal adjustment screw, while fine control is achieved by varying the voltage applied to the PZT.

quency. A piezo actuator (Thorlabs AE0203D04F) fixed into the horizontal arm of the mirror mount allowed fine control over the grating angle, θ, and hence the frequency of the output. The maximum increase in the actuator length was 3 μm for an applied voltage of 100 V, which corresponds to a frequency range of $\sim$ 20 GHz. In practice, mode-hops limited the continuous tuning range using the piezo to around 2 GHz. To ensure mechanical stability, the assembled ECDL mirror mount was attached to base plate, which was used to fix the ECDL inside a die cast box. Anti-reflection coated windows were fixed into the boxes to allow the laser beams to exit the box.

As described previously, the temperature of the diode has a direct impact on the output frequency of the laser. Using a heat conducting glue, a Peltier element was fixed between the assembled mirror mount and the base plate. The Peltier element was connected to an automatic temperature controller (Wavelength Electronics FPT-5000), which was configured to deliver a maximum current of 3 A.

A 10 kΩ thermistor, set into the mirror mount between the collimation tube and baseplate provided the feedback to the FPT-5000 to allow it to maintain a constant temperature to within 0.01 °C of the desired set point.

Changes in injection current also affect the diode output wavelength. An increase in current corresponds to a decrease in the frequency of the light output by the laser. Typically, an increase of 1 mA of the injection current corresponds to a 4 GHz decrease in output frequency. As the atomic transitions of interest have linewidths of < 1 MHz, it is therefore critical that the current noise is minimised and kept below a peak-to-peak value of 1 μA. A Thorlabs LD1255R was used as the current driver for the laser diode. A 27 Ω resistor was connected in series with the laser diode to allow a direct measurement of the current flowing through the circuit and also of the current noise. As laser diodes are extremely sensitive to sudden changes in current [75], three 10 μF capacitor was placed in parallel with the diode to ensure a gradual decrease in current in the event of a sudden loss of power. Using a Fluke 87 series multi-meter, the current noise was measured to be less than 1 μA.

5.3.1 Alignment and wavelength calibration

As laser diodes have only a relatively limited lifetime, and are very sensitive to environmental conditions, replacing the diode in the ECDL was, unfortunately, a regular occurrence. The following section describes the alignment procedure used to bring the wavelength of a new laser diode close to the atomic transition wavelength and also correctly set the feedback of the ECDL.

The laser diode was fixed into the collimation tube and driven a few mA above threshold to provide a 1 mW output. The lens was then adjusted to ensure that the laser output was collimated over the length of the optical bench. The tube was inserted into the post holder, positioning the front of the lens ~ 10 mm away from the grating, and then rotated to align the long axis of the beam profile parallel with optical table and perpendicular to the lines on the grating. The drive current was then reduced until the diode was just below threshold. This is the point at which the diode is most sensitive to optical feedback. A sheet of white card was placed one meter from the ECDL and used for observing the output. By rotating the horizontal and vertical adjust screws of the mirror mount a weak beam becomes visible close to the main beam profile. This weak beam is the result of a poorly aligned cavity, so by using the mirror mount adjustments screws to collapse the weaker beam onto the principal beam the output power of the diode increased dramatically as this feedback takes the laser above threshold. A power meter was then used to monitor the output power of the laser. The following process is then iterated until optimum feedback conditions are met:

- reduce the drive current until the diode is just below threshold.
- small rotation of the lens.
- alter vertical and horizontal adjustments of mirror mount to observe if the laser can be made to lase.
- reduce current to just below threshold and repeat.

The above process should be repeated until the threshold current is minimised.

At room temperature the HL6545MG laser diode is designed to output light at a wavelength of 660 nm. To reach the desired wavelength of 672 nm it was necessary to heat the diode to temperatures above 60 °C, the precise temperature was specific to the laser diode used but was typically 64 ±1°C. The Peltier element was driven with ~ 2 A of current to raise the temperature of the entire mirror mount and therefore increase the case temperature of the diode. Fig. 5.5 shows the typical variation of the bare diode output wavelength as a function of temperature. When placed in the ECDL, the grating could be used to extend the upper limit of the wavelength by a further 10 nm, permitting a lower operating temperature and increasing the diode lifetime. Once the temperature of the mirror mount had stabilised, the diode was brought up to 70 % of the

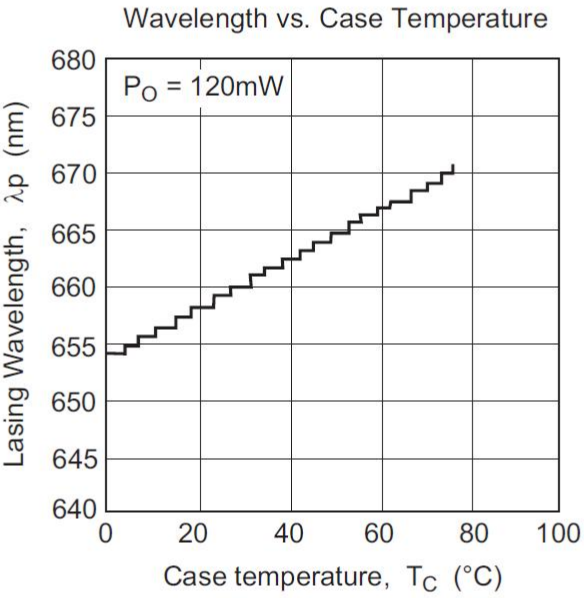

Figure 5.5: An example of the wavelength of light produced by a HL6545MG laser diode. Adapted from [144].

maximum operating current, producing output powers > 50 mW. The horizontal alignement screw was used to set the output wavelength close to 671.9 nm, the applied voltage to the piezo was then used for fine adjustment.

5.3.2 Stabilisation to a stable reference cavity

A number of attempts were made at producing an atomic frequency reference for the 672 nm laser with methods similar to that described in section 4.5, however, these were unsuccessful and alternative methods had to be sought. There are a number of absorption lines in the absorption spectrum of iodine that are close to the $4^1D_2 - 5^1P_1$ transition in calcium [145]. However, these absorption lines are weak and long interaction lengths and high iodine temperatures are required to provide a sufficient absorption signal [146]. The locking scheme which proved most successful in fixing the frequency of the 672 nm laser made use of a stabilised reference cavity [147].

Experimental setup

For the cavity to be a reliable frequency reference for the ECDL, it was necessary to first stabilise the cavity against environmental changes such as mechanical vibrations or thermal drifts, as these cause the frequency of the cavity modes to drift [147]. The linear Fabry Perot cavity used as the reference had a finesse of ~ 100 and a FSR of 300 MHz. The cavity length could be controlled, on the micron scale by changing the applied voltage to the PZT, which was attached to one of the cavity mirrors. This allowed the cavity length to be modulated at high frequencies. To fix the cavity length and make it a suitable frequency reference, the cavity was locked to a temperature stabilised HeNe laser, which acted as an absolute frequency reference. The HeNe output beam was directed into the cavity (M1), parallel, but off-centre from the cavities central axis, see Fig. 5.6. A photodiode was used to detect the light re-emerging from M1, which was produced by the resonances experienced by the cavity as the length was scanned by applying a large AC voltage (75 V_{p-p}, 20 Hz) to the PZT, shown in Fig. 5.7 (a).

In addition to the large AC scan, a weak modulation at 18 kHz was applied to the PZT, allowing a lock-in amplifier to demodulate the Lorentzian peaks and produce dispersion-like curves, see Fig. 5.7 (b). After alignment of the beam into the cavity, the large AC scan was removed and the output of an electronic integrator was connected to the PZT. The input to the integrator was the dispersion curve produced by the lock-in amplifier. At this point, the cavity could easily be locked to the HeNe laser by setting the PZT DC offset such that the cavity was close to a resonance and then switching the integrator to 'lock'. As the HeNe laser was extremely stable, the cavity would remain locked for weeks at a time, provided that there were no large mechanical disturbances on the optical table.

A beamsplitter was used to align a fraction (~ 3 mW) of the 672 nm ECDL output into the opposite end of the cavity to the end the HeNe was coupled into. Directed into the cavity, parallel but off centre from the central axis, the beam

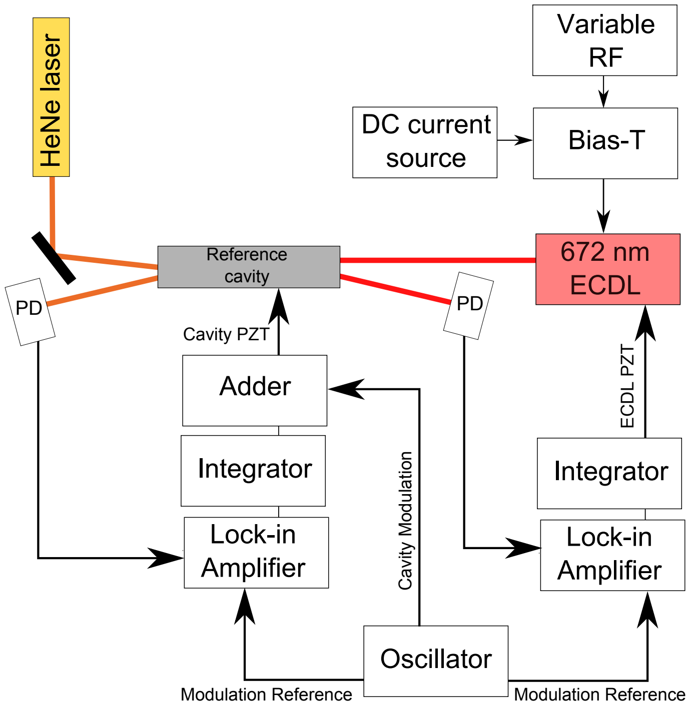

Figure 5.6: The 672 nm diode laser stabilisation system. The laser is locked to a reference cavity, which has been pre-stabilised to a HeNe laser.

circulated a number of times before it re-emerged and detected by a photodiode, see Fig. 5.6. To observe a resonance of the 672 nm light inside the cavity, the frequency of the laser had to be scanned by applying a varying voltage to the PZT within the ECDL, see Fig. 5.8 (a). As a result of the existing modulation of the reference cavity PZT, the 672 nm light detected by the photodiode could also be demodulated to produce a dispersion-like signal, Fig. 5.8 (b). Using an additional set of integrator electronics it is then possible to lock the laser to the cavity. However, as the reference cavity modes are fixed at a spacing of 300 MHz, there was little chance that locking the 672 nm laser to one of these modes would correspond to the frequency of the calcium $4^1D_2 - 5^1P_1$ transition. Therefore, a method to remain locked to the cavity but also frequency shift the laser was required.

An extremely useful property of diode lasers is the ease in which they can be frequency modulated. When used in spectroscopy experiments, ECDLs will

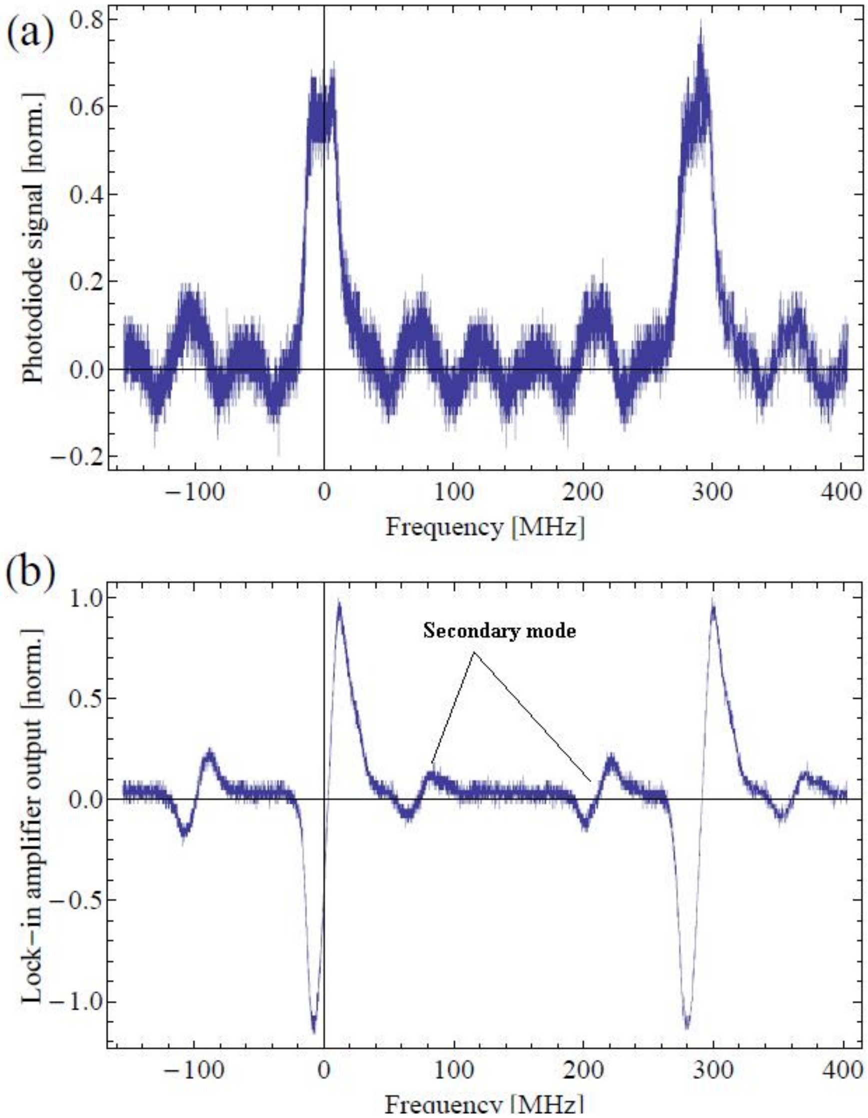

Figure 5.7: (a) The signal detected by the photodiode when the HeNe light is incident on the cavity and the cavity length is scanned by ∼300 MHz. (b) An 18 kHz modulation applied to one of the cavity mirrors allows the photodiode signal to be demodulated to produce a dispersion curve that is then used to stabilise the cavity length. A secondary HeNe laser mode can be observed in both the photodiode signal and its derivative, but is unused by the system.

often have the diode drive current modulated in the kHz range to allow lock-in amplifiers to produce dispersion-like representations of atomic transitions [75]. However, a more useful application in this instance involves modulation of the drive current at tens of MHz. In this regime, the optical spectrum develops sidebands located at the multiples of the RF modulation frequency, which is useful in a number of spectroscopic applications [148]. To generate sidebands on the 672 nm ECDL optical spectrum, the current delivered to the diode was sourced from a bias-t, which was used to couple together the output of the DC current driver and a variable radio-frequency synthesiser (Hameg HM8134-3, 0-1.2 GHz). The amplitude of the sidebands is proportional to the RF power delivered to the diode, typically the maximum power delivered was -1 dBm, powers greater than this drove the diode into a multimode operation.

The addition of sidebands to the 672 nm spectrum produced additional dispersion curves from lock-in amplifier 2, since there was already a modulation of 18 kHz on the reference cavity PZT. These dispersion curves were smaller in amplitude and had their zero crossings shifted from the carrier signal by a frequency equal to the RF output of the synthesiser. The advantage of using a variable RF synthesiser becomes apparent when the ECDL is locked using one of the dispersion curves produced by a sideband. Once locked on a sideband, the synthesiser output frequency could be adjusted between 10-140 MHz in real-time, providing a fully tunable source whilst remaining locked relative to the cavity resonance.

5.4 1530 nm laser

In addition to building a source of cold calcium, one of the main aims of this thesis was to explore methods of returning atoms populating the ${}^3P_2$ to the ground state. Previously, this has been done by driving atoms to the higher lying $4p^2\ {}^3P_2$ state, however, the short wavelength photons used in this process result in heating of the atoms [90]. Another, more obvious, route of returning the atoms to the singlet energy level scheme involves using the ${}^1D_1 - {}^3P_2$ transition; the source of the leak out of the cooling cycle. The wavelength required to stimulate this transition is 1530 nm [82], which is a wavelength at the edges of the S and C bands used in industrial fibre optic communication networks [149]. As a result of being close to

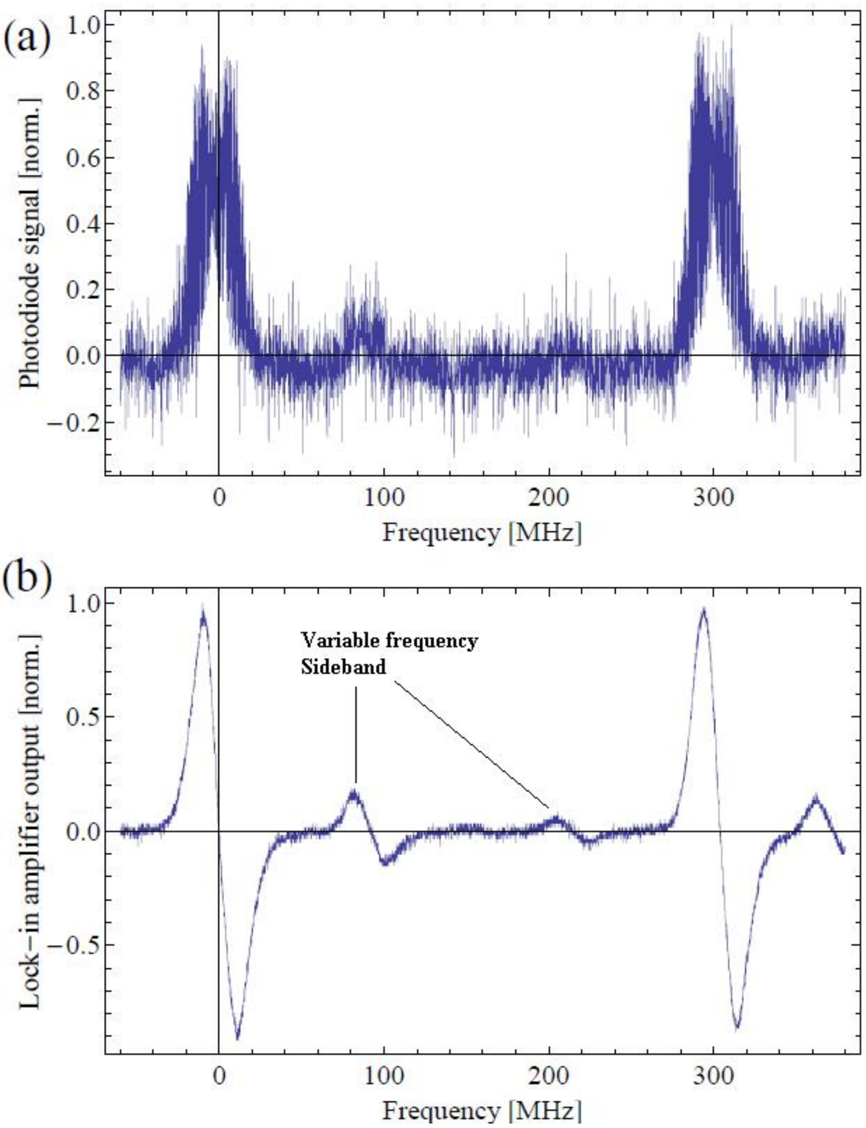

Figure 5.8: (a) The modes detected by the photodiode as the 672 nm laser is scanned using the grating. (b) Although the cavity is locked the cavity mirror is still modulated. As a result, signal (a) can be demodulated to produce a dispersion-like curve that can be used to lock the laser to the cavity. Position of the modulation sideband can be changed by simply altering the frequency of the synthesiser.

telecommunications wavelengths, it is possible to source commercial laser diodes that are capable of driving the atomic transition.

A QPhotonics (QDFBLD-1530-20) laser diode was chosen as the source for

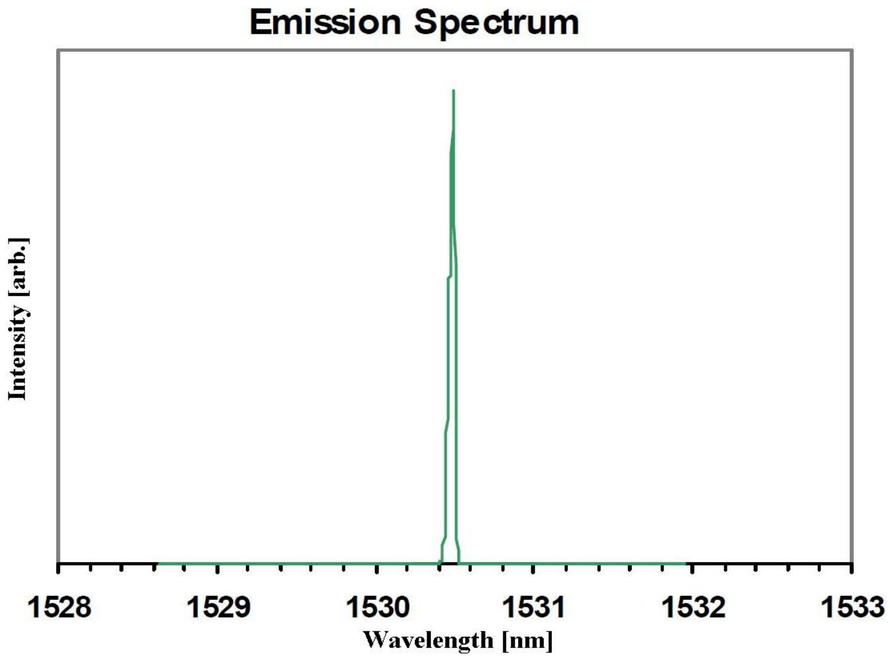

Figure 5.9: Emission spectrum of 1530 nm laser at 25 °C [150].

the 1530 nm light. The DFB-laser combines the diode, a TEC element and a 10 kΩ thermistor into a single compact unit. The diode package was fixed into a compatible mount (Thorlabs LM14S2) which was connected to a TEC controller (Wavelength Electronics MPT-5000) and a low noise current source (ILX Lightwave LDX-3200 Series). A maximum of 20 mW of 1530 nm light can be output by the laser, this is done via a single mode fibre, which collects the light directly output by the diode.

Laser diodes supplied in a butterfly package are generally not designed to be used in an ECDL type configuration, limiting the achievable linewidth to a value set by the manufacturer; approximately 1 GHz. With a lack of optical feedback, the diode temperature is the only means of controlling the output wavelength. The emission spectrum of the diode at 25 °C is shown in Fig. 5.9, the position of the centre peak varies by 0.2 nm per °C [150]. The ILX current driver was set to output 87.4 mA to the diode, which produced a usable output power of 14 mW.

Chapter 6

MOT setup and characterisation

Chapters 4 & 5 describe how to build the narrow linewidth light sources that are required to produce a calcium MOT. Chapter 3 describes the construction of a UHV chamber inside which a calcium MOT can be formed. With previous chapters as a reference, the following pages describe the the experimental setup and operation of what is believed to be the first alkali-earth MOT in the UK.

The setup differs significantly from the standard vapour cell MOTs commonly employed in modern cold atom experiments. The setup's uniqueness demands that many of the experimental operating parameters must be optimised individually to achieve the maximum number of trapped atoms. The results of this optimisation are discussed alongside the setup description.

6.1 Experimental setup and apparatus

6.1.1 Optical layout

The experiment is built upon two floating optical tables (see Fig. 6.1). Each of which has over-head shelving to support the electronic equipment used for experimental control and sensing. To isolate the vibrations of the UHV system, which are due to the system being constantly pumped by a turbomolecular pump, one table is dedicated to lasers, while the other is for the UHV system and coupling optics.

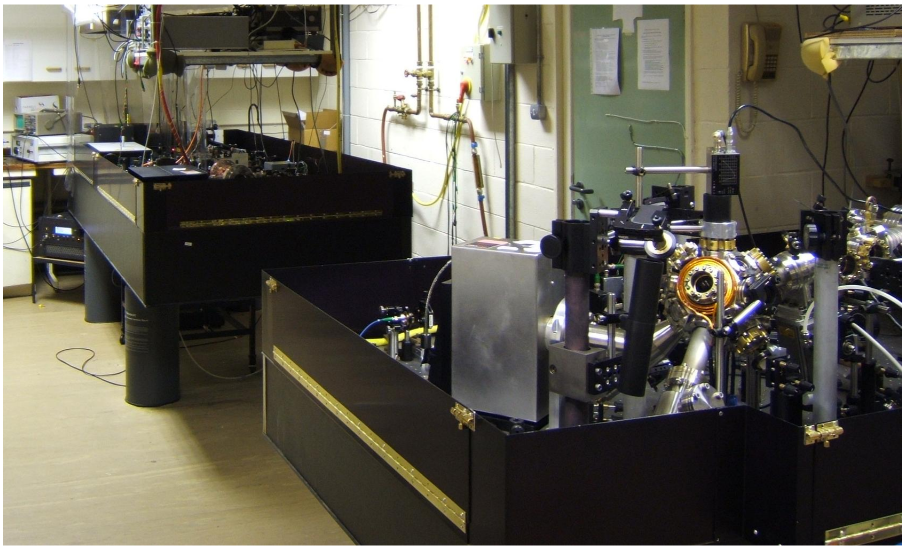

Figure 6.1: An image inside the lab showing the positioning of the laser (left) and vacuum (right) optical tables.

The *lasers table* has mounted on it the Verdi, the Ti:sapphire laser, the 672 nm diode laser, the HeNe and the 657 nm diode lasers. Light from these lasers that is needed to perform experiments on the *vacuum table*, is coupled across using polarisation maintaining fibres. The light emerging from the fibres on the vacuum table is then prepared and coupled into the chamber, as shown in Fig. 6.2.

Originally, the frequency doubling cavity was intended to be built on the lasers table, and blue light would also be coupled to the vacuum table via an optical fibre. This was to ensure that mechanical noise generated on this table would not affect the stability of the resonant enhancement cavity. However, difficulty arose in sourcing a fibre that did not heavily attenuate light in the blue part of the spectrum. This resulted in a different approach being taken. Fibres designed for IR wavelengths are a well developed technology and can transport light at these wavelengths over large distances (> 10 m) with negligible loss of optical power. It was decided that instead of transporting blue light between tables, the Ti:sapphire output would be sent via fibre to the vacuum table where it would

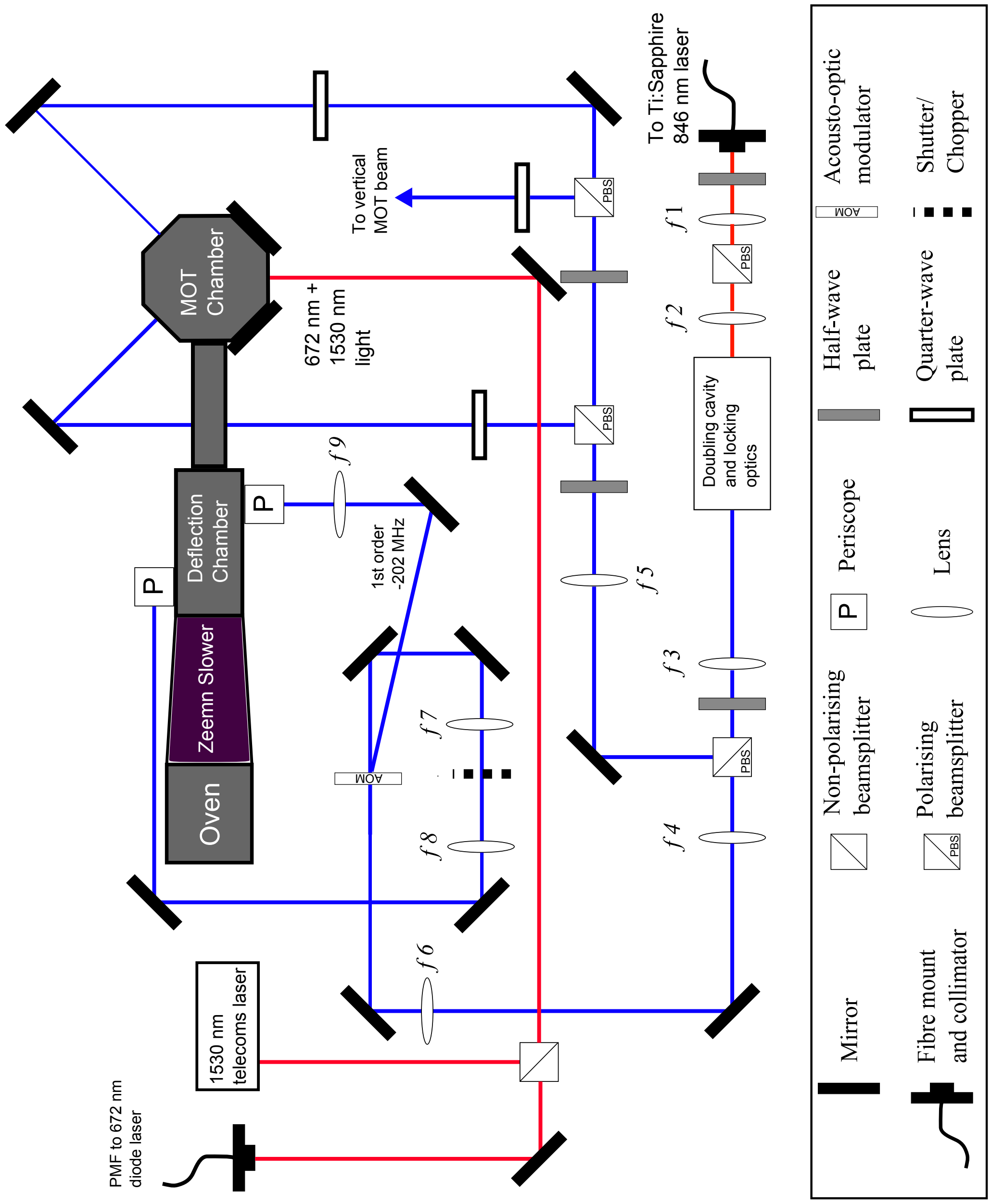

Figure 6.2: A schematic of the optical setup used to slow the atomic beam and create the MOT. Note that it is sufficient for the repumping lasers to be incident on the MOT from only one direction. Each of the three blue MOT beams are retroreflected.

then be coupled into the doubling cavity. Fortunately, after setting up doubling cavity on the vacuum table, the vibrations caused by the pump did not affect the output of the doubling cavity at all, thus allowing the output of the cavity to be used in the experiment without any compromise on 423 nm power. The half-wave plate and polarising beamsplitter placed at the output of the Ti:sapphire fibre was used to ensure that the light coupled into the doubling cavity was of pure vertical polarisation.

The optical layout shown in Fig. 6.2 is typical of the configuration used when atoms are trapped by the apparatus. The output power from the doubling cavity was divided up as follows; 35 mW of light for the MOT beams, 24 mW was used in the Zeeman slower and 10 mW was used for the (recirculating) deflection stage. This splitting of power was achieved by placing an AR-coated half-waveplate before a polarising beam splitting cube, and then rotating the waveplate about the beam axis through. The power output from each port of the beam splitter can then be divided in any ratio required by the controlling the angle of the waveplate.

Light that emerges from the doubling cavity is not collimated, therefore three lenses ($f3$ = 100 mm, $f4$ = 100 mm and $f5$ = 100 mm) were used to produce collimated laser beams with a diameter of 12 mm. The lens $f6$ = 400 mm focuses the incident. Light into an AOM from which 75 % of the light emerges in the first order, shifted in frequency by 202 MHz. Lens $f9$ = 500 mm then gently focuses this light through the Zeeman slower onto the front face of the calcium oven, to a spot of $\sim$ 5 mm. The zeroth order beam from the AOM is collimated to a beam size of 14 mm and is used for the 2D molasses deflection stage. A shutter placed in this beam acts as a switch for deflecting atoms into the main chamber, allowing control over loading of the MOT.

The paths of the repumping lasers are also shown in Fig. 6.2, for more details on the setup of these lasers and their effect on the MOT, see chapter 7.

6.1.2 Detectors

Photo detectors are positioned throughout the calcium experiment and used as a tool for accurately measuring the amount of light incident on an area of interest. Specifically, within the experiment they are used for: measuring the powers emitted by the various lasers used in the experiment, determining the fluorescence from atoms emitting photons, triggering parts of the apparatus and detecting the absorption of a laser beam passing through a group of atoms.

The experiments carried out in this thesis required a number of different colours of light to be detected and as no one material has a suitable spectral response for all of these colours detectors constructed from a number of different materials were used. Table 6.1 lists the detectors used in the experiment and the range of wavelengths which they are sensitive to.

Detector	Spectral response [nm]
Silicon Photodiode for Visible (BPW 21)	350-820
Hamamatsu PMT (H5784-20)	300-900
Silicon (bpx 65)	400-1050

Table 6.1: The spectral response for the main photodetectors used in the calcium experiment.

Light scattered by atoms trapped in the MOT and light from the atomic beam is detected using the amplified output of a BPW 21 diode. The bulk of the initial characterisation of the MOT, and the measurements of the velocity distributions produced by the Zeeman slower, were measured using this photodiode. However, the noise produced by this photodetector meant it was not sensitive enough for the experiments using the 1530 nm laser and had to be replaced with a commercial silicon detector package (LCA-S-400K-SI) with integrated low noise circuity.

A CCD camera was also implemented to monitor the density distribution of atoms trapped in the MOT. The camera was positioned at an unused port on the MOT chamber and included a zoom lens system. This allowed the camera to output a magnified image of the MOT onto a TV monitor. Using the magnified image on the screen as a reference, the MOT beams were slightly re-aligned to produce a compact MOT with a profile as close to a Gaussian curve as possible.

One of the transitions of interest within the ^{40}Ca energy level scheme is the $^1S_0 -^3 P_1$ transition. This transition is so long lived that few photons are emitted at this wavelength. As the amount of 657 nm light scattered by trapped atoms is negligible when compared with that at 423 nm, a much more sensitive method of detection is required than the amplified photodiode previously used.

6.1.3 Acousto-optic modulators

Lasers that are used within cold atom experiments are normally frequency stabilised to a reference cavity or to a known atomic line. These reference frequencies are often tens of MHz away from the frequency that is required for laser cooling. The acousto-optic modulator (AOM) is a device that gives the ability to shift the frequency of a laser beam by a controlled amount. A detailed description on the principles and applications of AOMs is given in [151].

One Crystal Technology 3080-125 AOM was used within the saturated absorption spectrometer used in the 423 nm laser stabilisation setup. This AOM was driven with an Isle Optics RF oscillator at 80 MHz, well within the 50 MHz bandwidth of the AOM. Using two mirrors and a focusing lens, up to 75 % of the incident light could be coupled into the first diffracted order.

The Zeeman slower beam was derived from the -1 diffracted order from the laser beam passing through a 3200-120 AOM, driven by a Marconi Instruments 2022 RF signal generator, whose output was amplified by a Wessex Electronics +34 dB amplifier. Lenses were used to focus the laser light to a spot size of 300 μm at the centre of the crystal within the AOM. With careful alignment and one Watt of RF power at 202 MHz delivered to the AOM, over of 80% of the incident light could be coupled into the first order and used in the Zeeman slower.

The remaining light was collimated and used for the deflecting the slow atoms emerging from the slower into the MOT chamber.

6.1.4 Zeeman slower

The Zeeman slower laser beam was derived from a laser source which has been stabilised to an atomic reference using the method described in 4.5. Therefore, the light incident on the AOM was detuned from resonance by 24 MHz resulting in an overall Zeeman laser beam detuning of -226 MHz. To drive the atoms which experience the Zeeman magnetic field, the laser light must be σ^+ polarised to drive the $m_J = +1$ level of the excited state. This was achieved by placing a quarter waveplate into the Zeeman beam with the optic axis aligned at 45° to the laser polarisation. Light is coupled through one of the lower windows on the deflection chamber and directed to the front face of the oven using a silver mirror fixed inside the chamber.

The Zeeman slower technique was used to slow the longitudinal velocity of an atomic beam. However, as the beam is slowed there is an accompanying increase in the transverse velocity that arises due to the spontaneous re-emission of the absorbed photons from the Zeeman laser. As the atoms decrease in longitudinal velocity from v_i to their final velocity v_f, given by

$$v_f = v_i - v_{rec}N(t), \tag{6.1}$$

the transverse velocity components increase as the atoms scatter photons via [152]

$$(v_{x,y}^{\mathrm{rms}})^2 = \frac{v_{\mathrm{rec}^2}}{3}N(t), \tag{6.2}$$

where v_{rec} is the recoil velocity and $N(t)$ is the number of photons scattered between $t = 0$ and t.

For atoms slowed from $v_i = 650$ m/s down to $v_f = 55$ m/s, over a distance of 20 cm, this results in an increase in the average transverse velocity of 2 m/s. Once atoms leave the Zeeman slower at the longitudinal velocity v_f, they will have a transverse velocity component of v_{trans} and the atomic beam will spread with a constant divergence angle of $2v_{trans}/v_f$.

When atoms leave the oven they emerge into an opening angle of 11°, resulting in an initial rms transverse velocity of 67 m/s. After leaving the oven these atoms almost immediately collide with the vacuum chamber walls and do not exit from the Zeeman slower. Only atoms with an initial transverse velocity less than 12 m/s will reach the end of the Zeeman slower. As shown above, the Zeeman slower also adds a small contribution to this transverse velocity, ensuring that a number of the slow atoms would not be able to reach the MOT chamber. This heating effect can be reduced with the use of a 2D molasses situated at the exit of the Zeeman slower.

6.1.5 Cooling and deflection

Cooling

Light from the zeroth order of the Zeeman slower AOM was used to create a Doppler cooling stage to reduce the velocities of the atoms in the transverse directions. One laser beam was used to create a 2D optical molasses using the geometry shown in Fig. 3.4. Atoms moving in molasses decay to the Doppler temperature in a characteristic time constant α/m, where

$$\alpha = -4\hbar k^2 \frac{I}{I_{sat}} \frac{2\Delta/\Gamma}{[4\Delta^2/\Gamma^2 + (1 + 2I/I_{sat})]^2}, \tag{6.3}$$

is the friction coefficient and m is the atomic mass [24].

A ^{40}Ca atom in a laser beam with an intensity of 7 mW/cm^2, detuned 24 MHz from the atomic resonance, will decay to the Doppler temperature with a time constant of around 50 μs. As the atoms that pass through the cooling stage with a speed of around 60 m/s, the beam diameter had to be sufficiently large enough to provide cooling for a number of time constants. The beam diameter was made to be 1.2 cm. This meant any atoms passing through the molasses would spend over 4 time constants in the molasses, ensuring that the atoms were cooled to the

Doppler temperature before exiting the deflection region.

Deflection

Simply cooling in the vertical direction does not remove the cooled atoms from the Zeeman slowed beam. By setting up the vertical molasses beam as shown in Fig. 6.3, the vertical velocity of the incoming atoms could be manipulated to direct the atomic beam into the vacuum chamber. Atoms that enter the molasses along the z-axis have their v_z component slowed by $v_z\text{cos}(\theta)$ and the v_y component of their velocity increased to $-vz\text{sin}(\theta)$, deflecting the atoms out of the MOT chamber. The angle of the deflection beam relative to the vertical axis was chosen to be $\theta = 13°$, this ensured sufficient deflection of the cooled atoms from the beam. As the beam is not along the y-axis, the atoms will experience the light Doppler shifted closer to resonance. For an angle of $\theta = 13°$, atoms traveling at 60 m/s experience the light Doppler shifted to 8 MHz above the atomic resonance. This results in a large friction coefficient slowing the atoms very quickly, deflecting the atoms out of the beam.

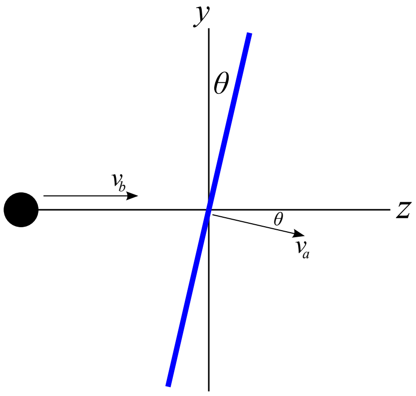

Figure 6.3: The setup for the vertical beam in the 2D molasses. Atoms entering along the z-axis are deflected by an angle θ. The experimental setup used an angle of $\theta = 13°$ to drive the atoms with a resonant beam and ensure efficient cooling.

6.1.6 MOT coils

As discussed previously, the scattering force requires a magnetic field to be able to trap atoms spatially. Experimentally, this was achieved using two coils of wire arranged in an anti-Helmholtz type configuration, which produced a linear magnetic field, passing through zero at the trap centre. A single piece of copper wire was shaped to produce two coils, each with 12 turns, along a common axis and separated by 132 mm. The inside diameter of the coils was 35 mm, large enough to allow the coil to be slotted over the viewports and fixed to the outside of the MOT chamber.

The coils were constructed from wire with a hollow square cross section and turned using the lathe in the Photonics group workshop. Water from the labs main supply was passed through the bore of the wire to provide cooling for the wire as the large currents passing through generated large amounts of heat. The current flowing in the coils could be varied between 0-200 A using a current control circuit. Typically, the maximum atom number was obtained when 180 A was flowing through the coils.

The MOT coils have a radius $R = 5$ cm, are separated by $a = 10$ cm and produce a total field between them that varies along the coil axis as,

$$B_{\text{tot}} = \frac{\mu_0 n I R^2}{2}\left(\frac{1}{(R^2+(z-a/2)^2)^{3/2}} - \frac{1}{(R^2+(z+a/2)^2)^{3/2}}\right), \tag{6.4}$$

where $n = 12$ is the number of turns each coil has and μ_0 is the permeability of free space. The field gradient at the centre close to the centre of the trap is almost constant at $\frac{dB}{dz} \approx 17.89$ G/cm. It should be noted that the trap field is not isotropic as the divergence of the magnetic field is zero. This means that the field gradient along the axial direction is actually twice of that in the x and y directions.

The MOT coils were only ever switched off during the experiment when an observational check for the presence of the MOT was required. Therefore, the 500 μs that the coils required to fully switch off was never a limiting factor.

6.2 Atomic beam characterisation

6.2.1 Beam presence

The most important part of the vacuum system is the atomic oven and its ability to output a beam of neutral calcium atoms. Once the vacuum system, as described in chapter 3, had first been assembled and brought to a pressure of 10^{-8} mbar, the temperature of the oven was slowly risen from room temperature to 450 °C. The initial heating of the oven was done slowly to allow any unwanted particles inside the chamber to evaporate freely and not react with and spoil the calcium. The oven was held at this temperature for a further hour to ensure that all of the calcium had been heated uniformly to produce a constant atomic beam. Note that the first version of the deflection chamber did not use internal mirrors to recirculate the molasses beam. It had viewports on every side, allowing optical access to the atomic beam for the following experiments in this section.

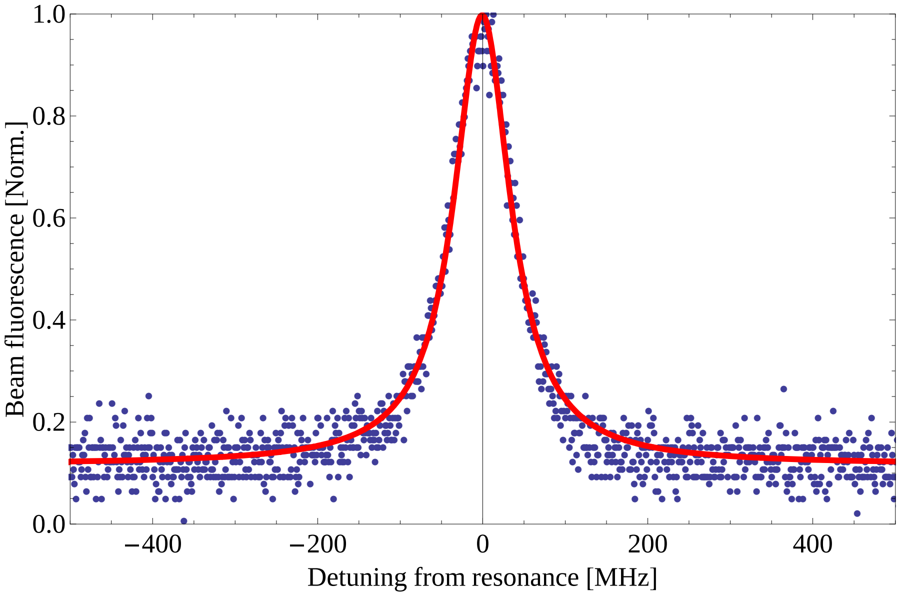

Figure 6.4: The fluorescence from the atomic beam as an orthogonal laser beam scans its frequency over the ${}^1S_0 -{}^1 P_1$ transition.

Once the oven was running and the vacuum had settled to a constant value, an experiment was performed to check for the presence of an atomic beam inside the deflection chamber. This was achieved by exciting the atoms with a resonant 423 nm beam that crossed the atomic beam at right angles, a photodetector detected the photons emitted orthogonally to both the laser and atomic beam directions. A sample of the beam fluorescence as the laser frequency is scanned across the atomic resonance is given in Fig. 6.4.

6.2.2 Velocity distribution from oven

After confirming that atoms were emerging from the oven, the longitudinal velocity distribution of the beam was measured with a similar setup. The photodetector remained in the same location and detected photons emitted vertically upwards by atoms. However, the laser beam was realigned such that it and the atomic beam were counter-propagating. The laser was scanned over a larger frequency range (6GHz) than in the previous experiment (600 MHz), in order to excite the atoms with many velocities from the distribution that were detectable in this configuration. Fig. 6.5 shows the signal detected by the photodiode for a probe beam power of 15 mW. The data are fitted with a Maxwell-Boltzmann distribution (Eqn. 3.1) for $T = 441$ °C. This temperature agrees well with the 457 °C measured by the thermocouples fixed to the oven inside the vacuum chamber.

6.2.3 Velocity distribution into MOT chamber

The experimental setup was designed to create a velocity distribution with an increased number of atoms at around 50 m/s and direct these atoms into the MOT chamber for trapping. A time-of-flight experiment was performed to ensure that the atoms arriving into the MOT chamber did have a velocity close to this value.

The 2-D molasses beams in the deflection stage of the experiment were derived from a 20 mW light beam, which was detuned 24 MHz from the atomic

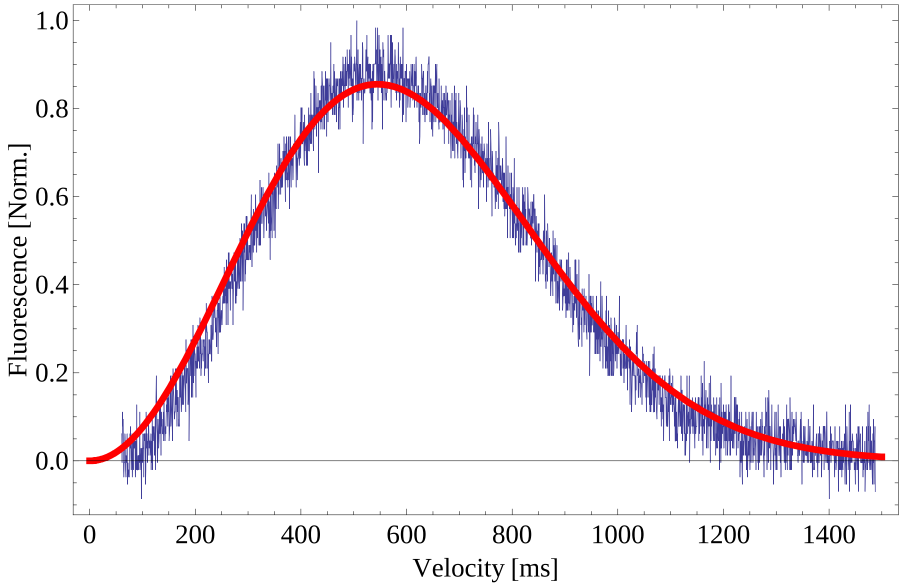

Figure 6.5: The longitudinal velocity distribution of the atomic beam produced directly from the oven. This plot was produced by monitoring the fluorescence from the atomic beam as the frequency of a counterpropagating laser beam was increased. From the fit a temperature of 441 °C is calculated. This is in agreement with the measured oven temperature of 457 °C.

resonance. Using a shutter the laser beam could be used to control the number of atoms reaching the MOT chamber. A 20 mW probe beam, detuned 24 MHz from the atomic resonance was used to illuminate the atoms arriving into the MOT chamber from the deflection stage. The probe was aimed transverse to the direction of the incoming atoms, while the fluorescence emitted orthogonally from excited atoms was measured with an amplified photodetector.

The resulting velocity distribution detected by the photodiode is shown in Fig. 6.6. This is the typical spread of velocities deflected into the MOT chamber for typical experimental operating parameters. The oven was set to 457 °C to produce atoms with an initial velocity distribution as shown above. The Zeeman slower had 9 A of current driven through its main coil and used a laser beam with 24 mW of power and was detuned from the atomic transition by 226 MHz with the use of an AOM.

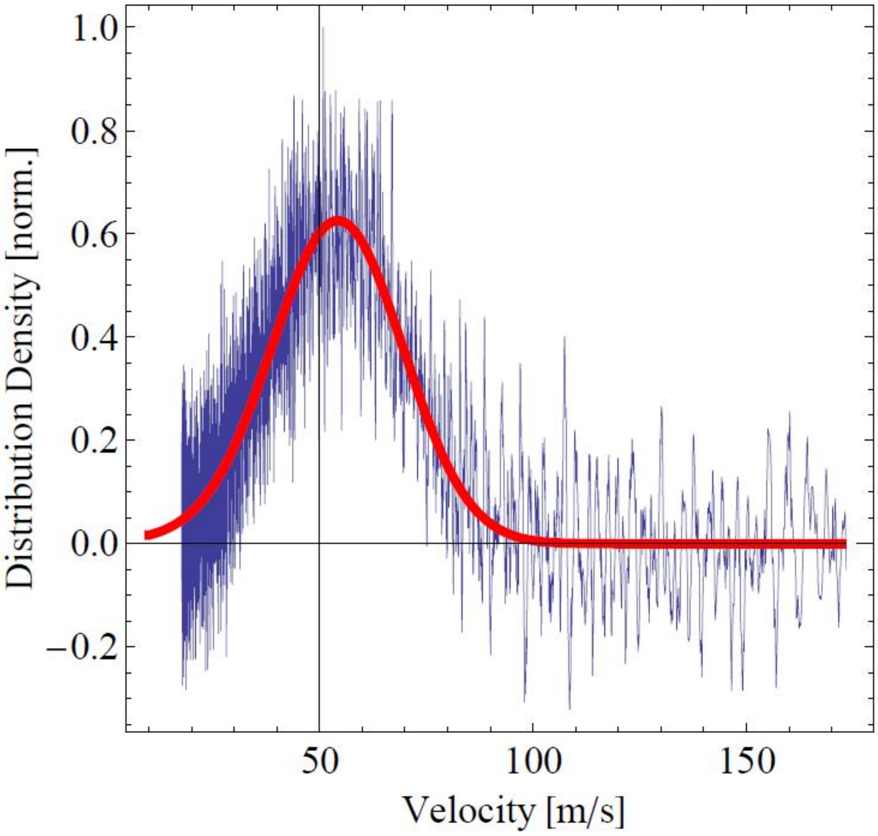

Figure 6.6: The velocity distribution of the atomic beam entering the MOT chamber for an initial oven temperature of 457 °C. A Gaussian fit measures a centre velocity of 55 m/s with a spread of 10 m/s.

For this experiment the shutter which the molasses beams pass through, was connected to a pulse generator which closed the shutter for 1.5 seconds and opened it for 1 ms. This ensured that for each experimental run there were no atoms remaining from the previous shot. The shutter open time was chosen to be short enough to allow the approximation that the fluorescence signal was proportional to the velocity distribution, but long enough to produce a detectable signal. Knowing that the distance between the deflection stage and the probe beam in the MOT chamber was $d = 33$ cm, the time axis of the measurement was converted to velocity via $v = t/d$, where t is the time between the detected signal and the opening of the shutter. The data in Fig. 6.6 is fitted with a $1/v$ weighted

Guassian centred on 55 m/s with a spread of 15 m/s.

6.3 MOT characterisation

The light for the MOT beams is split into three separate beams, each of approximately 10 mW, by using two polarising beamsplitter cubes. These beams are then passed through quarter-waveplates to produce circularly polarised light and then sent into the MOT chamber. The quarter waveplates were orientated such that the handedness of the radial beams was opposite to that of the axial beam, relative to the axis of the anti-Helmholtz coils. A photo of the MOT containing over 400,000 atoms is shown in Fig. 6.7.

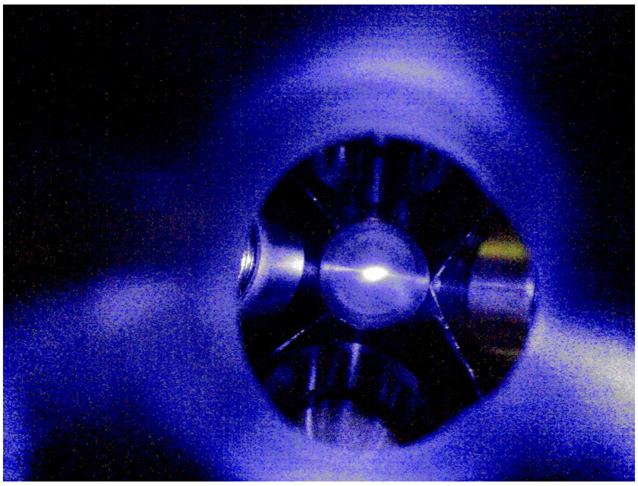

Figure 6.7: An image taken with a standard digital camera, showing the MOT working under typical conditions. The white cloud in the middle of the photo shows the fluorescence from over 400,000 atoms.

6.3.1 Atom number

A useful parameter for optimising a MOT is the number of atoms which it traps, this can be easily determined from the MOT fluorescence. A calibrated amplified photodiode was used to measure the light that was emitted by the MOT. At a distance $R = 87$ mm from the MOT, a lens with a radius $r = 12.5$ mm collects the emerging light and focuses it down onto the detector. At this distance, the collected light can be assumed to be coming from a point source that emits isotropically. The solid angle of the incoming light is determined by the lens as it has a smaller diameter than the viewport, therefore, $\Omega \approx 4\pi(r^2/4R)$. The rate at which atoms scatter the incident light is given by $R = \frac{\Gamma(I/I_{\text{sat}})}{2(1+I/I_{\text{sat}}+(2\delta/\Gamma)^2)}$ [71]. Since the energy of an emitted photon is $E = hc/\lambda$, the total number of atoms is found via:

$$N = \frac{2\lambda\Gamma}{hc}\frac{1 + I/I_{\text{sat}} + (2\delta/\Gamma)^2}{I/I_{\text{sat}}}\frac{4\pi}{\Omega}\frac{v_{\text{meas}}}{c_{dtr}}, \tag{6.5}$$

where v_{meas} is the voltage produced by the amplified photodiode and $c_{dtr} = 1.46 \times 10^7$ V/W is the calibration factor for the detector, which was found empirically. With an oven temperature of $T = 470$°C, 24 mW of laser power in the slower beam and the typical experimental operating conditions of $\delta = -24$ MHz, $\Gamma = 34$ MHz, $I = 77$ mW, using the amplified photodiode, the number of trapped atoms in the ground state is $N = 4 \times 10^5$ atoms. As the power from the doubling cavity contributed to a large error in the measurement of the intensity, the number of atoms is correct to the 15% level.

6.3.2 Deflection stage optimisation

To determine the power required for each of the molasses beams in the deflection stage of the apparatus, the MOT fluorescence was monitored as a function of the power in each of the beams. The following parameters were used to generate a MOT with around one hundred thousand atoms; the oven temperature was 497 °C a Zeeman slower laser detuning and power of - 230 MHz and 22 mW respectively and the Zeeman coil was driven with 9 A of current. The MOT used three retro-reflected, 10 mW, laser beams, resulting in an incident intensity of 1.3 I_{sat}. The MOT and deflection beams are both derived from the same source and are detuned 28 MHz from the atomic resonance.

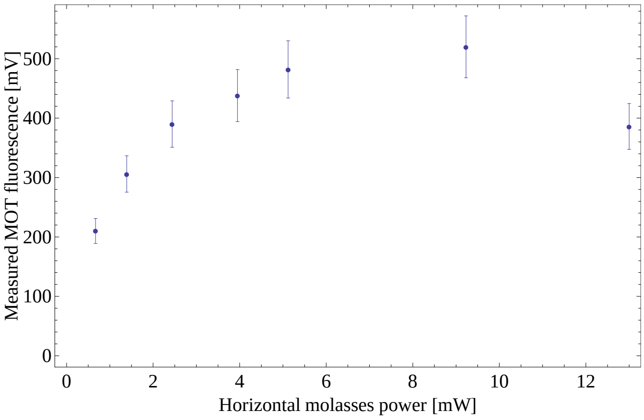

Figure 6.8: The effect on the MOT fluorescence as the horizontal molasses beam power is altered. An optimum value of 10 mW is found for the beam power.

Horizontal cooling

The horizontal beam of the transverse cooling stage reduces the velocity of the atoms in the horizontal plane and forces the atoms to stay on a course for the centre of the MOT chamber. The molasses in this direction is created by a laser beam with a diameter of ~ 1 cm, that enters through a viewport on the deflection chamber, crosses the atomic beam at 90°, exits the chamber via a viewport and is retro reflected by a mirror on the opposite side of the deflection chamber. The power into this beam was controlled with the aid of a polarising beam splitting cube and a half-wave plate. The MOT fluorescence was then measured as a function of the power in this beam with a constant 3.8 mW of power in the vertical molasses beam. It is clear from Fig. 6.8 that the maximum number of atoms are deflected into the MOT trapping region when the power in the horizontal beam is $\sim$10 mW.

Vertical cooling

The vertical cooling stage provides the means to deflect the slow atoms in the atomic beam to the MOT chamber. The following experiment was used to determine the optimum laser power that should be directed into the vertical molasses

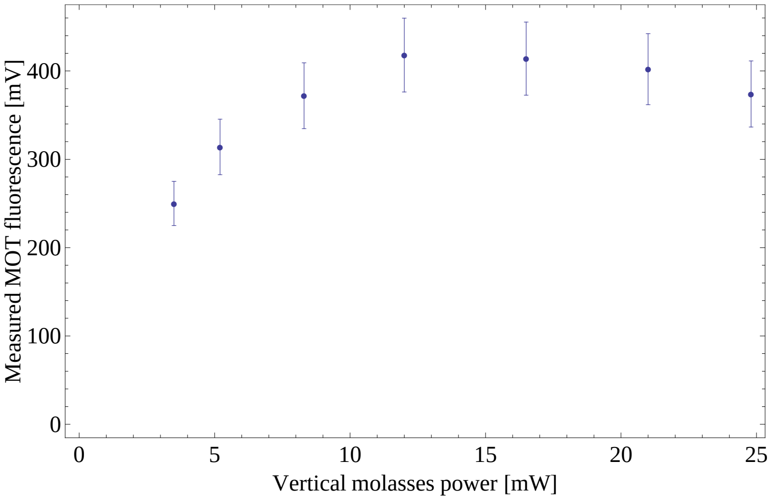

Figure 6.9: The effect on the MOT fluorescence as the vertical molasses beam power is changed. A value of around 11 mW generates the largest number of trapped atoms.

and deflect the maximum number of atoms into the MOT chamber. The setup for this experiment used a number of the same parameters as the previous experiment. However, as the power required by the MOT beams had to remain constant (30 mW), as did the Zeeman slower beam, the power for the deflection stage was limited to 25 mW. The horizontal molasses beam had a power of 3 mW, this was not the optimum value as found in section 6.3.2, but provided sufficient horizontal cooling to allow the rest of the power to be used in the deflection stage.

It can be seen from Fig. 6.9 that the number of trapped atoms is a maximum for around 11 mW in the deflection laser beam. As the power in the beam is increased beyond this power, the MOT fluorescence decreases. As the intensity of light in the molasses beam is increased the minimum temperature that can be imposed by the molasses also increases, resulting in a velocity that is faster than the capture velocity of the MOT.

6.3.3 Zeeman slower optimisation

To optimise the number of atoms trapped by the MOT, each of the Zeeman slower operating parameters were characterised with reference to the MOT fluorescence signal. In the following experiments the Zeeman laser detuning was kept constant at $\delta = -230$ MHz and the oven was operated at 457 °C. Both the horizontal and vertical molasses beams each had a power of 10 mW and were detuned by 28 MHz from the atomic resonance. Each of the MOT beams contained 10 mW of power, giving a total $I/I_{\text{sat}} = 1.3$ of incident intensity on the MOT and the current passing through the MOT coils was fixed at 180 A.

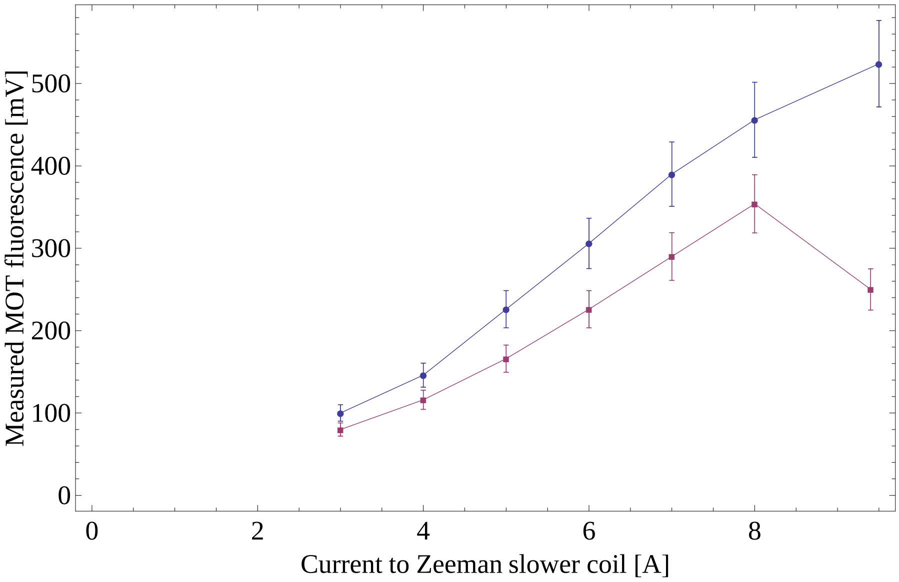

Figure 6.10: The MOT fluorescence as a function of the current flowing in the Zeeman slower. The blue dots represent a Zeeman slower laser beam power of 28 mW while the maroon squares represent a laser power of 17 mW.

The first experiment involved measuring the MOT fluorescence as a function of the main Zeeman coil current, which was carried out at two Zeeman laser powers 25 mW and 17 mW. It can be seen from Fig. 6.10 that the number of atoms trapped by the MOT was maximum for 9 A of current in the main Zeeman slower coil, this agrees well with the model on which the Zeeman slower was based.

The second parameter of the Zeeman slower to be characterised was the input laser beam power, this was varied as the MOT fluorescence was monitored. The current in main coil for this experiment was held at 9 A and the power in the Zeeman beam was varied with the aid of a polarising beam splitter cube. It can be seen from Fig. 6.11 that for 9 A of current in the main coil the slower the power which generates the largest trapped atom number is around 22 mW.

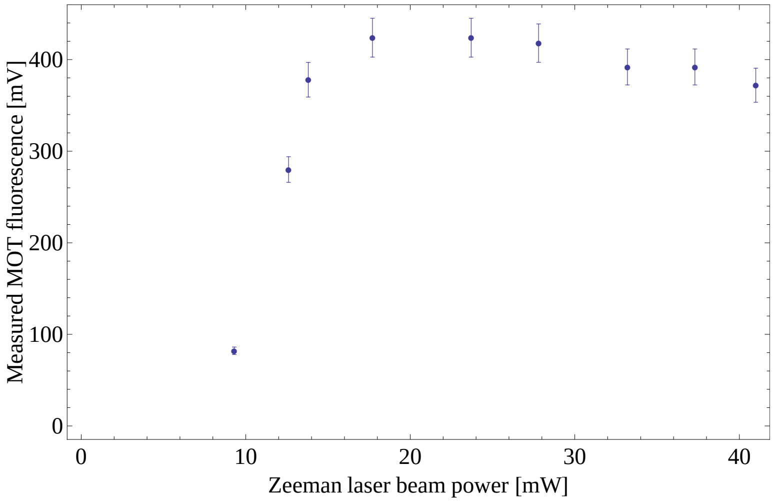

Figure 6.11: The MOT fluorescence as a function of the Zeeman slower laser beam power.

It should be noted that the Zeeman slower was originally designed to operate with two coils, the main coil and a termination coil at the end of the slower. When this coil was characterised it was observed that the current flowing in this coil made an insignificant impact on the trapped number of atoms in the MOT.

6.3.4 MOT coil current variation

Once the optimum loading values for the deflection stage had been set, the magnetic field of the trap was varied to observe the effect on the MOT fluorescence, this can be observed in Fig. 6.12. A current of ∼180 A flowing through the MOT coils produces the maximum number of trapped atoms. The maximum current that the supply could drive was 210 A. This placed an upper limit on the current available for the experiment.

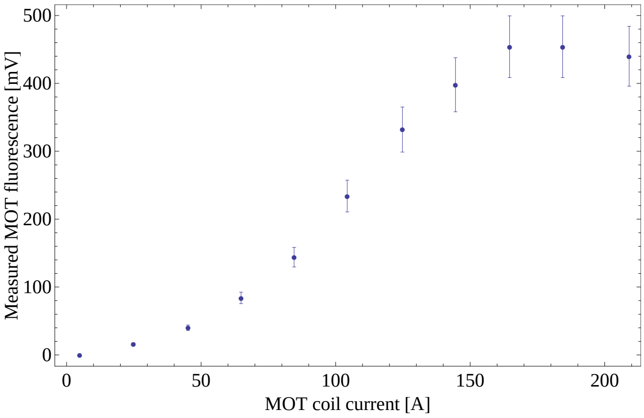

Figure 6.12: The MOT fluorescence as a function of the current flowing in the MOT coils for $I/I_{\text{sat}} = 1.3$, MOT beam $\Delta = -24$ MHz, Zeeman detuning of 230 MHz and an oven temperature of 456 °C.

6.4 Trapped atom characterisation

6.4.1 Trap lifetime

In any laser cooling experiment it is important to characterise the lifetime of the of the trap. This ensures that the atoms are not continually colliding with background particles and there are no unexpected losses. For the common vapour-loaded alkali MOTs the lifetime of the trap only depends on the background density and temperature [153].

The lifetime of atoms, trapped in the 423 nm MOT, is limited by leaks into the metastable triplet states. The rate of atoms lost from the MOT to the metastable $^3P_2$ state depends on the scattering rate on the cooling transition. Therefore, from the scattering rate, R, it is clear that the lifetime of the trap depends on the intensity of light in the MOT beams. The power into each of the three retro-reflected, 1.2 cm, MOT beams was varied to find a large MOT fluorescence signal but also provide a reasonable lifetime.

A chopper was used to pulse the 2-D molasses beam on and off for periods of ∼400 ms, allowing the trap to fully load and empty when the beam was on and off respectively. The MOT/2-D molasses beams were detuned by 24 MHz from the atomic resonance, while the MOT fluorescence was continually monitored with the amplified photodiode. The lifetime of the trap was measured for a number of MOT beam intensities. Each of the values are shown as points in Fig. 6.13, while the lines represent the calculated lifetime from a rate equation model.

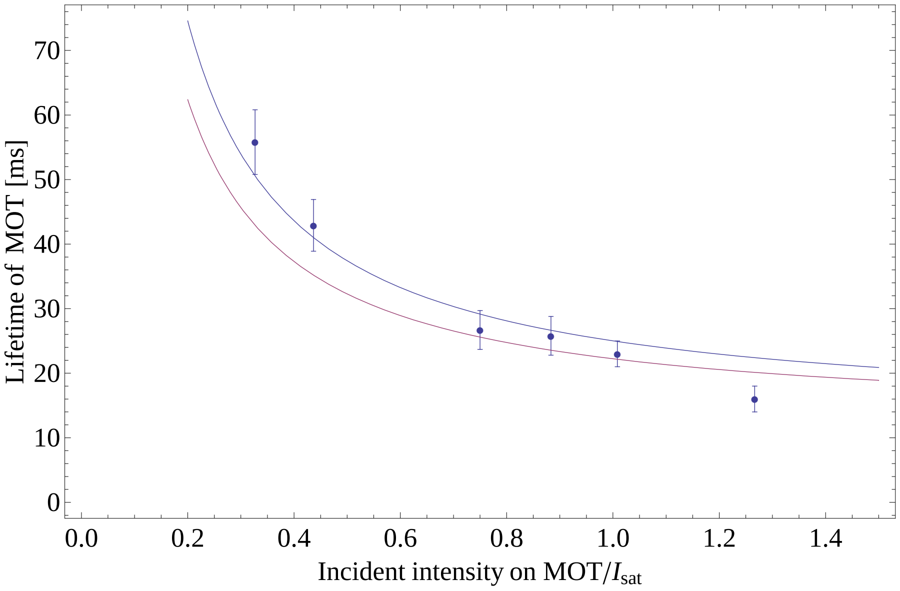

Figure 6.13: The variation of the trap lifetime as the total intensity incident on the atoms was varied. The curves represent the lifetime predicted by the rate equation model (Eqn. 6.10) for two values of Γ_{34}, the literature value of 300 s^{-1} (maroon) and the fitted value 414 s^{-1} (blue). For both theory and experimentally measured values $\Delta = -24$ MHz.

Rate equations

The losses due to transitions into the triplet states can be analysed with a rate equation model, allowing the lifetimes of the trap to be calculated for various experimental parameters. Fig. 6.14 shows the relevant energy level structure for the analysis, while the transition rates are given in table 6.2.

A set of coupled differential equations can be constructed and solved to give the relative populations in each of the levels as a function of time when atoms are trapped in the 423 nm MOT. Assuming that the filling rate is constant, the

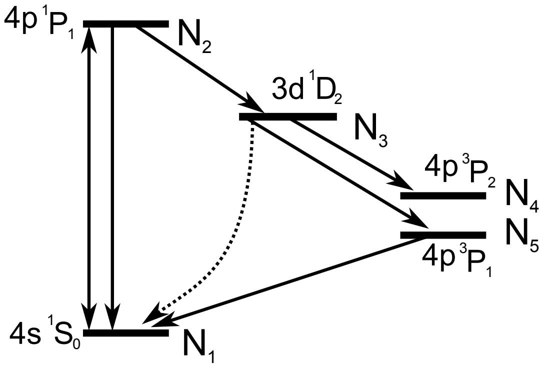

Figure 6.14: The energy levels relevant to the 423 nm MOT lifetime. The transition rates are given separately in Table 6.2. The dashed line represents an effective decay from $^1D_1$ to $^1S_0$.

equations can be written as follows [154],

$$\begin{aligned}
\dot{N_1} &= R - L(\Delta, I)(N_1 - N_2) + \Gamma_{21}N_2 + \Gamma_{31}N_3(1-\epsilon), \\
\dot{N_2} &= L(\Delta, I)(N_1 - N_2) - \Gamma_{23}N_2 - \Gamma_{21}N_2, \\
\dot{N_3} &= \Gamma_{23}N_2 - \Gamma_{31}N_3 - \Gamma_{34}N_3, \\
\dot{N_4} &= \Gamma_{34}N_3 - \Gamma_{31}\epsilon N_4, \qquad (6.6)
\end{aligned}$$

where R is the filling rate into the trap, N_i is the population of atoms in the i^{th} state, Γ_{ij} is the spontaneous transition rate between the i and j states, $L(\Delta, I) = (\Gamma_{21}^3/8)(\frac{I/I_{sat}}{\Delta^2+(\Gamma_{21}/2)^2})$ is the stimulated transition rate [24], and ϵ is the fraction of atoms that are fast enough to leave the MOT trapping region before they have time to decay from the $^1D_2$ state.

In steady state, the total number of trapped atoms, $N_T = N_1 + N_2 + N_3$, is constant, therefore,

$$\begin{aligned}
\dot{N_T} &= \dot{N_1} + \dot{N_2} + \dot{N_3} \\
&= R - (\Gamma_{34} + \epsilon\Gamma_{31})\frac{N_3}{N_1 + N_2 + N_3}N_T \\
&= 0. \qquad (6.7)
\end{aligned}$$

i	j	$\Gamma_{ij}[\mathrm{s}^{-1}]$
2	1	2.18×10^8
2	3	2180
3	4	300
3	5	96
5	1	2100

Table 6.2: The transition rates, Γ_{ij}, for each the relevant energy levels in Fig. 6.14 [65].

where,

$$\frac{N_3}{N_1+N_2+N_3} = \left[1+\frac{N_2}{N_3}\left(\frac{N_2}{N_1+N_2}\right)^{-1}\right]^{-1}, \tag{6.8}$$

and

$$\frac{N_2}{N_3} = \frac{\Gamma_{31}+\Gamma_{34}}{\Gamma_{23}}. \tag{6.9}$$

Assuming that N_1 and N_2 can be treated as a two level system[1], the fraction of atoms in the upper state $(N_2/(N_1+N_2))$ is therefore given by Eqn. 2.1. The lifetime of the trap is given by the analytic expression

$$\tau_{MOT}(\Delta, I) = 1+\frac{\Gamma_{31}+\Gamma_{34}}{\Gamma_{23}n_e(\Delta, I)}\frac{1}{\Gamma_{34}+\epsilon\Gamma_{31}}. \tag{6.10}$$

This expression is plotted in Fig. 6.13 using a detuning of $\Delta = -24$ MHz, and the transition rates listed in Table 6.2. The parameter ϵ is estimated to be 4.2 %, assuming a $^1D_2$ state lifetime and a MOT trapping radius of 10 mm [154].

The decay rates in Table 6.2 are those which are often used in the literature [82, 81]. However, as the transition rates Γ_{34} and Γ_{35} are low, and therefore difficult to measure, there have been varying values measured for the lifetime of the $^1D_2$ state [86]. Plotting Eqn. 6.10 as a function of the MOT beam intensity, using the values in the above table, predicts a lifetime shorter than the measured value. It is feasible to assume that the lifetime of $^1D_2$ state is shorter than that listed in

---

[1] The branching ratio of the decays from the $^1P_1$ state to the $^1D_2$ and $^1S_0$ states is 1:10^5 [154]

the table, therefore, Γ_{34} was made a free parameter of Eqn. 6.10 and then fitted to the data, returning a value for Γ_{34} of 414 s^{-1}. The data fit could have used Γ_{35} as the free parameter, however, it was kept constant at 96 s^{-1} as there were insufficient data points to allow both decay rates to be fitted.

6.4.2 Temperature

Measuring the temperature of an ensemble of atoms is a way of characterising the atomic velocity distribution. For atoms that have undergone laser cooling, the resulting temperature is a measure of how well the process was implemented, and is a critical parameter for calculating the phase space density of the sample. For an incident intensity equal to the saturation intensity and a laser detuning of $\Delta = -24$ MHz, the expected temperature is calculated to be 1.98 mK from Eqn. 2.12. The release and recapture technique is an appropriate method for measuring temperatures at this scale [71].

Method & result

The release and recapture technique requires the trapping volume for the atoms to be well known. To ease the temperature calculation, two of the MOT beams were passed through square apertures, which produced a cubic trapping region. Leaving one beam at full size removed any atoms that were outside the trapping region, ensuring that the fluorescence produced by the MOT, immediately after the lasers were switched on, was only due to the atoms that remained within the trapping region.

The procedure involved setting up the apparatus to operate as described in section 6.1, so as to produce a MOT, where fluorescence is measured with a photodiode. The fluorescence is then used to calculate the number of trapped atoms within the MOT, typically in excess of one million atoms. The shutter shown in Fig. 6.2 is then closed, abruptly blocking the three beams that create the MOT. The previously trapped atoms are released and ballistically expand. The shutter

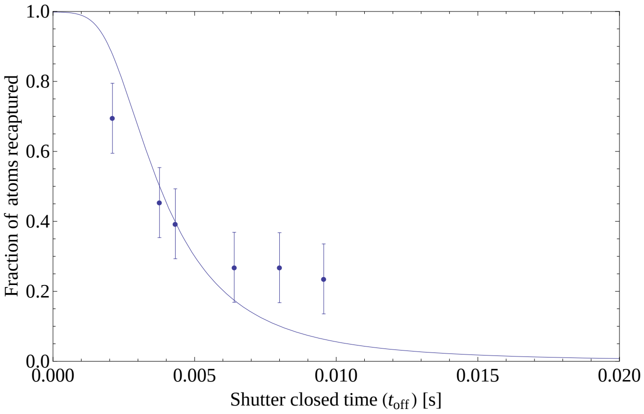

Figure 6.15: The fraction of atoms remaining in the MOT recapture region as a function of t_{off}. The theoretical fit for the data, shown as the solid line on the plot, returns a temperature of 3.2 mK of the atoms and is calculated using eq. 6.11, for $\Delta = -24$ MHz and $I/I_{sat} = 1$.

remains closed for a few milliseconds, t_{off}. During this time of ballistic expansion some atoms move out of the trapping region in which they were previously confined. After t_{off} the shutter is then reopened, allowing the beams to start the laser cooling process once more. At the instant the MOT is reestablished the fluorescence of the trap is measured with a photodiode. By comparing the initial steady state MOT fluorescence to the fluorescence produced by the remaining atoms after ballistic expansion, the temperature can be calculated using the method presented by Weiss *et al* [15].

Assuming that the initial spatial distribution of the atoms is Gaussian in the x, y, and z directions, the number of atoms, N, that remain after t_{off} in the cubic recapture volume is given by [15]

$$\frac{N}{N_0} = \int_{-d}^{d} \exp(-x^2/2\sigma_x^2)\mathrm{d}x \int_{-d}^{d} \exp(-y^2/2\sigma_y^2)\mathrm{d}y \int_{-d}^{d} \exp(-z^2/2\sigma_z^2)\mathrm{d}z, \quad (6.11)$$

where N_0 is the initial number of atoms, d is half of the length of one side of the square aperture, posing an upper limit on the recapture volume. Assuming the atomic velocities are described by a Maxwell-Boltzmann distribution [15], the time dependent widths of the cloud in the x and y directions are given by

$$\sigma_{x,y} = \sqrt{\sigma_0^2 + k_{\mathrm{B}}T\frac{t_{off}^2}{M}}, \tag{6.12}$$

where σ_0 is the initial cloud size, T is the temperature and M is the atomic mass. Since the magnetic field gradient of the MOT is twice as strong along the coil axis, the cloud width along the z-axis is given by

$$\sigma_z = \sqrt{\frac{\sigma_0^2}{2} + k_{\mathrm{B}}T\frac{t_{off}^2}{M}}. \tag{6.13}$$

The measured MOT fluorescence for various values of t_{off} are shown in Fig. 6.15. When the data were fitted to Eqn. 6.11, using an initial cloud radius of 1 mm, the temperature was found to be 3.2 mK. This value is in agreement with the temperature measurements of ^{40}Ca in the literature [80, 155, 156, 157, 158, 159], which range from 1.6 mK to 9.5 mK, depending on laser detuning and intensity. All of the measurements produce a temperature that is greater than the Doppler temperature, the reason behind this extra heating has been the subject of recent theoretical work, where it is proposed that coherences between the excited state sublevels cause an additional heating effect [160].

Chapter 7

Repuming Methods

In Chapter 6 the lifetime of the MOT was measured to be ∼20 ms. This value is in agreement with the rate equation analysis, which had previously shown that the decay rate into the $^3P_2$ state imposed an upper limit on the lifetime of the trap. Experiments by Grünert *et al* made use of atoms that had been lost to the long-lived $^3P_2$ state for a second-stage laser cooling setup. By using a laser at 1978 μm, in conjunction with the existing magnetic field, they constructed a second MOT using the $^3P_2 -^3 D_3$ transition. Cooling on this narrow transition produced a sample of atoms at a temperature of ∼20 μK. A diode laser at 430 nm was used to drive atoms from the $^3P_2$ state to the $^3P_1$ state, where they decayed back to the ground state via the 657 nm intercombination line. However, both the 1978 nm and 430 nm lasers are difficult to source, therefore alternative methods of utilising atoms in the $^3P_2$ state have been explored and are presented in this chapter.

7.1 Preventative repumping

The group of Hollberg were the first to demonstrate that the lifetime of a 423 nm calcium MOT could be increased by using a 672 nm laser [157]. Light at this wavelength excites atoms from the $^1D_2$ state to the higher lying $5p^1P_1$ state, intercepting the atoms before they have the chance to decay to the ^3P states. There are a number of decay routes atoms may take after they have been excited to the $5p^1P_1$. The most probable route is decaying directly back to the $^1D_2$ state, as shown in Fig. 7.1. The next most probable transition is to the $5s^1S_0$ state, from here atoms quickly decay into the 423 nm cooling cycle (Γ_{52}) and are thus retrapped. Atoms may also decay directly to the ground state, however, this is a relatively weak transition (Γ_{51}). The remaining decay channel provides a route into the triplet regime, from which atoms are either eventually lost to the $4p^3P_{0,2}$ states (Γ_{54}) or are retrapped by the 423 nm cooling cycle, via a decay from the $^3P_1$ state (included in Γ_{53}). The transition rates relevant for repumping in Fig. 7.1 are given in Table 7.1.

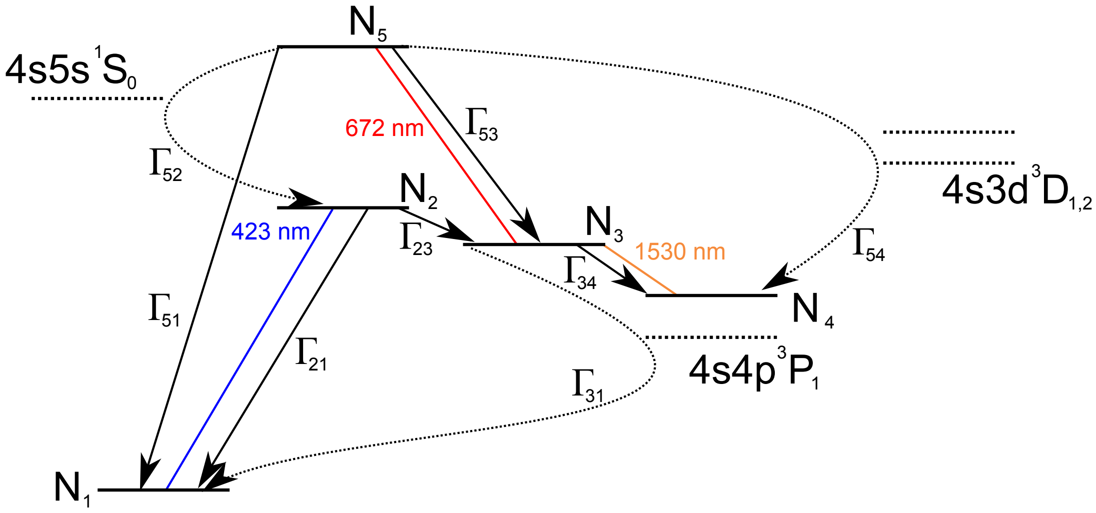

Figure 7.1: The energy levels of ^{40}Ca which are relevant to repumping atoms from metastable states back to the ground state. N_5 is the $5p\ ^1P_1$ state which atoms are excited to by the repump laser. Note that the energy spacings are not to scale.

A number of calcium MOT experiments have since employed a 672 nm repump laser [79, 161, 90]. Each experiment has reported an increase in the trap lifetime, but to varying degrees. Repump assisted lifetimes have been measured to be between 60 ms and 220 ms, depending on the power of the red laser and the intensity of the MOT beams. Ultimately the increase in atom number is limited by atoms decaying into the ${}^3P_2$ state, however, Γ_{54} is small enough that the population of the trap increases by around a factor of 5.

7.1.1 Rate equations

The set of differential equations, given in Eqn. 6.7, can be extended to include the effects caused by the repumping laser at 672 nm,

$$\begin{aligned}
\dot{N}_1 &= R - L_{1-2}(\Delta, I)(N_1 - N_2) + \Gamma_{21}N_2 + \Gamma_{31}N_3(1-\epsilon) + (\Gamma_{51} + \alpha\Gamma_{54})N_5, \\
\dot{N}_2 &= L_{1-2}(\Delta, I)(N_1 - N_2) - \Gamma_{23}N_2 - \Gamma_{21}N_2 + \Gamma_{52}N_5, \\
\dot{N}_3 &= \Gamma_{23}N_2 - \Gamma_{31}N_3 - \Gamma_{34}N_3 + \Gamma_{53}N_3 - L_{3-5}(\Delta, I)(N_3 - N_5), \\
\dot{N}_5 &= L_{3-5}(\Delta, I)(N_3 - N_5) - \Gamma_{52}N_5 - \Gamma_{53}N_5 - \Gamma_{54}N_5 - \Gamma_{51}N_5, \qquad (7.1)
\end{aligned}$$

where L_{1-2} and L_{3-5} are the stimulated transmission rates between the N_1 & N_2 and N_3 & N_5 states respectively. The coefficient α describes the fraction of atoms that return to the ground state from the N_5 state via the triplet regime, which is estimated to be ~ 0.5 [162].

i	j	$\Gamma_{ij}[10^6\ \mathrm{s}^{-1}]$
5	1	0.26
5	2	2.1
5	3	12
5	4	0.34

Table 7.1: The effective decay rates for transitions which occur when the 672 nm repump laser is used, see Fig. 7.1 [162, 65].

In steady state, $\dot{N}_T = \dot{N}_1 = \dot{N}_2 = \dot{N}_3 = \dot{N}_5 = 0$, the equations can be analytically solved to find the population of atoms in the N_2 state, assuming that the filling rate, R, is constant. In the limit of an infinite 672 nm intensity driving the repumping transition, the number of atoms in the N_2 state is enhanced by a factor of,

$$\xi = \frac{(\epsilon\Gamma_{31} + \Gamma_{34})(\Gamma_{31} + \Gamma_{34} + \Gamma_{51} + \Gamma_{52} + \Gamma_{54})}{(\Gamma_{31} + \Gamma_{34})(\epsilon\Gamma_{31} + \Gamma_{34} + \Gamma_{54} - \alpha\Gamma_{54})}, \tag{7.2}$$

Using the values listed in Tables 6.2 & 7.1, a 672 nm laser beam that is resonant with the transition and has an intensity equal to the saturation intensity should result in an increase of trapped atom number by a factor of 3.8 when compared to the case of no repumping laser.

The increase in trap lifetime due to the addition of the 672 nm laser to the setup can also be found using the above rate equations,

$$\begin{aligned} \dot{N_T} &= R - (\epsilon\Gamma_{31} + \Gamma_{34})N_3 - (1-\alpha)\Gamma_{54}N_5 \\ &= R - \underbrace{\left((\epsilon\Gamma_{31} + \Gamma_{34})\frac{N_3}{N_T} - (1-\alpha)\Gamma_{54}\frac{N_5}{N_T}\right)}_{1/\tau_{MOT}} N_T. \end{aligned} \tag{7.3}$$

Therefore, solving the equations in Eqn. 7.1 returns N_3/N_T and N_5/N_T in terms of the known decay rates and the repump laser power, allowing a direct calculation of the trap lifetime, τ_{MOT}, to be calculated. The lifetime of the trap is plotted in Fig. 7.2 as a function of the 672 nm laser intensity. The lifetime reaches a maximum of ~50 ms at beam intensities of $I/I_{sat} \approx 0.01$.

7.1.2 Repumping experiment

Transition detection

The light produced by the 672 nm ECDL was coupled to the vacuum table using a polarisation maintaining fibre. The light was then aligned into the vacuum chamber to be incident on the calcium MOT. With a lack of an absolute frequency reference for the ECDL, the MOT itself was used for locking the frequency of the laser. This was achieved by changing the DC voltage applied to the PZT of the ECDL, which in turn changed the output frequency of the laser. Fig. 7.3 shows a typical plot of the number of trapped atoms as the 672 nm laser is scanned across the $4^1S_2 - 5^1P_1$ transition.

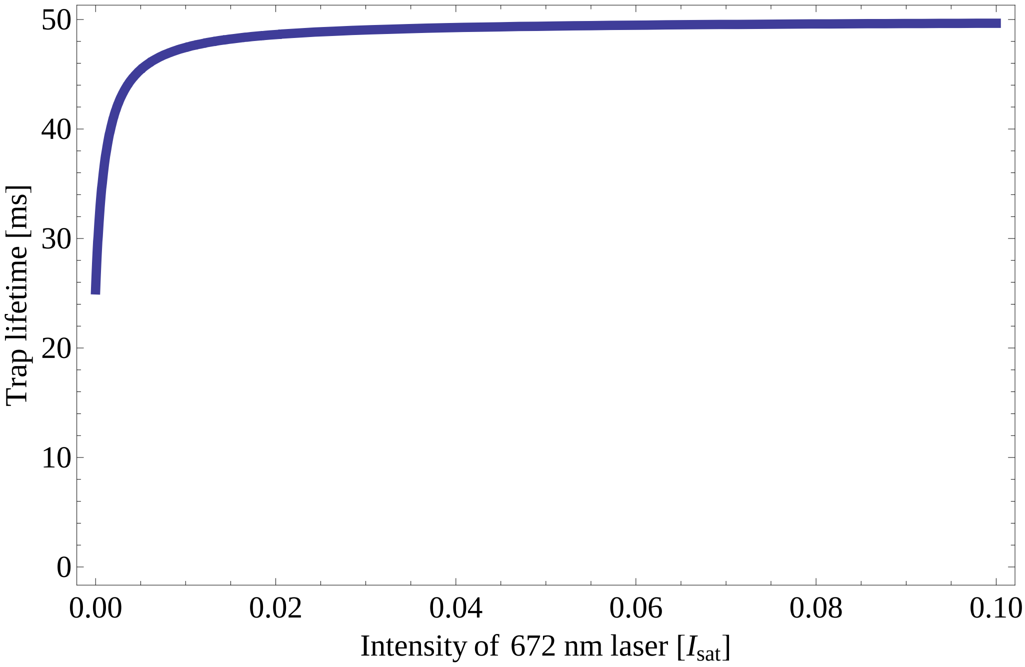

Figure 7.2: The theoretical increase in MOT lifetime as a function of the 672 nm laser intensity. The 672 nm laser is assumed to be on resonance with the transition and the intensity of blue light on the MOT is assumed to be equal to $I/I_{sat} = 1.2$.

The procedure to lock the laser to the reference cavity is given in section 5.3.2, however, to lock the laser to the atomic transition involved tuning the laser frequency until the MOT atom number was maximised. The RF current modulation was then applied to the diode and the reference cavity was locked to the HeNe laser. The ECDL output frequency was then altered slightly, such that the lower frequency sideband was resonating with a cavity mode. The ECDL was locked to the sideband dispersion signal and the synthesiser output frequency was increased until the MOT fluorescence was again maximised. Due to the diode being driven close to its maximum operating temperature, sudden laser mode hops were common, limiting the time the laser could maximise the MOT fluorescence to 1-2 hours, before having to be reset.

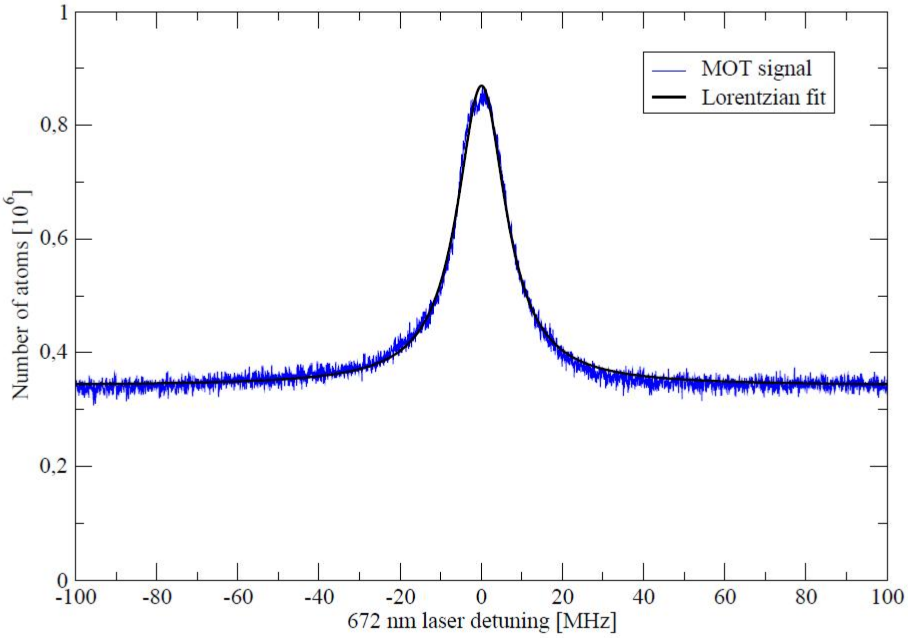

Figure 7.3: The number of trapped atoms as a function of the 672 nm laser detuning from the $4^1S_2 - 5^1P_1$ resonance. The 3 mW, 8 mm diameter, 672 nm laser beam was aligned incident to the MOT in a single pass configuration. The Lorentzian fit returns a linewidth of 15.1 MHz.

Increase in lifetime

The lifetime of the trap in the repump experiments was measured using a chopper to pulse the 2-D molasses beams on and off in the same as described previously (section 6.4.1). The lifetime of the trap was first measured without any repump light and is shown as the maroon points in Fig. 7.4. The repump laser was then directed onto the MOT and locked to the transition, striking the MOT with an incident intensity of $12I_{sat}$. The intensity of the 423 nm light on the MOT was $I/I_{sat} = 1.2$ and was detuned 24 MHz from the atomic resonance.

The lifetime with the repump laser on was then measured using the same method as above and is plotted using blue data points in Fig. 7.4. The lifetime without the repump laser was measured to be 16 ms while the lifetime increased to 44 ms with the use of the repump laser. These values are very close to those

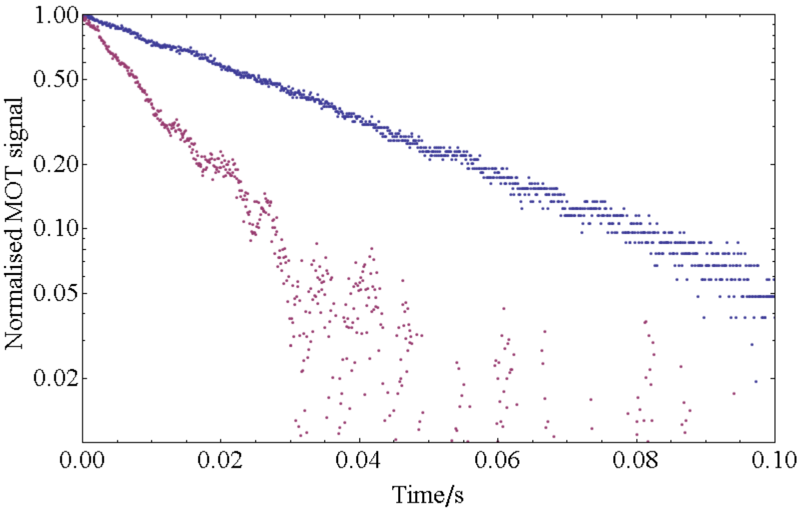

Figure 7.4: The MOT lifetime measured to be 44 ms with (blue) the 672 nm repump laser ($I/I_{sat} = 12$) and measured to be 16 ms without the repump laser.

calculated using the rate equations.

Intensity dependence

The locked 672 nm laser was used to excite the majority of the atoms falling into the 4^1D_2 back into the cooling cycle, increasing the number of atoms trapped in the MOT by a factor of 4. As the repumping process is inefficient, the laser must drive the transition relatively hard to ensure that atoms do not spend long periods of time in the 4^1D_2 and have the chance to decay to the 4^3P_2 state and be lost from the trap.

Fig. 7.5 shows the variation of MOT atom number enhancement as a function of the 672 nm laser power, which was varied using neutral density filters. The curve in the figure shows the expected change in MOT fluorescence with 672 nm laser power. The large difference between the expected result and the measured values is unclear, however, since the number of atoms is constant, and the lifetime of the trap is close to the expected value, this suggests that the filling rate of the trap is affected by the presence of the 672 nm laser. There was insufficient time to explore this possibility but would be a relatively fast experiment to perform

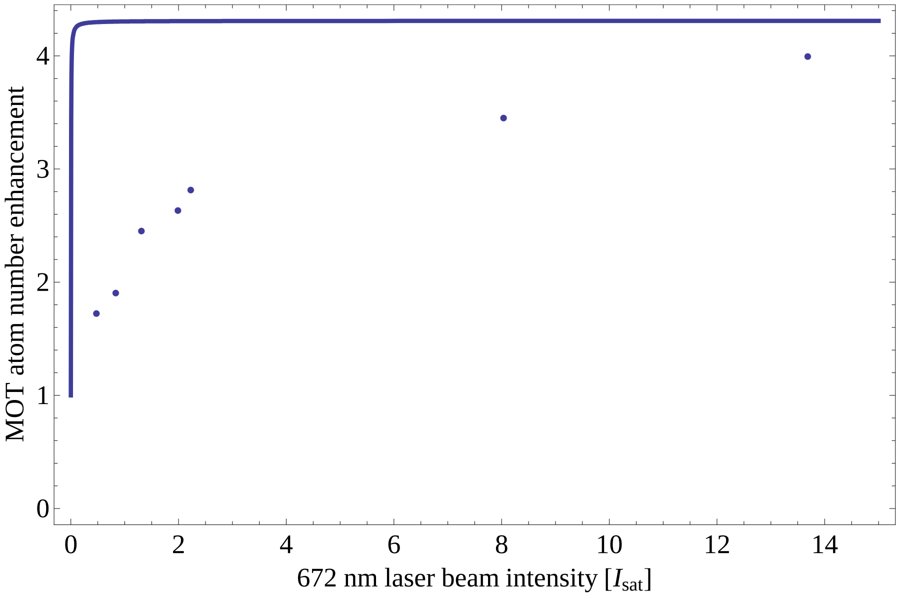

Figure 7.5: The data show the measured enhancement of the trapped atom number as a function of the 672 nm laser power. The beam diameter was ~8 mm. The curve shows the expected variation of enhancement with 672 nm laser power. The constants and decay rates used in the model were the same as those used in the previous section.

in future work.

A final point that should be noted from the rate equation analysis is that when the 672 nm laser is switched on the population in the $^1D_2$ state is removed as almost all of the atoms are pumped either into the metastable state or back into the cooling cycle, see Fig. 7.6.

7.2 Recovery repumping

The repumping scheme above results in an increased atom number and a MOT that exhibits a longer lifetime. However, atoms which have already decayed to the 4^3P_2, before the 672 nm laser is switched on, are essentially lost from the cooling cycle, but are still trapped by the MOT magnetic field. The $3^1D_2 -^3 P_2$ transition is one of the well known intercombination lines in ^{40}Ca, but there are

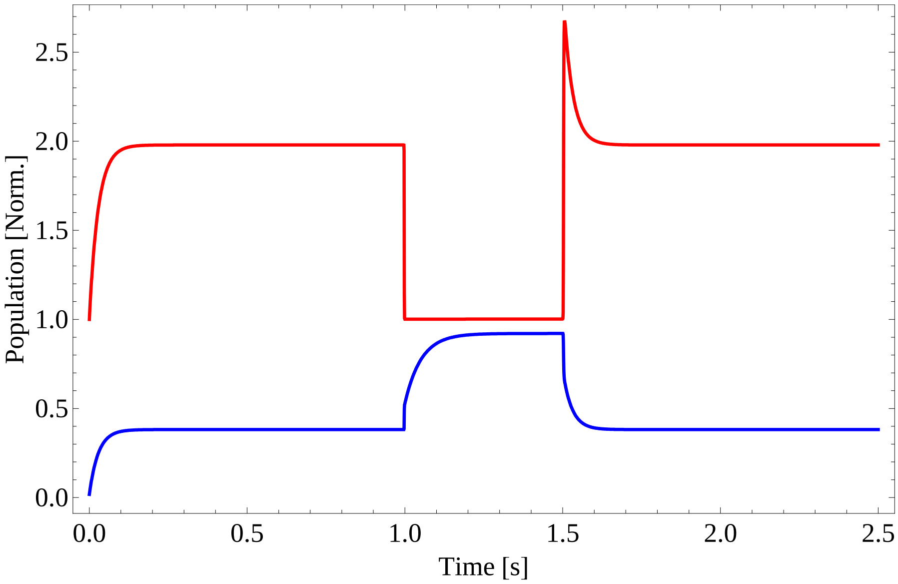

Figure 7.6: The populations in the N_2 & N_3 states as the resonant 672 nm laser is pulsed onto the MOT at $t = 1$ s for 0.5 s. The population in the N_3 state (red) empties within a few ms, allowing a large fraction of the atoms to be returned into N_2 state (blue) and retrapped in the MOT.

no references in the literature to the transition ever being stimulated by a laser source. The 15 mW of 1530 nm light output by the commercial diode laser was aligned into the MOT chamber as shown in Fig. 6.2.

Transition detection

As the line had not been observed previously in a laser cooling experiment, it was necessary to search for the exact wavelength of the light required for the transition. This was done by first loading the 423 nm MOT using the standard procedure described in chapter 6 and then illuminating the MOT with the 1530 nm laser light. The MOT fluorescence was monitored using a photodiode, while the temperature of the 1530 nm diode laser was scanned, as this was the mechanism for altering the output wavelength. Using a HP optical spectrum analyser the wavelength of the transition was measured to be 1530.562(7) nm.

Initially, it was expected that there would be an increase in the MOT fluores-

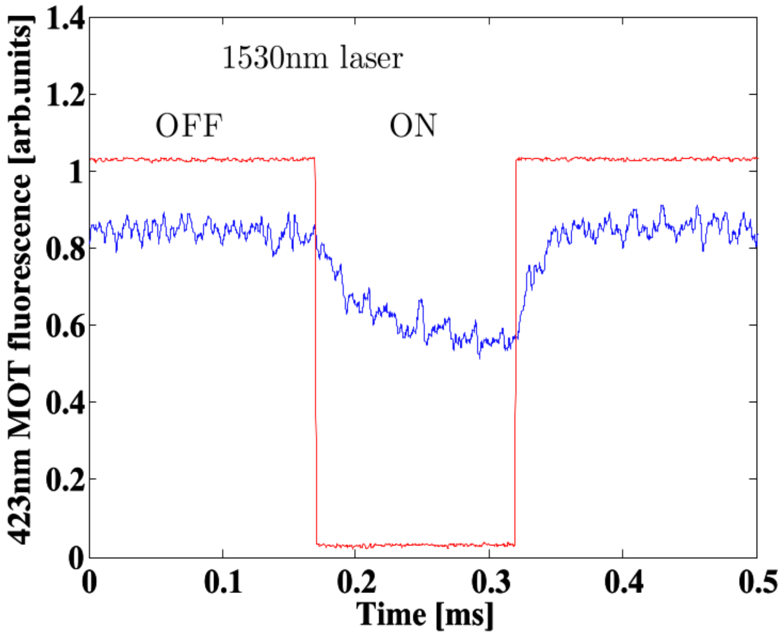

Figure 7.7: The blue trace shows the 423 nm steady state MOT fluorescence, with no incident 672 nm laser, as the resonant 1530 nm laser is pulsed on using a shutter.

cence when the laser was resonant with the transition. However, as can be seen from Fig. 7.7 a drop in the fluorescence was observed when the laser was used to excite the transition. This can be explained by the density of atoms in each of the states. When atoms in the MOT decay into the $^1D_2$, they are loaded into a volume equal to the size of the MOT, and are immediately addressed by the 1530 nm laser before they have a chance expand into a larger volume. However, once atoms enter the $^3P_2$ state they are not confined to the MOT region and expand into an ellipsoid determined by the MOT magnetic field. Assuming a temperature of 3.2 mK, the distance the atoms can expand along the z-axis is 2.5 mm in each direction, while in the x and y axis this is 5 mm in each direction. The laser now essentially drives a two level system where it only addresses a fraction of the atoms in the lower state, due to the large volume the atoms occupy. This results in atoms being driven into the $^3P_2$ state where they then expand into the larger volume. Driving atoms into the $^3P_2$ state changes the branching ratio of atoms decaying into the triplet and effectively reduces the rate of atoms decaying into the $^3P_1$ state, which reduces the number of atoms decaying back into the cooling cycle, and a drop in MOT fluorescence is observed.

The rate equations in Eqn. 7.1 can be easily adapted to include a drive term, $L_{3-4}(N_3 - N_4)$, to represent the 1530 nm laser,

$$\begin{aligned}
\dot{N}_1 &= R - L_{1-2}(\Delta, I)(N_1 - N_2) + \Gamma_{21}N_2 + \Gamma_{31}N_3(1-\epsilon) + (\Gamma_{51} + \alpha\Gamma_{54})N_5, \\
\dot{N}_2 &= L_{1-2}(\Delta, I)(N_1 - N_2) - \Gamma_{23}N_2 - \Gamma_{21}N_2 + \Gamma_{52}N_5, \\
\dot{N}_3 &= \Gamma_{23}N_2 - \Gamma_{31}N_3 - \Gamma_{34}N_3 + \Gamma_{53}N_3 \\
&\quad - L_{3-5}(\Delta, I)(N_3 - N_5) - L_{3-4}(\Delta, I)(N_3 - \beta N_4), \\
\dot{N}_4 &= \Gamma_{34}N_3 + \Gamma_{54}N_5(1-\alpha) + L_{3-4}(\Delta, I)(N_3 - \beta N_4), \\
\dot{N}_5 &= L_{3-5}(\Delta, I)(N_3 - N_5) - \Gamma_{52}N_5 - \Gamma_{53}N_5 - \Gamma_{54}N_5 - \Gamma_{51}N_5, \qquad (7.4)
\end{aligned}$$

the coefficient was introduced to account for the laser only being able to address a fraction of the atoms in the N_4 state. As 1530 nm was the only laser repumping the atoms in this experiment, $L_{3-5}(\Delta, I)$ (the 672 nm laser intensity) was set equal to zero in the rate equation model.

Fig. 7.8 shows the population in the N_2 and N_3 states as the MOT is loaded and the resonant 1530 nm laser is pulsed into the MOT region, this was calculated using the solution to the rate equations. Using the model, the β coefficient has been estimated to be $\approx 0.7\%$ of the total number of atoms in the N_4 state.

7.3 Combined repumping

Fig. 7.6 shows that the population in the $^1D_2$ state can be removed by applying a laser at 672 nm. Fig. 7.8 shows that the number of atoms in the MOT drops when a resonant 1530 nm laser is incident. The rate equation analysis showed that this was due to the laser addressing fewer atoms in the $^3P_2$ state than the upper $^1D_2$ state. The rate equations in Eqn. 7.4 were set up to include the effects from both the 672 nm and 1530 nm lasers simultaneously. The model of the

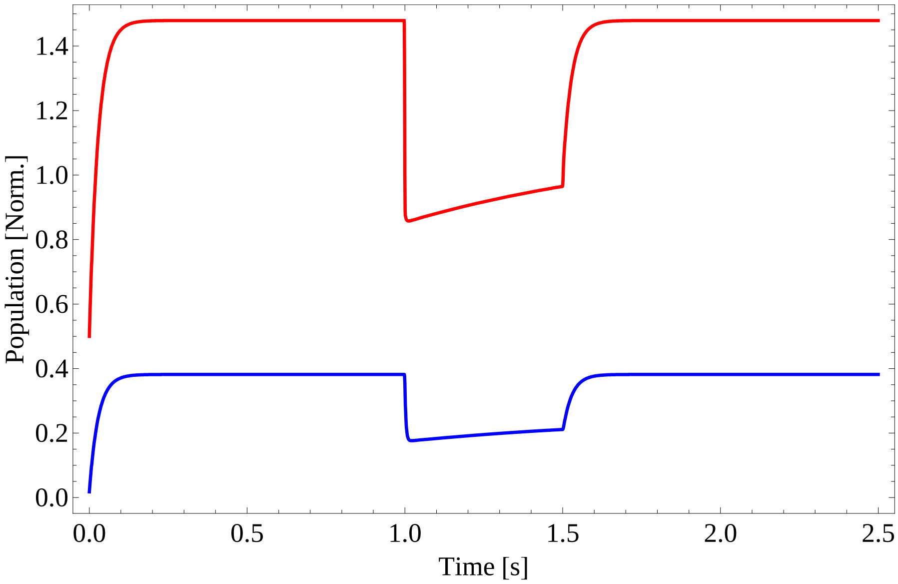

Figure 7.8: The populations in the N_2 & N_3 states as a function of time. When the 1530 nm laser is pulsed on at t=1 s, the population in the N_3 state (red) drops as atoms are driven into the $^3P_2$ state. As a result, the population in the N_2 state (blue) also drops. Both of the curves have been normalised and the N_3 population curve has been given an offset to allow a comparison of the populations.

updated system is shown in Fig. 7.9. In this figure the 672 nm laser is switched on first until the MOT is in steady state. At this point the $^1D_2$ state (blue) is empty and the number of atoms in the 423 nm MOT (red) has increased by a factor of ∼4. When the 1539 nm laser is switched on at $t = 2.5$ s, a number of atoms in the $^3P_2$ state are excited back into the cooling cycle and result in a higher trapped atom number. This is due to the population of the $^1D_2$ state being close to zero.

The experimental setup was then adapted to have the 672 nm and 1530 nm beams overlapped, using a polarising beamsplitter cube, before entering the MOT chamber. The resonant beams were then simultaneously pulsed onto the MOT cloud while the fluorescence was detected using the photodiode. The result of the combined laser light can be seen in Fig. 7.10

Fig. 7.10 has the same conditions as used in the model from $t = 2.5$ s to $t = 3$

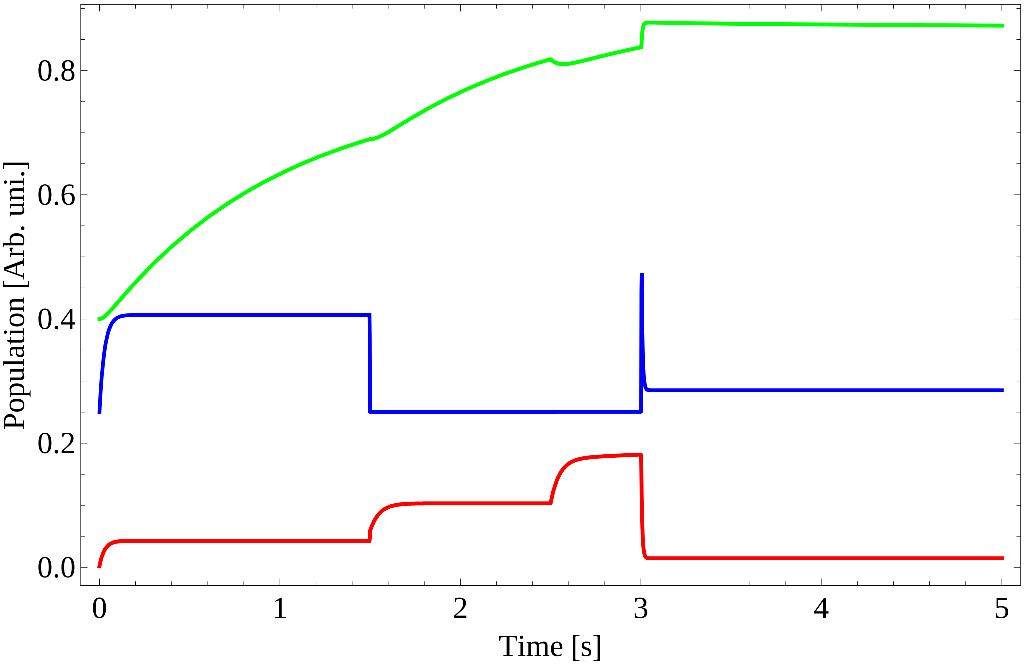

Figure 7.9: The populations in each of the N_2 (red), N_3 (blue), N_4 (green) states as the 672 nm laser is switch on at $t = 1.5$ s and the 1530 nm laser is switched on at $t = 2.5$ s, both lasers are then switched off at $t = 3$ s. Note the curves have been normalised and a vertical offset has been applied to allow direct comparison.

s, confirming the prediction by the model that there would be an increase in the number of atoms.

Conclusions

The number of atoms trapped in the calcium MOT has been increased by a factor of 9 using a combination of a 672 nm diode laser and a 1530 nm diode laser. A rate equation model has been developed that explains the increase in the number of atoms in both the 672 nm repump case and the combined 672 & 1530 nm repump case.

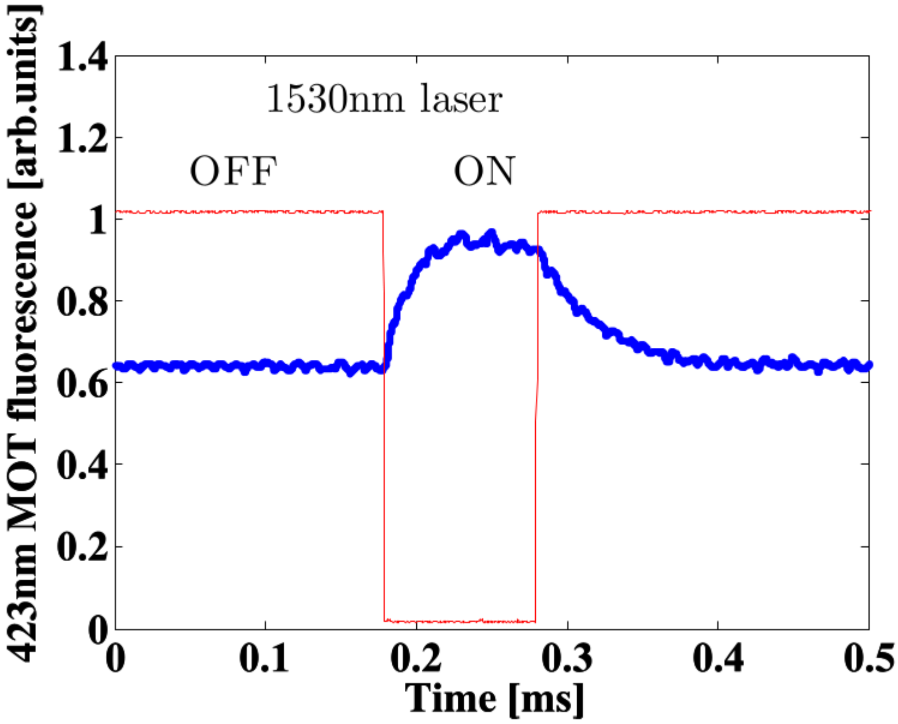

Figure 7.10: The effect of pulsing 15 mW of resonant 1530 nm and 5 mW of 672 nm light, simultaneously, on the the MOT.

Chapter 8

Conclusions

8.1 Summary

In Chapter 2 an overview of laser cooling and trapping was presented, with a particular focus on the theory of the scattering force, Doppler cooling and the magneto-optical trap (MOT). This was followed by a description of calcium and how its atomic properties make it a desirable element for laser cooling.

Details of the construction of a compact vacuum system were given in Chapter 3. This included a description of the oven used to generate a collimated beam of atomic calcium. A short Zeeman slower, incorporated into the vacuum system, was used to slow the atoms emerging from the oven. The Zeeman slower field was measured and compared with the ideal slower field. The theoretical fraction of atoms in the beam addressed by the slower was then calculated. The function and operation of the deflection and MOT chambers was also described.

Chapter 4 described the design, construction and characterisation of a frequency doubled Ti:sapphire laser system for generating light to stimulate the $^1S_0 - ^1P_1$ transition in ^{40}Ca. A Hänsch-Couillaud locking scheme was used to generate 100 mW of narrow-linewidth, 423 nm, light using a resonant enhancement cavity containing a ppKTP crystal. A novel method of locking the Ti:sapphire laser to the atomic transition using a hollow-cathode lamp is also presented.

Technical details of the laser diodes used in the calcium experiment were detailed in Chapter 5.

In Chapter 6 the procedure used to set up, what is believed to be, the first calcium MOT in the UK was given. Each stage of the setup had been optimised to produce around 100,000 atoms in the trap. The lifetime of the trap was calculated by solving a system of rate equations. Under typical operating conditions, the measured MOT lifetime was found to agree well with the rate equation model, when a reasonable modification to the decay rates from the $^1D_2$ state was included.

In Chapter 7 repumping schemes for the calcium MOT were explored. A 672 nm laser was used to intercept atoms decaying from the main cooling cycle and repump them back into the system. The observed increase in the number of trapped atoms agrees well with the updated rate equation model, which takes into account the additional states that are populated when this transition is excited. The $^3P_1 - ^1D_2$ transition has been observed at 1530.5 nm using a commercial laser diode. Stimulating this transition in the absence of the 672 nm laser resulted in a reduction in the trapped atom number, this was due to the relative population in each of the states. However, with both repump lasers (672 nm & 1530 nm) incident on the MOT, fluorescence was seen to increase by a factor of 6.

8.2 Improvements

The aim of the work in this thesis was to generate a large sample of cold calcium atoms and explore techniques that could be used to further lower the temperature, but at the same time, trap as many atoms as possible. Using the setup, atoms within the trap reached a temperature of 3 mK, close to the Doppler temperature. Using repump lasers, leaks into the triplet states have been partially blocked, resulting in over 1 million atoms being trapped.

The response of the trapped atom number as a function of the repump laser intensity does not agree with the solution of the rate equations. However, the measured lifetime of the trap, when the 672 nm laser is operating, is close to the value of the lifetime predicted by the model. Since in steady state the total number of atoms remains constant, the filling rate of the trap must also be a function of the 672 nm laser intensity. The available power from the 672 nm laser was a limiting factor for taking a greater set of measurements. By transporting the ECDL to the vacuum table, a higher intensity of 672 nm light would be made available and allow a larger number of measurements to be made for both the atom number and the filling rate, which would provide greater insight to the dominant loss mechanism for the calcium MOT.

The release and recapture technique used for measuring the temperature of the atoms in the trap are affected by the large number of atoms in the $^1D_2$ state. Atoms remain in this state for up to 2.5 ms and during this time are free to expand to a large distance beyond the trap centre. They can then return to the ground state and begin to, once again, scatter photons, resulting in a bigger recapture region than expected for the temperature calculation. A more accurate way of finding the temperature of the atoms would be to measure the Doppler broadened lineshape of the 657 nm intercombination line [157].

8.3 Future Work

To achieve a calcium BEC, the temperature of the atoms generated by the experiment in this thesis must be reduced by around a further 4 orders of magnitude. To do this, a method similar to that used by the PTB group could be used. This would involve using a high power laser to trap the calcium atoms in an optical dipole trap and use a standard forced evaporation technique to reduce the velocity distribution of the atoms present in the trap. As there is sufficient optical access to the MOT chamber used in the Strathclyde experiment, an optical dipole trap could be introduced to the apparatus with relative ease. To reach BEC three-body collisions need to be minimised, the PTB group note that this can be done by loading the atoms into a large volume dipole trap.

Bibliography

[1] NIST Database, *http://physics.nist.gov/cuu/Constants/Table/allascii.txt*, (2009).

[2] T. W. Hänsch and A. L. Schawlow, *Cooling of gases by laser radiation*, Opt. Commun. **13**, 68 (1975).

[3] S. Stenholm, *Foundations of Laser Spectroscopy*, Wiley, 1984.

[4] D. Wineland and H. Dehmelt, *Proposed 10*^{14} $\Delta\nu < \nu$ *Laser fluorescence spectroscopy on Ti*$^{+}$ *mono-ion oscillator III*, Bull. Am. Phys. Soc. **20**, 637 (1975).

[5] D. Wineland, R. E. Drullinger, and F. L. Walls, *Radiation pressure cooling of bound resonant absorbers*, Phys. Rev. Lett. **40**, 1639 (1978).

[6] R. Blatt, P. Gill, and R. C. Thomoson, *Current perspectives on the physics of trapped atoms*, J. Mod. Opt. **39**, 193 (1992).

[7] W. D. Phillips and H. Metcalf, *Laser deceleration of an atomic beam*, Phys. Rev. Lett. **48**, 596 (1982).

[8] S. Chu, L. Hollberg, J. E. Bjorkholm, A. Cable, and A. Ashkin, *Three-dimensional viscous confinement and cooling of atoms by resonance radiation pressure*, Phys. Rev. Lett. **55**, 48 (1985).

[9] A. L. Migdall, J. V. Prodan, W. D. Phillips, T. H. Bergeman, and H. J. Metcalf, *First Observation of Magnetically Trapped Neutral Atoms*, Phys. Rev. Lett. **54**, 2596 (1985).

[10] E. Raab, M. Prentiss, A. Cable, S. Chu, and D. Pritchard, *Trapping of Neutral Sodium Atoms with Radiation Pressure*, Phys. Rev. Lett. **59**, 2631 (1987).

[11] S. Stenholm, *The semiclassical theory of laser cooling*, Rev. Mod. Phys. **58**, 699 (1986).

[12] P. D. Lett, R. N. Watts, C. I. Westbrook, W. D. Phillips, P. L. Gould, and H. J. Metcalf, *Observation of atoms laser cooled below the Doppler limit*, Phys. Rev. Lett. **61**, 169 (1988).

[13] J. Dalibard and C. Cohen-Tannoudji, *Laser cooling below the Doppler limit by polarization gradients: simple theoretical models*, J. Opt. Soc. Am. B **6**, 2023 (1989).

[14] P. J. Ungar, D. S. Weiss, E. Riis, and S. Chu, *Optical molasses and multilevel atoms: theory*, J. Opt. Soc. Am. B **6**, 2058 (1989).

[15] D. S. Weiss, E. Riis, Y. Shevy, P. J. Ungar, and S. Chu, *Optical molasses and multilevel atoms: experiment*, J. Opt. Soc. Am. B **6**, 2072 (1989).

[16] S. Chu, *The manipulation of neutral particles*, Rev. Mod. Phys. **70**, 685 (1998).

[17] W. D. Phillips, *Laser cooling and trapping of neutral atoms*, Rev. Mod. Phys. **70**, 721 (1998).

[18] C. N. Cohen-Tannoudji, *Manipulating atoms with photons*, Rev. Mod. Phys. **70**, 721 (1998).

[19] K. Huang, *Statistical Mechanics*, Wiley, 1987.

[20] S. N. Bose, Z. Phys. D **26**, 178 (1924).

[21] A. Einstein, Sitzber. Kgl. Preuss. Akad. Wiss. , 261 (1924).

[22] J. Bardeen, L. N. Cooper, and J. R. Schrieffer, *Theory of superconductivity*, Phys. Rev. **108**, 1175 (1957).

[23] P. E. Sokol, *Bose condensation in liquid helium*, Neutron News **4**, 22 (1993).

[24] C. S. Adams and E. Riis, *Laser cooling and trapping of neutral atoms*, Prog. Quant. Electr. **21**, 1 (1997).

[25] W. Petrich, M. H. Anderson, J. R. Ensher, and E. A. Cornell, *Stable, tightly confining magnetic trap for ecaporative cooling of neutral atoms*, Phys. Rev. Lett. **74**, 3352 (1995).

[26] K. B. Davis, M. O. Mews, and W. Ketterle, *An analytical model for evaporative cooling of atoms*, Appl. Phys. B **60**, 155 (1994).

[27] M. H. Anderson, J. R. Ensher, M. R. Matthews, C. E. Wieman, and E. A. Cornell, *Observation of Bose-Einstein condensation in a dilute atomic vapor*, Science **269**, 198 (1995).

[28] K. B. Davis, M. O. Mewes, M. R. Andrews, N. J. van Druten, D. S. Dufree, and D. M. K. dn W. Ketterle, *Bose-Einstein condensation in a gas of sodium atoms*, Phys. Rev. Lett. **75**, 3969 (1995).

[29] E. A. Cornell and C. E. Wieman, *Nobel lecture: Bose-Einstein condensation in a dilute gas, the first 70 years and some recent experiments*, Rev. Mod. Phys. **74**, 875 (2002).

[30] W. Ketterle, *Nobel lecture: When atoms behave as waves: Bose-Einstein condensation and the atom laser*, Rev. Mod. Phys. **74**, 1131 (2002).

[31] *http://www.uibk.ac.at/exphys/ultracold/atomtraps.html*, (2009).

[32] M. R. Andrews, C. G. Townsend, H. J. Miesner, D. S. Dufree, D. M. Kurn, and W. Ketterle, *Observation of interference between two Bose condensates*, Science **275**, 637 (1997).

[33] M. Greiner, O. Mandel, T. Esslinger, T. Hansch, and I. Bloch, *Quantum phase transition from a superfluid to a Mott insulator in a gas of ultracold atoms*, Nature **415**, 39 (2002).

[34] B. DeMarco and D. S. Jin, *Onset of Fermi degeneracy in a trapped atomic gas*, Science **285**, 1703 (1999).

[35] C. R. Ooia, K.-P. Marzlinb, and J. Audretschc, *Laser cooling of molecules via single spontaneous emission*, Eur. Phys. J. D **22**, 259267 (2002).

[36] S. Jochim, M. Bartenstein, A. Altmeyer, G. Hendl, S. Riedl, C. Chin, J. H. Denschlag, and R. Grimm, *Bose-Einstein condensation of molecules*, Science **302**, 2101 (2003).

[37] M. Greiner, C. A. Regal, and D. S. Jin, *Probing the excitation spectrum of a Fermi gas in the BCS-BEC crossover regime*, Phys. Rev. Lett. **94**, 070403 (2005).

[38] F. P. D. Santos, J. Léonard, J. Wang, C. J. Barrelet, F. Perales, E. Rasei, C. S. Unnikrishnan, M. Leduc, and C. Cohen-Tannoudji, *Bose-Einstein condensation of metastable helium*, Phys. Rev. Lett. **86**, 3459 (2001).

[39] Y. Takasu, K. Maki, K. Komori, T. Takano, K. Honda, M. Kumakura, T. Yabuzaki, and Y. Takahashi, *Spin-singlet Bose-Einstein condensation of two-electron atoms*, Phys. Rev. Lett. **91**, 040404 (2003).

[40] A. Greismaier, J. Werener, S. Hensler, J. Stuhler, and T. Pfau, *Bose-Einstein condensation of chromium*, Phys. Rev. Lett. **94**, 160401 (2005).

[41] D. G. Fried, T. C. Killian, L. Willman, D. Landhuis, S. C. Moss, D. Kleppner, and T. J. Greytak, *Bose-Einstein condensatino of atomic hydrogen*, Phys. Rev. Lett. **81**, 3811 (1998).

[42] C. C. Bradley, C. A. Sackett, and R. G. Hulet, *Bose-Einstein condensation of Lithium: observation of limited condensate number*, Phys. Rev. Lett. **78**, 985 (1997).

[43] G. Modungno, G. Ferrari, G. Roati, R. J. Brecha, A. Simoni, and M. Inguscio, *Bose-Einstein condensation of potassium atoms by sympathetic cooling*, Science **294**, 1320 (2001).

[44] T. Weber, J. Herbig, M. Mark, H. C. Nägral, and R. Grimm, *Bose-Einstein condensation of cesium*, Science **299**, 232 (2003).

[45] K. R. Vogel, S. A. Diddams, C. W. Oates, E. A. Curtis, R. J. Rafac, W. M. Itano, J. C. Bergquist, R. W. Fox, W. D. Lee, J. S. Wells, and L. Hollberg, *Direct comparison of two cold-atom-based optical frequency standards by using a femtosecond-laser comb*, Opt. Lett. **26**, 102 (2001).

[46] M. Boyd, T. Zelevinsky, A. Ludlow, S. Foreman, S. Blatt, T. Ido, and J. Ye, *Optical atomic coherence at one second time scale*, Science **314**, 1430 (2006).

[47] O. I. de la Convention du Mtre, *The International System of Units (SI)*, Bureau International des Poids et Mesures, 8 th edition, 2006.

[48] D. J. Jones, S. A. Diddams, J. K. Ranka, A. Stentz, R. S. Windeler, J. L. Hall, and S. T. Cundiff, *Carrier-Envelope Phase Control of Femtosecond Mode-Locked Lasers and Direct Optical Frequency Synthesis*, Science **288**, 635 (2000).

[49] C. Degenhardt, H. Stoehr, C. Lisdat, G. Wilpers, H. Schnatz, B. Lipphardt, T. Nazarova, P. Pottie, U. Sterr, J. Helmcke, and F. Riehle, *Calcium op-*

tical frequency standard with ultracold atoms: Approaching 10-15 relative uncertainty, Phys. Rev. A **72**, 062111 (2005).

[50] C. W. Oates, E. A. Curtis, and L. Hollberg, *Improved short-term stability of optical frequency standards: approaching 1 Hz in 1 s with the Ca standard at 657 nm*, Opt. Lett. **25** (2000).

[51] M. Machholm, P. S. Julienne, and K. Suominen, *Collisions of cold magnesium atoms in a weak laser field*, Phys. Rev. A **59**, R4113 (1999).

[52] M. Machholm, P. Julienne, and K. Sominen, *Calculations of collisions between cold alkaline earth atoms in a weak laser field*, Phys. Rev. A **64**, 033425 (2001).

[53] G. Zinner, T. Binnewies, and F. Riehle, *Photoassociation of Cold Ca Atoms*, Phys. Rev. Lett. **85**, 2292 (2000).

[54] U. Dammalapati, *Metastable D-state spectroscopy and laser cooling of barium*, PhD thesis, Rijksuniversiteit Groningen, 2006.

[55] H. Katori, T. Ido, Y. Isoya, and M. Kuwata-Gonokami, *Magneto-optical trap and cooling of strontim atoms down to the photon recoil temperature*, Phys. Rev. Lett. **82**, 1116 (1999).

[56] H. Stoehr, F. Mensing, J. Helmcke, and U. Sterr, *Diode laser with 1 Hz linewidth*, J. Opt. Soc. Am. B **31**, 736 (2006).

[57] E. A. Curtis, C. W. Oates, and L. Hollberg, *Quenched narrow-line second- and third-stage cooling of* ^{40}Ca, J. Opt. Soc. Am. B **20**, 977 (2003).

[58] C. S. Adams, S. G. cox, E. Riis, and A. S. Arnold, *Laser cooling of calcium in a 'golden ratio' quasi-electrostsatic lattice*, J. Phys. B **36**, 1933 (2003).

[59] S. Kraft, F. Vogt, O. Appel, F. Riehle, and U. Sterr, *Bose-Einstein Condensation of Alkaline Earth Atoms:* ^{40}Ca, Phys. Rev. A **103**, 130401 (2009).

[60] S. Stellmer, M. K. Tey, B. Huang, R. Grimm, and F. Schreck, *Bose-Einstein Condensation of Strontium*, Phys. Rev. Lett. **103**, 200401 (2009).

[61] U. Dammalapati, I. Norris, and E. Riis, *Saturated absorption spectroscopy of calcium in a hollow-cathode lamp*, J. Phys. B **42**, 165001 (2009).

[62] U. Dammalapati, I. Norris, L. Maguire, M. Borkowski, and E. Riis, *A compact magneto-optical trap apparatus for calcium*, Meas. Sci. Technol. **20**, 095303 (2009).

[63] C. J. Foot, *Laser cooling and trapping of atoms*, Cont. Phys. **32**, 369 (1991).

[64] A. Ashkin, *Atomic-Beam deflection by resonance-radiation pressure*, Phys. Rev. Lett. **25**, 1321 (1970).

[65] NIST Database, *http://physics.nist.gov/PhysRefData/ASD/lines_form.html*, (2009).

[66] W. Ertmer, R. Blatt, J. Hall, and M. Zhu, *Laser manipulation of atomic beam velocities: demonstration of stopped atoms and velocity reversal*, Phys. Rev. Lett. **54**, 996 (1985).

[67] R. N. Watts and C. E. Wieman, *Manipulating atomic velocities using diode lasers*, Opt. Lett. **11**, 291 (1986).

[68] C. J. Foot, *Atomic Physics*, Oxford University Press, 2005.

[69] T. E. Barrett, S. W. Dapore-Schwartz, M. D. Ray, and G. P. Lafyatis, *Slowing atoms with* σ^- *polarized light*, Phys. Rev. Lett. **67**, 3483 (1991).

[70] Y. B. Ovchinnikov, *A Zeeman slower based on magnetic dipoles*, Opt. Commun. **276**, 261 (2007).

[71] P. D. Lett, W. D. Phillips, S. L. Rolston, C. E. Tanner, R. N. Watts, and C. I. Westbrook, *Optical molasses*, J. Opt. Soc. Am. B **6**, 2084 (1989).

[72] W. D. Phillips, *Laser cooling and trapping of neutral atoms*, in *Laser manipulation of Atoms and Ions*, edited by E. Arimondo, P. W. D., and F. Strumia, pages 289–337, 1992.

[73] M. Gajda and J. Mostowski, *Three-dimensional theory of the magneto-optical trap: Doppler cooling in the low-intensity limit*, Phys. Rev. A **49**, 4864 (1994).

[74] D. R. Lide, editor, *CRC handbook of chemistry and physics*, CRC Press, 74^{th} edition, 1995.

[75] C. E. Wieman and L. Hollberg, *Using diode lasers for atomic physics*, Rev. Sci. Instrum. **62**, 1 (1991).

[76] A. S. Arnold, C. S. Garvie, and E. Riis, *Large magnetic storage ring for Bose-Einstein condensates*, Phys. Rev. A **73**, 01606 (2006).

[77] M. J. Weber, *Handbook of laser wavelengths*, CRC Press, 1999.

[78] G. W. C. Kaye and T. Laby, *Tables of physical and chemical constants*, Longman, 1995.

[79] S. Hoekstra, A. K. Mollema, R. Morgenstern, H. W. Wilschut, and R. Hoekstra, *Single-atom detection of calcium isotopes by atom-trap trace analysis*, Phys. Rev. A **71**, 023409 (2005).

[80] J. Grunert and A. Hemmerich, *Optimizing the production of metastable Calcium atoms in a magneto-optic trap*, Appl. Phys. B **64**, 815 (2001).

[81] T. Kurosu and F. Shmuzu, *Laser cooling and trap of calcium and strontium*, Jpn. J. Appl. Phys. **29**, 2127 (1990).

[82] N. Beverini, F. Giammanco, E. Maccioni, F. Strumia, and G. Vissani, *Measurement of the calcium 1P1-1D2 transition rate in a laser-cooled atomic beam*, J. Opt. Soc. Am. B **6**, 2188 (1989).

[83] C. F. Fischer and G. Tachiev, *Allowed and spin-forbidden electric dipole transitions in Ca I*, Phys. Rev. A **68**, 012507 (2003).

[84] L. Pasternack, D. R. Yarkony, P. J. Dagdigian, and D. M. Silver, *Experimental and theoretical study of the Ca I* $4s3d^1D - 4s^{21}S$ *and* $4s4p^3P_1 - 4s^{21}S$ *forbidden transitions*, J. Opt. B, J. Phys. B **13**, 2231 (1980).

[85] L. R. Hunter, G. M. Watson, D. S. Weiss, and A. G. Zajonc, *High-precision measurement of lifetimes and collisional decay parameters in Ca 1D states using the two-photon Hanle effect*, Phys. Rev. A **31**, 2268 (1985).

[86] R. Drozdowski, J. Kwela, and M. Walkiewicz, *Lifetimes of the 4s4p(3)p(1) and 4s3d(1)d(2) states of ca-i*, Z. Phys. D **27**, 321 (1993).

[87] A. Derevianko, *Feasibility of Cooling and Trapping Metastable Alkaline-Earth Atoms*, Phys. Rev. Lett. **87**, 023002 (2001).

[88] T. Loftus, J. R. Bochinski, and T. W. Mossberg, *Magnetic trapping of ytterbium and the alkaline-earth metals*, Phys. Rev. A **66**, 013411 (2002).

[89] D. Hansen and A. Hemmerich, *Observation of Multichannel Collisions of Cold Metastable Calcium Atoms*, Phys. Rev. Lett. **96**, 073003 (2006).

[90] J. Grnert and A.Hemmerich, *Sub-Doppler magneto-optical trap for calcium*, Phys. Rev. A **65**, 041401 (2002).

[91] *Manual: Varian Valcon Plus 40 l/s vacuum pump.*

[92] F. Strumia, W. D. Phillips, and E. Arimondo, *Laser Manipulation of Atoms and Ions*, Amsterdam ; New York : North-Holland, 1991.

[93] K. J. Weatherill, *A* CO_2 *Laser Lattice Experiment for Cold Atoms*, PhD thesis, Durham University, 2007.

[94] C. Deamerow and W. Erley, *A simple and versatile ultrahigh vacuum leak-tight infrared window assembly*, J. Vac. Sci. Technol. A **5**, 2974 (1987).

[95] S. G. Cox, P. F. Griffin, C. S. Adams, D. DeMille, and E. Riis, *Reuseable ultrahigh vacuum viewport bakeable to 240C*, Rev. Sci. Instrum. **74**, 3185 (2003).

[96] D. M. Lucas, A. Ramos, J. P. Home, M. J. McDonnell, S. Nakayama, J.-P. Stacey, S. C. Webster, D. N. Stacey, and A. M. Steane, *Isotope-selective photo-ionization for calcium ion trapping*, Phys. Rev. A **69**, 012711 (2004).

[97] R. L. Targat, J. J. Zondy, and P. Lemonde, *75% efficiency blue generation from an intracavity PPKTP frequency doubler*, Opt. Commun. **247**, 471 (2005).

[98] F. Torabi-Goudarzi and E. Riis, *Efficient cw high-power frequency doubling in periodically poled KTP*, Opt. Commun. **227**, 289 (2003).

[99] G. D. Boyd and D. A. Kleinman, *Parametric interaction of focussed Gaussian beams*, J. Appl. Phys. **39**, 3597 (1968).

[100] P. A. Franken, A. E. Hill, C. W. Peters, and G. Weinreich, *Generation of optical harmonics*, Phys. Rev. Lett. **7**, 118 (1961).

[101] H. Mabuchi, E. S. Polzik, and H. J. Kimble, *Blue-light-induced infrared absorption in KNbO*, J. Opt. Soc. Am. B **11**, 2023 (1994).

[102] R. W. Boyd, *Nonlinear Optics*, Academic Press, 2008.

[103] F. Zernike and J. E. Midwinter, *Applied nonlinear optics*, Wiley, 1973.

[104] M. V. Pack, D. J. Armstrong, and A. V. Smith, *Measurement of the chi(2) Tensors of KTiOPO4, KTiOAsO4, RbTiOPO4, and RbTiOAsO4 Crystals*, Appl. Opt. **43**, 3319 (2004).

[105] R. L. Sutherland, D. G. McLean, and S. Kirkpatrick, *Handbook of Nonlinear Optics*, CRC Press, 2 edition, 2003.

[106] M. M. Fejer, G. A. Magel, D. H. Jundt, and R. L. Byer, *Quasi-phase-matched 2nd harmonic-generation - tuning and tolerances*, IEEE J. Quantum Electron. **28**, 2631 (1992).

[107] G. G. D. Miller, *Periodically poled lithium niobate: modeling, fabrication, and nonlinear-optical performance*, PhD thesis, Stanford University, 1998.

[108] W. Wiechmann, S. Kubota, T. Fukui, and H. Masuda, *Refractive-index temperature derivatives of potassium titanyl phosphate*, Opt. Lett. **18**, 1208 (1993).

[109] Coherent, *MBR-110 Single-Frequency Ti:Sapphire Laser*, 2000.

[110] Toptica, *Toptica FPI-100 Fabry-Pérot interferometer manual*, 2005.

[111] S. Wang, V. Pasiskevicius, F. Laurell, and H. Karlsson, *Ultraviolet generation by first order frequency doubling in ppKTP*, Opt. Lett. **23**, 1883 (1998).

[112] G. Norris, J. Harris, and G. McConnell, *Characterisation of periodically poled materials using nonlinear microscopy*, Opt. Expr. **16**, 5667 (2008).

[113] A. Ashkin, G. D. Boyd, and J. M. Dziedzic, *Resonant optical second harmonic generation and mixing*, IEEE J. Quantum Electron. **2**, 109 (1966).

[114] C. S. Adams and A. I. Ferguson, *Tunable narrow linewidth ultra-violet light generation by frequency doubling of a ring Ti : sapphire laser using lithium tri-borate in an external enhancement cavity*, Opt. Commun. **90**, 89 (1992).

[115] A. Ksendzov, E. Bloemhof, V. White, J. K. Wallace, R. O. Gappinger, J. S. Sanghera, L. E. Busse, W. J. Kim, P. C. Pureza, V. Q. Nguyen, I. D. Aggarwal, S. Shalem, and A. Katzir, *Measurement of spatial filtering capabilities of single-mode infrared fibers*, in *Proc. SPIE 6268*, 2006.

[116] A. Yariv, *Quantum electronics*, Wiley, New York, 1989.

[117] G. Brooker, *Modern classical optics*, Oxford University Press, 2003.

[118] E. D. Black, *An introduction to Pound-Drever-Hall laser frequency stabilization*, Am. J. Phys. **69**, 79 (2001).

[119] R. W. P. Drever, J. L. Hall, F. V. Kowalski, J. Hough, G. M. Ford, A. J. Munley, and H. Ward., *Laser Phase and Frequency Stabilization Using an Optical- Resonator*, Appl. Phys. B **31**, 97 (1983).

[120] T. W. Hänsch and B. Couillaud, *Laser frequency stabilization by polarization specroscopy of a reflecting reference cavity*, Opt. Commun. **35**, 441 (1980).

[121] B. Wolf, *Principles of Optics*, Pergammon Press, 1980.

[122] J. L. Hall, *Defining and measuring optical frequencies*, Rev. Mod. Phys. **78**, 1279 (2006).

[123] A. Mollema, I. W. Wansbeek, I. Willmann, K. Jungmann, R. G. E. Timmermans, and R. Hoekstra, *Laser-frequency locking using light-pressure-induced spectroscopy in a calcium beam*, Phys. Rev. A **77**, 043409 (2008).

[124] M. L. Harris, C. S. Adams, S. L. Cornish, I. C. McLeod, E. Tarleton, and I. G. Hughes, *Polarization spectroscopy in rubidium and cesium*, Phys. Rev. A **73**, 062509 (2006).

[125] K. B. MacAdam, A. Steinbach, and C. Wieman, *A narrow-band tunable diode-laser system with grating feedback, and a saturated absorption spectrometer for Cs and Rb*, Am. J. Phys. **60**, 1098 (1992).

[126] W. Demtröder, *Laser spectroscopy: basic concepts and instrumentation*, Springer, 2003.

[127] G. Camy, J. Borde, and M. Ducloy, *Hetrodyne saturation spectroscopy through frequency modulation of the saturating beam*, Opt. Commun. **41**, 325 (1982).

[128] C. I. Sukenik, H. C. Bush, and M. Shiddiq, *Modulation free laser frequency stabilization and detuning*, Opt. Commun. **203**, 133 (2002).

[129] E. D. van Ooijen, G. Kargert, and P. van der Straten, *Laser frequency stabilisation using Doppler-free bichromatic spectroscopy*, Appl. Phys. B **79**, 57 (2004).

[130] M. Huang and M. Lu, *A calcium vapor cell for atomic spectroscopy*, Rev. Sci. Instrum. **73**, 3747 (2002).

[131] C. J. Erickson, B. Neyenhuis, and D. S. Durfee, *High-temperature calcium vapor cell for spectroscopy on the 4s2 1S04s4p 3P1 intercombination line*, Rev. Sci. Instrum. **76**, 123110 (2005).

[132] R. L. Cavasso-Filo, A. Mirage, A. Scalabrin, D. Pereira, and F. C. Cruz, *Laser spectroscopy of calcium in hollow-cathode discharges*, J. Opt. Soc. Am. B **18**, 1922 (2001).

[133] *L2783-20NE-Ca Hamamatsu Hollow cathode lamp datasheet.*

[134] G. Smith, *Collision broadening and shift in the resonance line of calcium*, J. Phys. B **5**, 2310 (1972).

[135] O. M. Marago, B. Fazio, P. G. Gucciardi, and E. Arimondo, *Atomic gallium laser spectroscopy with violet/blue diode lasers*, Appl. Phys. B **77**, 809 (2003).

[136] R. N. Hall, G. E. Fenner, J. D. Kingsley, T. J. Soltys, and R. O. Carlson, *Coherent Light Emission From GaAs Junctions*, Phys. Rev. Lett. **9**, 366 (1962).

[137] R. V. Steele, *Diode-laser market grows at a slower rate*, Laser focus world **41**, 221439 (2005).

[138] ROHM, *Laser diode's application table*, 1st edition.

[139] D. A. Neamen, *Semiconductor Physics and devices*, McGraw Hill, third edition, 2003.

[140] P. Melman and W. J. Carlsen, *Interferometric measurement of time-varying longitudinal cavity modes in GaAs diode lasers*, Appl. Opt. **20**, 26942697 (1981).

[141] A. S. Arnold, J. S. Wilson, and M. G. Boshier, *A simple extended-cavity diode laser*, Rev. Sci. Instrum. **69**, 138 (1998).

[142] K. B. MacAdam, A. Steinbach, and C. Wieman, *A narrow-band tun- able diode-laser system with grating feedback, and a saturated absorption spectrometer for Cs and Rb*, Am. J. Phys. **60**, 1098 (1992).

[143] L. Ricci, M. Weidemuller, T. Esslinger, A. Hemmerich, C. Zimmermann, , Vuletic, W. Konig, and T. W. Hansch, *A compact grating-stabilized diode laser system for atomic physics*, Opt. Commun. **117**, 541 (1995).

[144] *Hitachi HL6545MG Diode laser datasheet.*

[145] S. Gerstenkorn and P. Luc, *Atlas du Spectre d'Absorption de la Molecule d'Iode*, Centre National de la Recherche Scientifique, Paris, 1978.

[146] V. P. Gerginov, Y. V. Dancheva, M. A. Taslakov, and S. S. Cartaleva, *Frequency tunable monomode diode laser at 670 nm for high resolution spectroscopy*, Opt. Commun. **149**, 162 (1998).

[147] A. G. Adam, T. E. Gough, and N. R. Isenor, *CO[sub 2] laser stabilization using an external cavity locked to a reference HeNe laser*, Review of Scientific Instruments **57**, 6 (1986).

[148] J. L. Hall, L. Hollberg, T. Baer, and H. G. Robinson, *Optical heterodyne saturation spectroscopy*, Appl. Phys. Lett. **39**, 680 (1981).

[149] M. Castelli, *Network consultants handbook*, Cisco Press, 2001.

[150] *QDFBLD-1530-20 1530 nm laser diode datasheet.*

[151] E. A. Donley, T. P. Heavner, F. Levi, M. O. Tataw, and S. R. Jefferts, *Double-Pass acousto-optic modulator system*, Rev. Sci. Instrum. **76**, 063112 (2005).

[152] M. A. Joffe, W. Ketterle, A. Martin, and D. E. Pritchard, *Transverse cooling and deflection of an atomic beam inside a Zeeman slower*, J. Opt. Soc. Am. B **10**, 2257 (1993).

[153] K. Lindquist, M. Stephens, and C. Wieman, *Experimental and theoretical study of the vapor-cell Zeeman optical trap*, Phys. Rev. A **46**, 4082 (1992).

[154] T. Kurosu and F. Shimizu, *Laser cooling and trapping of Alkaline earth atoms*, Jpn. J. Appl. Phys. **31**, 908 (1992).

[155] T. Chaneliere, J. Meunier, R. Kaiser, C. Miniatura, and D. Wilkowski, *Extra-heating mechanism in Doppler cooling experiments*, J. Opt. Soc. Am. B **22**, 1819 (2005).

[156] F. Riehle, A. Witte, T. Kisters, and J. Helmcke, *Interferometry with Ca atoms*, Appl. Phys. B **54**, 333 (1992).

[157] C. W. Oates, F. Bondu, R. W. Fox, and L. Hollberg, *A diode-laser optical frequency standard based on laser-cooled Ca atoms: Sub-kilohertz spectroscopy by optical shelving detection*, Eur. Phys. J. D **7**, 449 (1999).

[158] C. Degenhardt, T. Binnewies, G. Wilpers, U. Sterr, and F. Riehle, *Photoassociation spectroscopy of cold calcium atoms*, Phys. Rev. A **67**, 043408 (2003).

[159] R. Cavasso-Filo, A. Scalabrin, D. Pereira, and F. C. Cruz, *Observing negligible collision trap losses The case of alkaline earth metals*, Phys. Rev. A **67**, 021402 (2003).

[160] S. K. Choi, S. E. Park, J. Chen, and V. G. Minogin, *Three-dimensional analysis of the magneto-optical trap for (1+3)-level atoms*, Phys. Rev. A **77**, 015405 (2008).

[161] I. D. Moore, K. Bailey, J. Greene, Z. T. Lu, P. Mller, T. P. OConnor, C. Geppert, K. D. A. Wendt, and L. Young, *Counting Individual* ^{41}*Ca Atoms with a Magneto-Optical Trap*, Phys. Rev. Lett. **92**, 153002 (2004).

[162] R. Kurucz and B. Bell, *Atomic Line Data*, Smithsonian Astrophysical Observatory CD-ROM No. **23** (1995).